Challenges and solutions for sensor-based incremental nonlinear control of hydraulically actuated parallel robots

Luuk van Litsenburg

February 28, 2020

Delft University of Technology

TU Delft

Challenges and solutions for sensor-based incremental nonlinear control of hydraulically actuated parallel robots

by

L. van Litsenburg

to obtain the degree of Master of Science
at the Delft University of Technology,
to be defended publicly on Friday February 28, 2020 at 9:30 AM.

Student number: 4282345
Project duration: February 11, 2019 – February 28, 2020
Thesis committee:

Dr. ir. Q.P. Chu	TU Delft, Chair
Ir. O. Stroosma	TU Delft, Responsible thesis supervisor
Dr. ir. E. van Kampen	TU Delft, Examiner
Dr. ir. Alexei Sharpanskykh	TU Delft, Examiner

This thesis is confidential and cannot be made public until February 28, 2025.

An electronic version of this thesis is available at `http://repository.tudelft.nl/`.

TU Delft

Delft University of Technology

Copyright © Luuk van Litsenburg
All rights reserved.

Delft University Of Technology
Department Of
Control and Simulation

The undersigned hereby certify that they have read and recommend to the Faculty of Aerospace Engineering for acceptance a thesis entitled **"Challenges and solutions for sensor-based incremental nonlinear control of hydraulically actuated parallel robots"** by **Luuk van Litsenburg** in partial fulfillment of the requirements for the degree of **Master of Science**.

Dated: 28 February 2020

Readers:

dr.ir. Q. P. Chu

ir. O. Stroosma

dr.ir. A. Sharpanskykh

dr.ir. E. van Kampen

Preface

This work concludes my studies in Delft. I would like to thank QiPing Chu and Olaf Stroosma for their support and guidance throughout the thesis. The many meetings and enthusiasm made the thesis much more engaging. Furthermore, I would like to thank the people of SIM008 for their help with the thesis and their companionship. If any questions remain regarding this thesis feel free to contact me.

L. van Litsenburg
Delft, February 2020

Contents

Introduction

This document is the final thesis deliverable to obtain the degree of Master of Science in Aerospace Engineering at Delft University of Technology. This thesis addresses some of the challenges and solutions regarding nonlinear control of the SIMONA Research Simulator. The posed challenges and accompanying solutions are related to input saturations of the electro-hydraulic servo-valve, delays in the measurements and replacement of the main spool measurements by a servo-valve model. The solutions were implemented in the sensor-based nonlinear controller of the SIMONA Research Simulator and the results are presented in this work.

This document consists of three parts. The first part contains the paper that mainly shows the results from the experiments conducted on the SIMONA Research Simulator. The preliminary thesis is included in part II, which comprises the literature study and the preliminary research. Finally, part III contains the appendices that discuss some topics in more detail and show some additional results that were not treated in the paper.

I

Paper

Challenges and solutions for sensor-based incremental nonlinear control of hydraulically actuated parallel robots

Luuk van Litsenburg
Department of Control & Operations
Delft University of Technology
Delft, The Netherlands
L.vanLitsenburg@student.tudelft.nl

***Abstract*—Incremental Nonlinear Dynamic Inversion has shown increases in performance and robustness to model mismatches and uncertainties in hydraulic control as compared to other model-based controllers [1]. This work will expand on hydraulic Incremental Nonlinear Dynamic Inversion force control and discuss three of its challenges and accompanying solutions. The solutions are tested experimentally on the SIMONA Research Simulator. First, the importance of the synchronization of the linearization loops of the Incremental Nonlinear Dynamic Inversion controller is shown analytically and through experiments. Secondly, it is found that saturation of the electro-hydraulic servo-valve leads to wind-up when integral action is present. Pseudo Control Hedging is implemented to deal with the wind-up effects due to saturation. The implementation of the Pseudo Control Hedging is evaluated through experiments on the SIMONA Research Simulator. Thirdly, it is shown analytically that the main spool measurements should be used for the control increment of the Incremental Nonlinear Dynamic Inversion controller. Measurements of the main spool position are therefore used in the control, but it is often difficult to extract these from the servo-valve. Through experiments it is found that measurements of the main spool position can be replaced by either a first- or second-order servo-valve model.**

***Index Terms*—Force control, motion control, hydraulics, Incremental Nonlinear Dynamic Inversion, INDI, saturation**

I. Introduction

Hydraulic actuation is an attractive choice for many applications due to its stiffness [2] and ability to provide smooth and rapid responses under high loading conditions [3]. Some use cases require accurate control of hydraulic actuators as well, such as quadruped robots [4], automotive active suspension [5] and flight simulator motion control [3].

The objective of flight simulator motion control is to track a given trajectory as accurately as possible. A common strategy for trajectory tracking using hydraulic actuators is to use a cascaded control structure consisting of an inner and outer-loop controller [6]. The inner loop converts the hydraulic actuator, which is a velocity generator by nature, to a force generator. The outer-loop controls the trajectory by providing force commands to the inner loop. Hydraulic actuators are highly nonlinear systems [7]. For most applications a simple PID controller does not suffice as inner-loop controller due to its inability to adapt its behavior to the nonlinearities [8].

Fig. 1: The SIMONA Research Simulator

Incremental Nonlinear Dynamic Inversion (INDI) has proven its ability to accurately control nonlinear systems [9; 10]. INDI is an incremental sensor-based control strategy that calculates an increment to be added to the previous control input. At each increment measurements and properties of the mechanical system are used to obtain a linearized approximation of the system at that time step. This linearized approximation is used for the dynamic inversion. The dynamic inversion cancels the nonlinearities of the system. The resulting linear system can be controlled using conventional linear control approaches. INDI is less sensitive to model mismatches and uncertainties than other dynamic inversion controllers as it uses less model information. This decreased model dependency shifts the sensitivity from the accuracy of the model towards the accuracy of the measurements [11].

An inner loop INDI hydraulic controller has already been designed [1]. The inner loop controller is part of a larger controller for a Gough-Stewart platform flight simulator. In experiments on the SIMONA Research Simulator (SRS) at Delft University of Technology the performance and robustness of a conventional model-based controller [3] and the sensor-based INDI controller were compared. Figure 1 shows a picture of the SRS. In these experiments an increase in both performance and robustness to model uncertainties and mismatches was

found for the INDI controller as compared to the conventional model-based controller [1].

The flow to the hydraulic actuators of the SRS is controlled by electro-hydraulic servo-valves. The maximum output flow of a servo-valve is limited and therefore control input saturation occurs when this limit is reached. Saturation of the servo-valve might therefore bring forth undesirable phenomena such as wind-up [12] and could lead to instability [13]. This paper will discuss the effects of servo-valve saturations on the INDI controller and provide a solution do deal with these effects.

Pseudo Control Hedging (PCH) [14] is implemented in this paper to the inner loop controller to eliminate the negative consequences associated with the saturation. PCH adjusts the reference, such that adaptive elements in the controller will not observe certain characteristics of the system such as saturation. PCH has already been implemented successfully in other INDI controllers [15; 10]. This work shows that some adaptations will have to be made to the PCH to make the method suitable for the hydraulic servo-valve. The resulting controller adaptations to the inner loop INDI controller are evaluated through simulation and experiments on the SRS.

The hydraulic inner loop INDI controller requires the main spool position of the electro-hydraulic servo-valve. In the SRS the main spool position of the servo-valve is measured, but in practice it might be difficult to obtain these measurements. It is not standard practice for the manufacturers of the servo-valves to provide the user with a signal for this position. This work will therefore consider the use of a servo-valve model for the position instead. Through experiments on the SRS the performance of the adapted controller is evaluated.

Two loops in the INDI controller are responsible for the linearization of the system. The first loop is used for the incremental part of the controller. The second loop is used for the feedback of the state derivative. The importance of the synchronization of these loops for stability is shown in other works [15; 1]. A proof is given in this work that shows the importance of this synchronization with regard to time delays and filters. The results of experiments executed on the SRS with time delays in the inner loop INDI controller are discussed in this work.

The paper is organized as follows. The platform and input references used for the experiments are explained in section II. The general cascaded hydraulic control structure used to follow these references is discussed in section III. Section IV introduces the concept of INDI and the specific application of INDI to the hydraulic inner loop controller is treated in section V. The importance of the synchronization of the linearization loops of the INDI controller is shown in section VI. Section VII discusses effect of saturation on the inner loop INDI controller. The implementation and experimental evaluation of PCH is treated in section VIII. Section IX considers the use of a servo-valve model instead of measurements, which is then evaluated through experiments. The last section provides a conclusion of the main findings.

II. Methods

Solutions are provided to solve the three main problems related to saturation, delays and elimination of servo-valve measurements. The solutions were tested through experiments on the SRS at the faculty of Aerospace Engineering at Delft University of Technology.

The SRS is a hydraulic motion system with six degrees of freedom. Six hydraulic actuators with a stroke of 1.25 meter are connected to a platform such that it constitutes a Stewart platform. The extension of the actuators is measured using Heidenhain LC 415 linear encoders. A Rexroth 4WSE3EE15-15 three-stage servo-valve is connected to each hydraulic actuator. The position of its main spool is measured using the internal feedback signal. Each hydraulic actuator is equipped with a PAINE 210-60-090 pressure transducer to measure the pressure difference. The control loops run at 5 kHz.

The saturation is tested with an increasing sinusoidal heave reference. The heave signal increases in amplitude up until the point that the servo-valves start to saturate. The stability of the system is tested through a constant position reference such that the actuators are positioned in their neutral position. This point is the most critical point for stability due to the low damping ratio of the system at this point and the high flow gain [7]. The reference for the other experiments consists of a pre-positioning movement followed by a circular motion in the horizontal plane with pitch and roll, but no heave movement. The X and Y coordinates in the base frame for this reference are shown in Fig. 3.

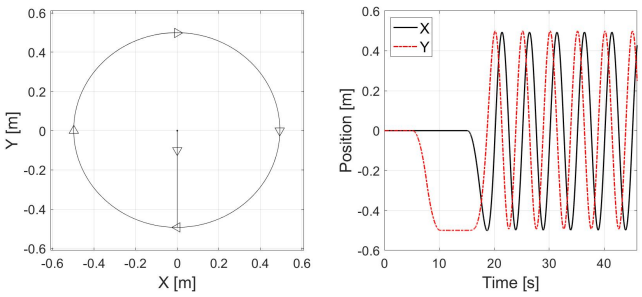

(a) XY - Plane (b) Time-series

Fig. 3: The circular trajectory reference

III. Cascaded hydraulic control structure

A common strategy for hydraulic motion control is to split up the control problem into two. An inner loop controls the force, while the outer loop controls the motion. This cascaded structure is used in the controller for the SRS [3]. The outer loop determines the desired position and velocity using inverse kinematics. The controller uses position and velocity feedback, and a feedforward force to calculate the force for the inner loop controller. The feedforward force is calculated using the inverse dynamics of the platform. The control law for the outer loop is shown in (1) and the complete controller is shown in Fig. 2. $\boldsymbol{F_{ref}}$ is the reference force, $\boldsymbol{F_{ff}}$ is the feedforward

force, K_P and K_D are the proportional and differential gain, $\boldsymbol{q_d}$ and $\dot{\boldsymbol{q}}_{\boldsymbol{d}}$ are the desired position and velocity, $\boldsymbol{q_m}$ and $\dot{\boldsymbol{q}}_{\boldsymbol{m}}$ are the measured position and velocity. The trajectory consists of position $\boldsymbol{z_d}$, the platform velocity $\dot{\boldsymbol{s}}_{\boldsymbol{d}}$ and the platform acceleration $\ddot{\boldsymbol{s}}_{\boldsymbol{d}}$. These can be used to calculate the corresponding actuator extensions using inverse kinematics. $\boldsymbol{P_{ref}}$ and $\boldsymbol{P_m}$ are the reference and measured pressure, $\boldsymbol{u}$ is the control input to the servo-valve, $\boldsymbol{x_m}$ is the measured main spool position of the servo-valve, and $\boldsymbol{\phi_1}$ and $\boldsymbol{\phi_2}$ are the flow rates from the servo-valve to the hydraulic actuator.

$$\boldsymbol{F_{ref}} = \boldsymbol{F_{ff}} + K_P(\boldsymbol{q_d} - \boldsymbol{q_m}) + K_D(\dot{\boldsymbol{q}}_{\boldsymbol{d}} - \dot{\boldsymbol{q}}_{\boldsymbol{m}}) \tag{1}$$

The inner loop pressure control is done using an existing INDI controller [1]. This controller and applied adaptations will be treated in the next sections.

IV. Incremental Nonlinear Dynamic Inversion

To understand the basic principle of INDI the control-affine system presented in (2) is considered. The system is approximated by a first-order Taylor expansion around the current moment in time and is presented in (3).

$$\dot{\boldsymbol{x}} = \boldsymbol{f}(\boldsymbol{x}, \boldsymbol{u}) + \boldsymbol{G}(\boldsymbol{x})\,\boldsymbol{u} \tag{2}$$

$$\begin{aligned}\dot{\boldsymbol{x}} \cong \dot{\boldsymbol{x}}_0 &+ \frac{\partial}{\partial \boldsymbol{x}}\left[\boldsymbol{f}(\boldsymbol{x}, \boldsymbol{u}) + \boldsymbol{G}(\boldsymbol{x})\right]_{\boldsymbol{x}=\boldsymbol{x}_0, \boldsymbol{u}=\boldsymbol{u}_0}(\boldsymbol{x} - \boldsymbol{x}_0) \\ &+ \frac{\partial}{\partial \boldsymbol{u}}\left[\boldsymbol{f}(\boldsymbol{x}, \boldsymbol{u}) + \boldsymbol{G}(\boldsymbol{x})\right]_{\boldsymbol{x}=\boldsymbol{x}_0, \boldsymbol{u}=\boldsymbol{u}_0}(\boldsymbol{u} - \boldsymbol{u}_0)\end{aligned} \tag{3}$$

When the sampling time is small and the dynamics of the actuator are considerably faster than the dynamics of the system it is possible to apply the *time-scale separation principle*. This principle assumes fast control action and a negligible change in state compared to the change in control input for small time increments [15]. Therefore, it is assumed that $\boldsymbol{x} = \boldsymbol{x_0}$ while $\boldsymbol{u} \neq \boldsymbol{u_0}$ so that equation 3 simplifies to (4).

$$\dot{\boldsymbol{x}} \cong \dot{\boldsymbol{x}}_0 + \boldsymbol{G}(\boldsymbol{x}_0)(\boldsymbol{u} - \boldsymbol{u}_0) \tag{4}$$

The INDI control law presented in (5) is obtained by rewriting (4) for the control input and choosing the state derivative $\dot{\boldsymbol{x}}$ as the new virtual control $\boldsymbol{\nu}$ ($\boldsymbol{\nu} = \dot{\boldsymbol{x}}$).

$$\boldsymbol{u} = \boldsymbol{u}_0 + \boldsymbol{G}^{-1}(\boldsymbol{x}_0)(\boldsymbol{\nu} - \dot{\boldsymbol{x}}_0) \tag{5}$$

V. Hydraulic force control using INDI

Figure 4 illustrates the thirds stage of a servo-valve and a hydraulic actuator, with compartment volumes V_1 and V_2, compartment pressures P_{p1} and P_{p2}, compartment leakage flows ϕ_{l1} and ϕ_{l2}, actuator extension q, piston area A_p, input flow rates ϕ_1 and ϕ_2, supply pressure P_s, return pressure P_t and servo-valve main spool position x_m. The pressure difference over the hydraulic actuator is defined by the difference between the two compartment pressures ($dP = P_1 - P_2$).

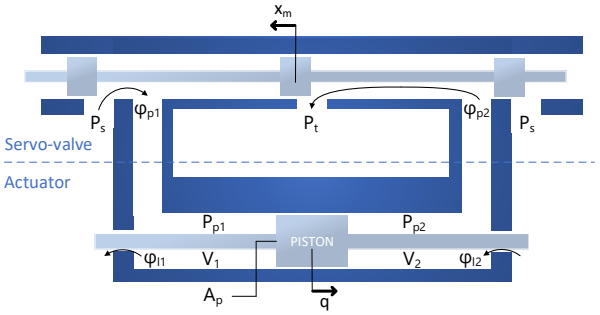

Fig. 4: The third stage of the servo-valve connected to the hydraulic actuator

The INDI principle has already been applied to hydraulic actuators by Huang et al. [1]. In this work the simple model presented in (6) is used to represent the hydraulic actuator, where the oil stiffness C_m is calculated using (7). ϕ_n is the maximum servo-valve flow, L_{lm} is the main leakage parameter of the hydraulic actuator, E is the oil bulk modulus and u is the control input to the actuator.

$$d\dot{P} = 2C_m(q)\left(\phi_n\sqrt{1 - \frac{x_m}{|x_m|}\frac{dP}{P_s}}u - L_{lm}dP - A_p\dot{q}\right) \tag{6}$$

$$C_m(q) = \frac{1}{2}\left(\frac{E}{V_1(q)} + \frac{E}{V_2(q)}\right) \tag{7}$$

Equation 8 represents the INDI control law for the hydraulic actuator and is derived by applying the general structure in (5) to (6), with the pressure difference derivative $d\dot{P}$ chosen as the virtual control ν and the control effectiveness $G(\boldsymbol{x}_0)$ given in (9), where $\boldsymbol{x} = (dP, x_m, q)$.

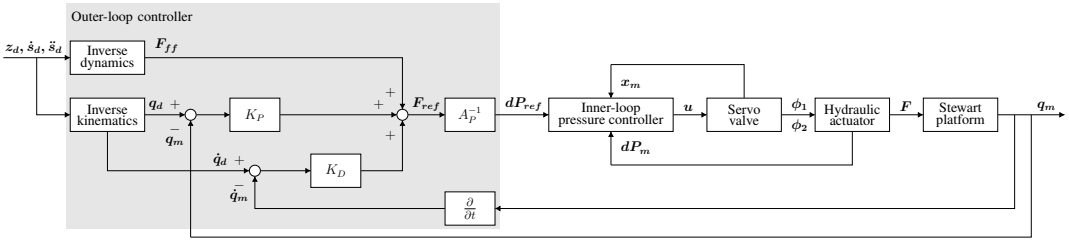

Fig. 2: Cascaded hydraulic control structure with a model-based outer loop controller

$$u = u_0 + G^{-1}(\boldsymbol{x}_0)\,(\nu - d\dot{P}_0) \tag{8}$$

$$G(\boldsymbol{x}_0) = C_m(q_0)\phi_n\sqrt{1 - \frac{x_{m0}}{|x_{m0}|}\frac{dP_0}{P_s}} \tag{9}$$

the inner loop control input is not directly sent to the hydraulic actuator. The servo-valve is present between the inner loop controller and the actuator. The main spool position should therefore be used instead of the previous control input, which is shown theoretically later in this section. Equation 8 is therefore rewritten to (10) with Δt as the time increment. (11) is obtained by transforming (10) to the Laplace domain. S^* represents the estimated valve dynamics.

$$u(t) = S^*\,u(t - \Delta t) + G^{-1}(\boldsymbol{x}_0)(\nu - \; d\dot{P}(t - \Delta t)) \tag{10}$$

$$U(s) = G^{-1}(\boldsymbol{x}_0)\frac{N(s) - e^{-\Delta ts}d\dot{P}}{1 - S^*(s)\,e^{-\Delta ts}} \tag{11}$$

Equation 12 is obtained when the valve-dynamics are taken into account and (4) is applied to the hydraulic system presented in (6). Equation 13 is the result of dividing the Laplace transform of (12) by $(1 - e^{-\Delta ts})$.

$$d\dot{P}(t) = d\dot{P}(t - \Delta t) + G(\boldsymbol{x}_0)(Su(t) - Su(t - \Delta t)) \tag{12}$$

$$d\dot{P}(s) = G(\boldsymbol{x}_0)\,S(s)\,U(s) \tag{13}$$

Insertion of (11) in (13) leads to (14). The transfer function from ν to $d\dot{P}$ presented in (15) is obtained by rewriting (14).

$$d\dot{P}(s) = \frac{S\,N(s) - S(s)\,e^{-\Delta ts}d\dot{P}}{1 - S^*(s)\,e^{-\Delta ts}} \tag{14}$$

$$\frac{d\dot{P}(s)}{N(s)} = \frac{S(s)}{1 - \; e^{-\Delta ts}(S^*(s) - S(s))} \tag{15}$$

It is assumed that the valve dynamics are perfectly estimated so that $S^* = S$. In this case the denominator of (15) will become 1 and (16) is obtained. Only the valve dynamics remain, which is to be expected as they are not taken into account by the inversion. It is therefore important to include the dynamics in the incremental loop as the performance is otherwise harmed as shown by (15) . It is also possible that the denominator introduces right half-plane (RHP) poles that could lead to instability.

$$d\dot{P}(s) = S(s)\,N(s) \tag{16}$$

In the SRS the dynamics are included by measuring the main spool position x_m. Filters F_1 and F_2 are placed on the incremental and pressure difference derivative feedback loops. F_1 and F_2 are second-order low-pass filters that need to be equal for stability and performance reasons [1]. The only difference is that F_2 includes a differentiator term as the pressure difference is measured and its derivative is needed. A second-order low-pass filter F_3 is placed on the pressure feedback signal for the linear controller and a specifically designed prefilter F_5 [8] on the reference pressure signal. The control input is passed through a first-order low-pass filter F_4. The complete inner loop controller is shown in Fig. 5.

Experiments were conducted on the SRS for the cascaded hydraulic controller with an inner loop INDI controller. The integral gain K_I is varied for the linear controller of the INDI controller. The extension reference for leg 1 is shown in Fig. 6. The error for the extension of leg 1 is shown in Fig. 7.

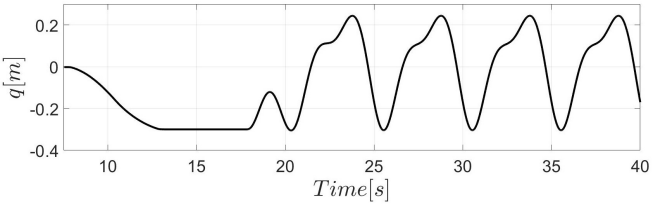

Fig. 6: Outer loop extension reference for leg 1 for the circular trajectory

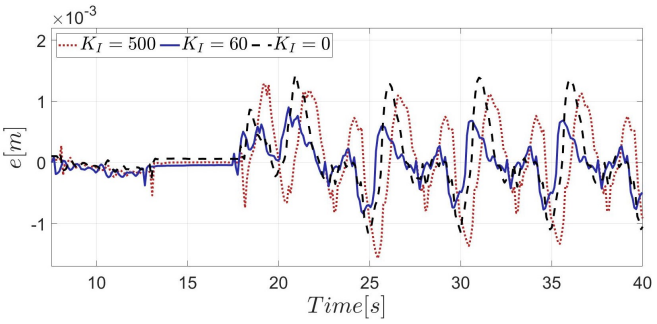

Fig. 7: Extension tracking errors of leg 1 for varying K_I during circular trajectory tracking experiments

The best outer loop tracking performance for leg 1 is achieved for $K_I = 60$ as the tracking error is consistently below 1 mm for this gain and drops the maximum error from 1.43mm to 0.93mm. Worse outer loop performance is obtained for $K_I = 500$, in contrast to the inner loop pressure tracking. The normalized pressure difference error is smaller for $K_I = 500$ as shown in figure 8. Better inner loop tracking does therefore not necessarily result in better outer loop tracking. The cascaded controller should be optimized simultaneously using strategies like Multi-Objective-Parameter-Optimization [16] [17].

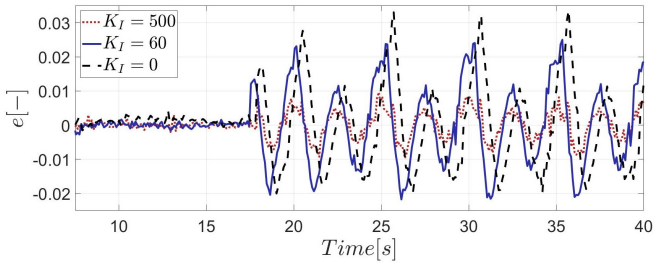

Fig. 8: Normalized pressure difference tracking errors of leg 1 for varying K_I during circular trajectory tracking experiments

VI. Synchronization of the Linearization Loops

The importance of synchronization of the linearization loops has been shown in terms of equivalent filters [1]. It is known as well that it is important to keep the delays in the loops equal [10]. In order to demonstrate the importance of the synchronization of the delays, consider the continuous-time controller as shown in Fig. 9. The linearization loops in this controller contain the filters A and B, time increment Δt, and delays d_1 and d_2. A and B represent general filters, which are used to demonstrate the overall effect of filters on the system.

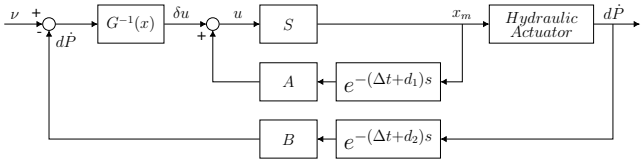

Fig. 9: The INDI linearization loops with delays and filters

The relation presented in (17) can be found from Fig. 9. This can be rewritten for the input such that (18) is obtained.

$$U(s) = U(s)Se^{-(\Delta t+d_1)s}A + G^{-1}(\boldsymbol{x}_0)(N(s) - d\dot{P}e^{-(\Delta t+d_2)s}B) \tag{17}$$

$$U(s) = G^{-1}(\boldsymbol{x}_0)\frac{N(s) - d\dot{P}e^{-(\Delta t+d_2)s}B}{1 - Se^{-(\Delta t+d_1)s}A} \tag{18}$$

The transfer function from the virtual input to the pressure difference derivative presented in (19) is obtained when (18) is inserted in (13) and rewritten.

$$\frac{d\dot{P}(s)}{N(s)} = \frac{S}{1 - S(s)e^{-\Delta ts}(Ae^{-\Delta d_1 s} - Be^{-\Delta d_2 s})} \tag{19}$$

Equation 19 shows that an additional term is present in the denominator that reduces the control performance if the delays and filters are not equal. This extra term could even introduce poles in the RHP that may lead to instability. In order to illustrate this, it is now assumed that the filters equal 1, the sampling time is 0, the delay d_1 equals 0 and that the valve dynamics also equal 1. Equation 20 is then obtained from (19). A first order Padé approximation of (20) leads to (21) [18].

$$\frac{d\dot{P}(s)}{N(s)} = \frac{1}{e^{-d_2 s}} \tag{20}$$

$$\frac{d\dot{P}(s)}{N(s)} \cong \frac{\frac{2}{d_2} - s}{\frac{2}{d_2} + s} \tag{21}$$

Equation 21 shows that any nonzero positive delay d_2 will introduce RHP poles when no valve-dynamics are present, the sampling time is 0, and no delay is present in the incremental loop. This simple case illustrates the general possibility of RHP poles to be introduced in the system due to the additional term in the denominator. Therefore, it is important to keep the filters and delays equal so that this term disappears. In practice this would mean that the delays will have to be either measured or determined by means of a detailed system analysis.

On the SRS an experiment with delay has also been executed. 7 ms of delay was present in the outer linearization loop that feeds back the pressure difference derivative. The delay led to instability for a neutral position reference. The inner loop pressure response for this scenario is shown in Fig. 10.

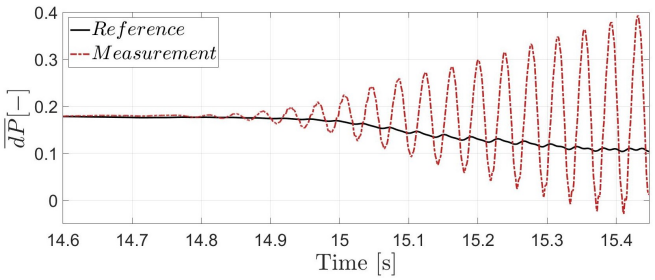

Fig. 10: Normalized pressure difference response during a neutral position tracking experiment with 7ms delay in the pressure measurement

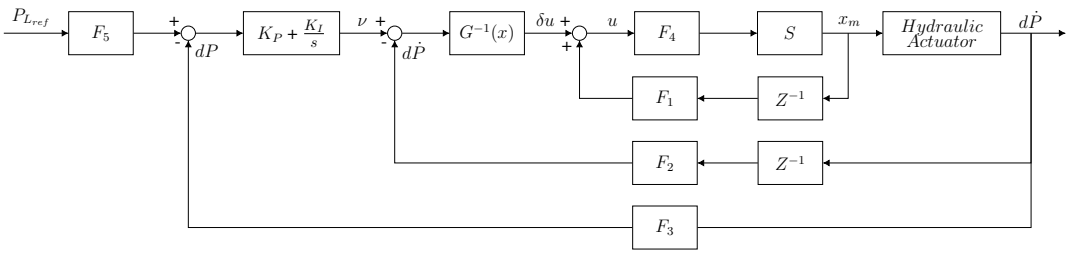

Fig. 5: Block diagram of the inner loop INDI controller including the filter design

VII. Effects of saturation

A pressure reference is tracked in simulation to better understand the effects of saturation on the inner loop controller. The reference is tracked for $K_I = 1500$ and $K_I = 0$. The simulation results are shown in figure 11.

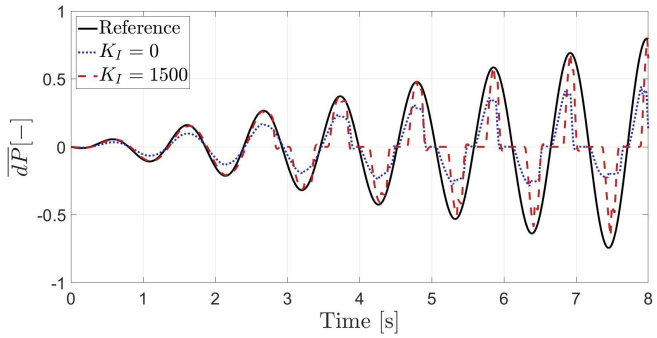

Fig. 11: Simulation of inner loop tracking of a normalized pressure difference reference that leads to servo-valve saturation for varying K_I

Figure 11 shows that the controller with integral action is better in tracking up until the points where the saturation starts. During saturation the pressure drops, because the hydraulic actuator is a velocity generator. When the velocity stagnates it means that the acceleration as well as the pressure drop to zero. After saturation the controller should track the reference again. The controller without integral action has lower performance before saturation, but after saturation it is able to quickly follow the reference again. For the controller with integral action wind-up occurs during saturation. The wind-up has to be countered after saturation, leading to delayed tracking. Figure 12 shows that the controller with integral action is winding up as the value reaches above 1 for the normalized input. For the controller without integral action it is bounded as the amount above 1 for the normalized input is equal to the increment and does not increase with time.

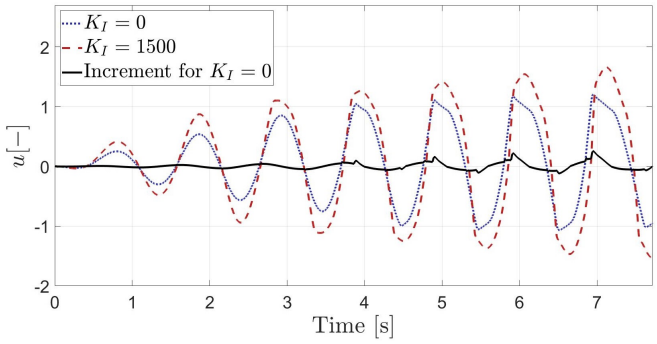

Fig. 12: The inner loop command in the simulation with a pressure reference that leads to servo-valve saturation for varying K_I

In experiments on the SRS similar results were found in motion tracking with servo-valve saturation for the controller without integral action as shown in Fig. 13. The controller directly tracks the reference after saturation and no wind-up effects are present. No experiments have been executed with the controller with integral action to prevent damage to the simulator.

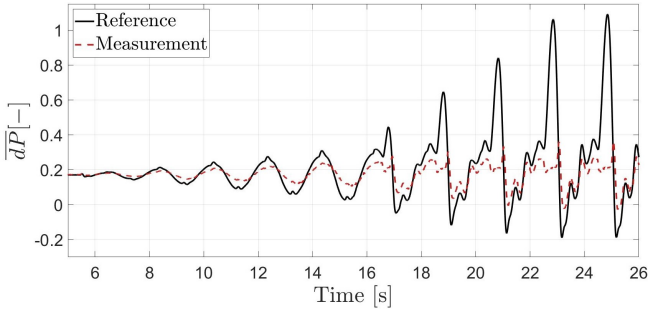

Fig. 13: Normalized pressure difference tracking errors of leg 1 for the sinusoidal heave reference that leads to servo-valve saturation with $K_I = 0$

The integral action therefore degrades the control performance during saturation and the wind-up could lead to unexpected effects in the simulator. The addition of this gain does however increase the control performance when no saturation is present.

VIII. Pseudo Control Hedging

PCH is a method that prevents adaptive elements in the controller from acting upon certain system characteristics such as saturation [14]. It uses the difference between the control input and the effective amount of control input to the actuator to determine the amount that it should hedge back the reference. The hedge is subtracted through a reference model.

The control law for the INDI controller as presented in (5) can be rewritten for the virtual control such that (22) is obtained. The difference between the commanded and the effective virtual control is determined to obtain the amount of ineffective virtual control to be hedged, which is presented mathematically in (23).

$$\nu = \dot{x}_0 + G(\boldsymbol{x}_0)(u - u_0) \tag{22}$$

$$\nu_h = \nu_{com} - \nu_{eff} \tag{23}$$

The virtual control hedge in (24) is obtained through insertion of (22) in (23) for both the commanded and effective virtual control. This is simplified to (25) [10].

$$\nu_h = [\dot{\boldsymbol{x}}_0 + G(\boldsymbol{x}_0)(u_{com} - u_0)] - [\dot{\boldsymbol{x}}_0 + G(\boldsymbol{x}_0)(u_{eff} - u_0)] \tag{24}$$

$$\nu_h = G(\boldsymbol{x}_0)\,(u_{com} - u_{eff}) \tag{25}$$

For the servo-valve the effective input equals the measurement of the main spool position, which results in (26).

$$\nu_h = G(\boldsymbol{x}_0)\,(u_{com} - x_m) \tag{26}$$

Use of the main spool measurement does degrade the overall performance of the controller. The hedge subtracts any ineffective input due to the dynamics of the servo-valve and not only the amount due to saturation. The servo-valve has a known saturation point, which can be used to only subtract the ineffective input due to saturation. This is done by hedging back any amount above the known saturation point. The adaptation to the hedge is shown in (27).

$$\nu_h' = G(\boldsymbol{x}_0)\left(u_{com} - sat(u_{com})\right) \tag{27}$$

This hedge is subtracted from the reference using a reference model. For this controller a first order low-pass filter is used as reference model, which is shown in Fig. 14.

The PCH gain K_{PCH} is needed, because the effectiveness of the hedge is dependent on the magnitude of the reference model gain K_{ref}. This is shown by the transfer function from the virtual control hedge to the hedged pressure reference dP_h shown in (28), where the effectiveness of the hedge decreases with increasing reference model gain.

$$\frac{dP_h}{N_h} = \frac{1}{s + K_{ref}} \tag{28}$$

The complete inner loop controller including integral action and the implementation of PCH is shown in Fig. 14. In an experiment on the SRS a heave signal with an increasing amplitude through time is used to test the implementation of the PCH. The inner loop pressure tracking is shown in Fig.15.

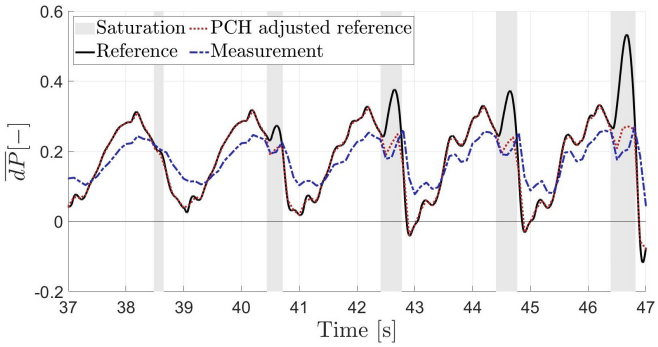

Fig. 15: Experimental results of inner loop normalized pressure tracking with saturation and PCH

Figure 15 shows that the reference and the corrected reference only differ when saturation has occurred. The PCH is adjusting the reference such that the inner loop controller will not adapt to the saturation. The saturation is finished when the two references align again. After saturation the measurements follow both references again, which indicates that there are no significant wind-up effects. Fig. 17 shows the that the inner loop control input to the servo-valve also remains bounded.

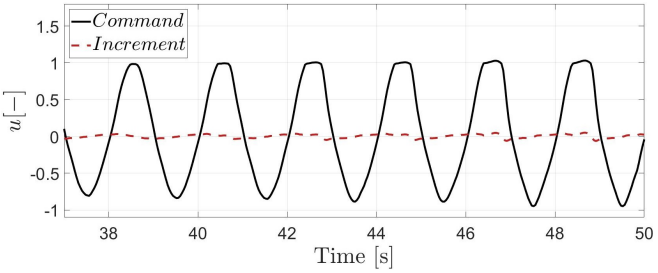

Fig. 17: Commands to the servo-valve of leg 1 in the experiment for the controller with PCH implemented

Figure 17 shows that the control input to the servo-valve remains bounded. The control input reaches above 1, but this amount equals the increment. The amount above 1 can therefore be subtracted from the command without consequence, as no significant wind-up is occurring anymore. The outer loop extension tracking and tracking error are shown in Fig. 18.

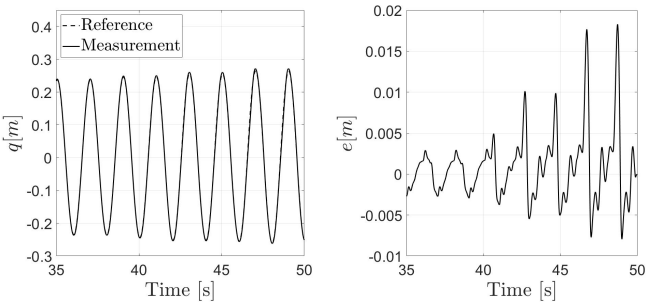

(a) Extension tracking (b) Extension tracking error

Fig. 18: Actuator extension tracking of leg 1 in the experiment for the controller with PCH implemented

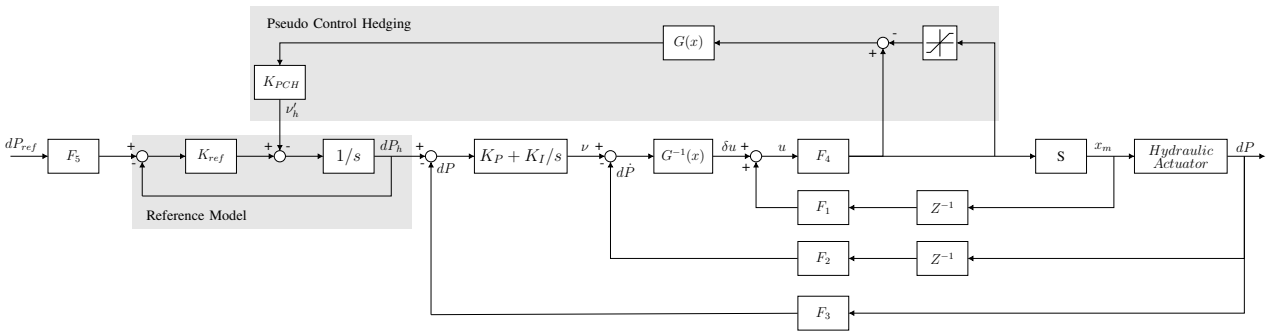

Fig. 14: Inner loop INDI controller including the adapted PCH and reference model

The responses show degraded performance during saturation, but stable behavior. No wind-up effects are to be found in this figure either. Therefore, the PCH is working as expected and prevents the negative effects due to wind-up in the inner loop controller.

IX. INDI WITHOUT SERVO-VALVE MEASUREMENTS

The INDI controller uses measurements of the main spool position for the incremental loop, which might be difficult to acquire in practice. It might easier to use a servo-valve model. The adapted controller with valve model S_m is shown in Fig. 16. Manufactures often provide information to model valves as first- or second-order transfer functions. The structure of the models is shown in (29) and (30), with τ_s the time constant, and ω_n and ς the apparent natural frequency and damping of the servo-valve. For the servo-valves of the SRS a τ of 0.2, an ω_n of $2 \cdot \pi \cdot 167$ and a ς of 0.55 were used.

$$S_m = \frac{1}{\tau s + 1} \quad (29) \qquad S_m = \frac{\omega_n^2}{s^2 + 2\varsigma\omega_n + \omega_n^2} \quad (30)$$

Experiments are conducted on the SRS using the adapted inner loop INDI controller that uses servo-valve models instead of measurements. The inner loop responses and the control errors are shown in Figs. 19 and 20 respectively.

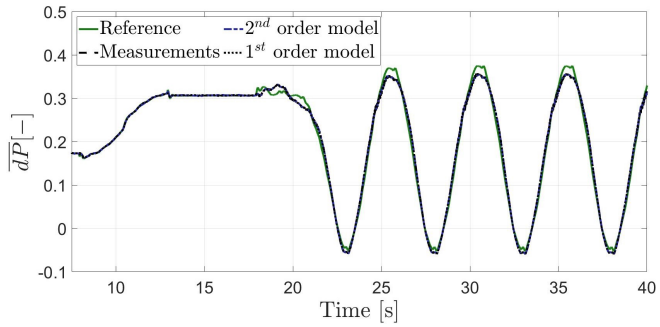

Fig. 19: Experimental results of normalized pressure difference tracking using different valve models

Figures 19 and 20 show no significant differences in terms of stability and performance between the three controllers. It is therefore possible to replace the servo-valve measurements by a first- or second-order model. This simplifies the design and implementation of INDI controllers for hydraulic actuators with servo-valves, as the models can be derived from the data provided by the manufactures of the servo-valves. A first-order model suffices for this trajectory and an easy way to derive the model would therefore be to determine the time constant using the data provided in the datasheets of the servo-valve.

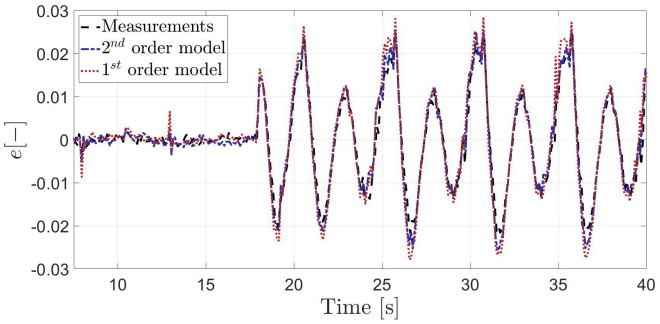

Fig. 20: Experimental results of the normalized inner loop tracking error for different valve models

X. DISCUSSION & CONCLUSION

This paper discussed some of the challenges and accompanying solutions for incremental nonlinear control applied to hydraulic parallel robots. The solutions have been implemented in an existing hydraulic INDI force controller [1], which is part of a larger cascaded motion controller. The solutions were evaluated experimentally on the SRS.

It is found that the addition of integral gain to the linear controller in the inner loop INDI force controller leads to increased tracking performance for both controllers in the cascaded structure. However, there is a point where the inner loop tracking improves and the outer loop tracking decreases through further increase of the integral gain. Better inner loop tracking does therefore not necessarily lead to better outer loop tracking. The best outer loop tracking was obtained for $K_I = 60$, which reduced the maximum absolute extension error by 30% to around 1mm.

The integral action does wind up during saturation. Therefore, PCH is implemented. The PCH subtracts the ineffective control due to saturation of the servo-valve from the inner loop pressure reference. Through experiments is is found that the adjustment successfully prevents the negative effects due to wind-up of the integral action during saturation. The implementation therefore allows for increased performance as it is possible to safely incorporate integral action in the inner loop controller.

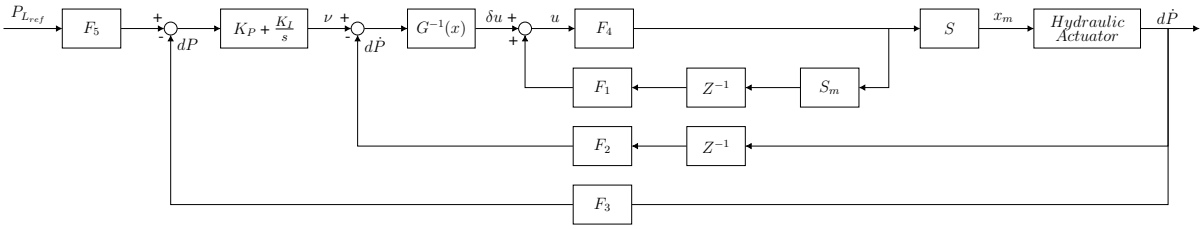

Fig. 16: Block diagram of the inner loop INDI controller including the filter design and servo-valve model adaptation

Furthermore, the importance of the synchronization of the delays for the linearization loops of the INDI controller has been shown analytically and experimentally on the SRS. When the mismatch in delay is too large it leads to instability. The synchronization of delays in these loops is therefore essential in the design and implementation of an INDI controller. The delays should be measured or determined through a thorough system analysis in order to synchronize them.

Finally, it is found through experiments that it is possible to replace servo-valve measurements in the INDI controller by a first- or second-order servo-valve model without losing stability or significant performance. The use of such a model simplifies the implementation and design of the INDI controller, as manufacturers often provide the user with information to model the servo-valve as a first- or second-order transfer function.

Incorporation of this inner loop controller in an outer loop INDI motion controller [19], the extension of PCH to the outer loop motion controller, simultaneous optimization of both loops in the cascaded controller using Multi-Objective Parameter Optimization [16] [17] and the application of more advanced filtering techniques to the measurement signals are interesting directions for future research.

REFERENCES

[1] Y. Huang, "Incremental nonlinear control of hydraulic parallel robots: An application to the simona research simulator," Ph.D. dissertation, Delft University of Technology, 2019.

[2] A. Alleyne and R. Liu, "A simplified approach to force control for electro-hydraulic systems," *Control Engineering Practice*, vol. 8, no. 12, pp. 1347–1356, 2000.

[3] S. Koekebakker, "Model based control of a flight simulator motion system," Ph.D. dissertation, Delft University of Technology, 2001.

[4] T. Boaventura, C. Semini, J. Buchli, M. Frigerio, M. Focchi, and D. G. Caldwell, "Dynamic torque control of a hydraulic quadruped robot," in *2012 IEEE international conference on robotics and automation*. IEEE, 2012, pp. 1889–1894.

[5] A. Alleyne, R. Liu, and H. Wright, "On the limitations of force tracking control for hydraulic active suspensions," in *Proceedings of the 1998 American Control Conference. ACC (IEEE Cat. No. 98CH36207)*, vol. 1. IEEE, 1998, pp. 43–47.

[6] J. Heintze and A. Van Der Weiden, "Inner-loop design and analysis for hydraulic actuators, with an application to impedance control," *Control Engineering Practice*, vol. 3, no. 9, pp. 1323–1330, 1995.

[7] D. Noah and R. Fales, *Hydraulic Control Systems*, 2nd ed. John Wiley & Sons, 9 2019.

[8] G. van Schothorst, "Modelling of long-stroke hydraulic servo-systems for flight simulator motion control and system design," Ph.D. dissertation, Delft University of Technology, 8 1997.

[9] R. Da Costa, Q. Chu, and J. Mulder, "Reentry flight controller design using nonlinear dynamic inversion," *Journal of Spacecraft and Rockets*, vol. 40, no. 1, pp. 64–71, 2003.

[10] P. Simplício, M. Pavel, E. Van Kampen, and Q. Chu, "An acceleration measurements-based approach for helicopter nonlinear flight control using incremental nonlinear dynamic inversion," *Control Engineering Practice*, vol. 21, no. 8, pp. 1065–1077, 2013.

[11] S. Sieberling, Q. Chu, and J. Mulder, "Robust flight control using incremental nonlinear dynamic inversion and angular acceleration prediction," *Journal of guidance, control, and dynamics*, vol. 33, no. 6, pp. 1732–1742, 2010.

[12] Q. Guo, J. Yin, T. Yu, and D. Jiang, "Saturated adaptive control of an electrohydraulic actuator with parametric uncertainty and load disturbance," *IEEE Transactions on Industrial Electronics*, vol. 64, no. 10, pp. 7930–7941, 2017.

[13] D. Y. Abramovitch and G. F. Franklin, "On the stability of adaptive pole-placement controllers with a saturating actuator," in *26th IEEE Conference on Decision and Control*, vol. 26. IEEE, 1987, pp. 825–830.

[14] E. N. Johnson and A. J. Calise, "Pseudo-control hedging: A new method for adaptive control," in *Advances in navigation guidance and control technology workshop*. Alabama, USA, 2000, pp. 1–2.

[15] R. van't Veld, E.-J. Van Kampen, and Q. P. Chu, "Stability and robustness analysis and improvements for incremental nonlinear dynamic inversion control," in *2018 AIAA Guidance, Navigation, and Control Conference*, 2018, p. 1127.

[16] F. Grondman, G. Looye, R. O. Kuchar, Q. P. Chu, and E.-J. Van Kampen, "Design and flight testing of incremental nonlinear dynamic inversion-based control laws for a passenger aircraft," in *2018 AIAA Guidance, Navigation, and Control Conference*, 2018, p. 0385.

[17] H.-D. Joos, "A multiobjective optimisation-based software environment for control systems design," in *Proceedings. IEEE International Symposium on Computer Aided Control System Design*. IEEE, 2002, pp. 7–14.

[18] G. J. Silva, A. Datta, and S. Bhattacharyya, "Controller design via padé approximation can lead to instability," in *Proceedings of the 40th IEEE Conference on Decision and Control (Cat. No. 01CH37228)*, vol. 5. IEEE, 2001, pp. 4733–4737.

[19] Y. Huang, D. Pool, O. Stroosma, and Q. Chu, "Robust incremental nonlinear dynamic inversion controller of hexapod flight simulator motion system," in *Advances in Aerospace Guidance, Navigation and Control*. Springer, 2018, pp. 87–99.

II

Preliminary Report

This part of the thesis has already been graded and is included only for convenience. This part should therefore not be considered for the final grading.

Nomenclature

$\bar{\phi}_m$	Normalized flow from the second to the third stage of the servo-valve
$\bar{i}_{ca}$	Normalized input current to the torque motor
$\bar{u}$	Normalized input signal to the servo-valve
$\bar{x}_m$	Normalized thirds stage spool position
$\bar{x}_s$	Normalized second stage spool position
$\boldsymbol{\beta}$	Matrix containing inertial properties of leg i
$\dot{\boldsymbol{s}}$	Platform velocity vector
$\boldsymbol{\omega}_p$	Angular velocity vector of the platform
$\boldsymbol{\phi}$	Euler angles for the transformtation between reference frame a and b
$\boldsymbol{F}$	Vector containing the input actuator forces
$\boldsymbol{f}$	vector field in $\mathbb{R}^n$
$\boldsymbol{G}$	$n \times m$ control effectiveness matrix
$\boldsymbol{g}$	gravity vector
$\boldsymbol{H}$	Vector containing the column input output transformations
$\boldsymbol{h}$	vector field in $\mathbb{R}^m$
$\boldsymbol{M}$	Matrix containing inertial properties of leg i
$\boldsymbol{Q}_i$	Matrix containing inertial properties of leg i
$\boldsymbol{R}_i$	Position vector for the centre of gravity of the platform
$\boldsymbol{V}_i$	Matrix containing dynamic properties of leg i
$\boldsymbol{x}$	state vector
$\boldsymbol{z}$	Platform position vector
$\delta\nu$	virtual control increment of the INDI controller
η	dynamic viscosity of the oil
λ_i	natural frequency i of the transmission lines
μ_0	gap normal in the magnetic flux direction
ν	virtual control of the INDI controller
ν_{kin}	kinematic viscosity
ϕ_n	maximum servo-valve flow
ϕ_{0i}	flow i through the inlet restrictions of the second stage
$\phi_{l,bi}$	leakage flow for bearing i of the hydraulic actuator

$\phi_{l,mi}$ third stage leakage flow for port i

$\phi_{l,si}$ servo-valve second stage leakage flow for port i

ϕ_{mi} second stage output flow i

ϕ_{ni} first stage output flow i

ϕ_{oi} output flow i from the transmission line

ϕ_{pij} input flow j to the transmission line

ϕ_{pi} Flow i to the hydraulic actuator

ρ oil density

A_0 inlet restriction orifice area of the second stage

A_m main spool piston area

A_p piston area of the hydraulic actuator

A_s second stage spool side area

A_{mi} main spool port opening area i

A_{n3} orifice area of the second stage

$A_{p,bi}$ Virtual piston area for bearing i

A_{si} servo-valve second stage spool port opening area i

B_a viscous friction coefficient of the flapper

C_i^* adjusted filter i for the inner loop controller

c_0 Speed of sound in oil

c_b servo-valve ball clearance

C_d discharge coefficient for the turbulent flow

C_i filter i for the inner loop controller

c_i Identified coefficients for the fourth and fifth order servo-valve models

c_{rm} radial clearance of the main spool and the bushing

c_{rs} radial clearance of the second stage spool and the bushing

D_n nozzle diameter of the second stage

D_nt Dissipation number for the transmission lines

d_{mi} port underlap for port i

d_{si} port underlap for port i of the second stage

E oil bulk modulus

E_a Body frame attached to the moving platform

E_b Inertial frame attached to the static base

f_1 Function describing the servo-valve nonlinearities

F_{act} generated force by the hydraulic actuator

F_{ax} axial force working on the second stage spool

F_{cs} force due to coulomb friction on the second stage spool

F_{ff} feedforward force

F_{ref} reference force

h_m main spool port opening width

h_s second stage spool port opening width

i_{ca} input signal to the torque motor of the electro-hydraulic servo-valve

J_a inertia of the flapper

K_a equivalent flapper spring constant

K_p proportional gain for the linear controller of the inner loop controller

$K_{\Delta P}$ feedforward pressure difference gain

$K_{\dot{q}}$ actuator velocity error gain

K_b torque motor magnetic stiffness

K_{ca} torque motor current amplifier gain

K_c inner loop action controller gain

K_{dm} differential third stage feedback gain

K_D actuator velocity error gain of the outer loop controller

K_{fbs} servo-valve mechanical feedback spring constant

K_{lv} varying inner loop servo-valve input normalizing gain

K_l inner loop controller leakage gain

K_{PCH} pseudo control hedging effectiveness gain for the inner loop controller

K_{pm} proportional third stage feedback gain

K_P actuator extension error gain of the outer loop controller

K_q actuator extension error gain

K_{REF} reference model gain for the inner loop controller

K_t torque motor gain

K_v inner loop controller velocity gain

L transmission line length

l_a servo-valve armature length

l_{fbs} servo-valve feedback spring length

l_f servo-valve flapper length

L_{lm} main leakage parameter of the hydraulic actuator

LP_{bi} Laminar leakage coefficient for bearing i

M_s mass of the second stagespool

M_0 magnetomotive force

N number of windings of the coil for the torque motor

P_L Pressure differences between the two chambers of the hydraulic actuator

P_s supply pressure

P_t return pressure

P_{ff} feedforward pressure difference

P_{mi} second stage output pressure i

P_{n3} Nozzle outlet pressure of the second stage

P_{ni} first stage output pressure i

P_{oi} output pressure i from the transmission line

P_{pij} input pressure j to the transmission line

P_{pi} flow i to the hydraulic actuator

P_{pi} pressure i to the hydraulic actuator

q actuator extension

q_d desired atuator extension

r_h cross-section radius of the transmission line

T_t torque generated by the torque motor

T_{fbs} torque due to the mechanical feedback link between the torque motor and the second-stage spool

T_{ff} torque due to the nonlinear flow forces on the flapper

u input to the electro-hydraulic servo-valve

V_m Actuator volume at middle position

w_0 viscuous friction coefficient of the second stage spool

w_s force due to coulomb friction on the second stage spool

x_s second stage spool position

x_{f0} distance between the flapper and nozzle in neutral position

x_f flapper deflection distance at the nozzles

x_g flapper deflection distance at the tip

x_m servo-valve third stage spool position

Z_0 undamped natural frequencies of node i of the transmission lines

List of Figures

List of Tables

1

Introduction

In 1904 a man named Edwin Albert Link was born. Edwin had a passion for flying and his father owned a piano and organ factory where he also worked at. Edwin did however encounter one problem with flying as it was very expensive at the time to learn how to do it. He wanted to address this problem and used his skills from his job at the factory to create what is now known as the first commercial flight simulator. His flight simulator was not taken seriously at the start and was mainly used by theme parks, but when the second World War arrived it was found that it was an effective way to train airmen more cheaply. Edwin demonstrated one of the benefits of a flight simulator, which is cost effectiveness. Other important factors include safety and eco-friendliness. For the same reasons the SIMONA project was proposed by S.K. Advani in 1901 [3] and initiated in 1902. The project included the realization of the SIMONA Research Simulator (SRS). With the simulator it is possible to do research in various field in a more cost-effective, save and eco-friendly way. The SRS is a flight simulator that can move with six degrees of freedom and it is desirable to control this movement as accurately as possible. This master thesis will address the control of the SRS both on the level of simulations as well as experiments.

1.1. SIMONA Research Simulator

The SIMONA Research Simulator (SRS) is a 6 DoF parallel robot that contains a platform with six hydraulic legs connected to it. The legs exert forces on the platform allowing it to move. The legs are connected in pairs to three points on the platform such that a Gough-Stewart platform is obtained. Each hydraulic leg contains an electro-hydraulic servo-valve and hydraulic actuator which are connected by means of transmission lines.

Figure 1.1: The Simona Research Simulator located at the faculty of aerospace engineering at Delft University of Technology

1.2. Parallel robots

A parallel robot is a mechanism of which the end-effector is supported by multiple kinematic chains as opposed to serial robots where the end-effector is supported by only one kinematic chain. A schematic representation of a parallel and serial robot is presented in figure 1.2. Parallel robots possess various advantages over serial robots as they generally have higher stiffness, better dynamic performance [29] and few moving masses. The disadvantage is that they have complex models that often require complex and expensive computations [32].

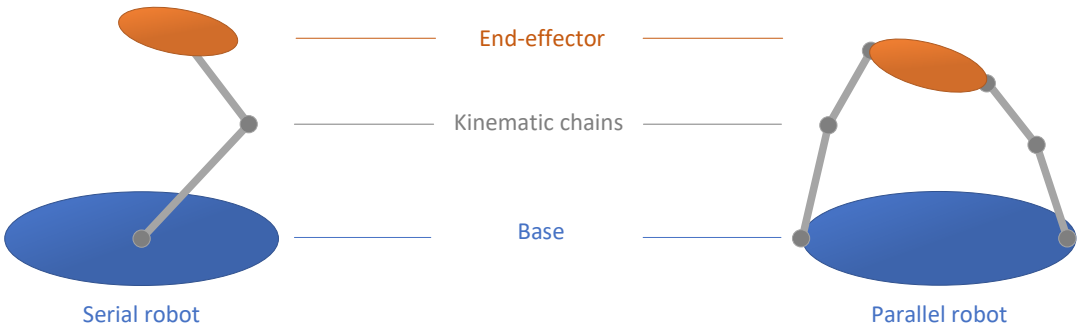

Figure 1.2: Differences between serial and parallel robots

1.3. Gough-Stewart Platform

The Gough-Stewart platform is a specific type of parallel robot that has a a platform as end-effector which is moved by six linear actuators which are connected to the base [37]. [12] The Stewart platform has six degrees of freedom and is suitable for high-performance tasks such as simulation due to its high accuracy potential and high load capacity [24]. [39] The Gough-Stewart platform was therefore also chosen for the SRS due to the high loads and need for accuracy. A schematic representation of a Gough-Stewart platform can be seen in figure 1.3.

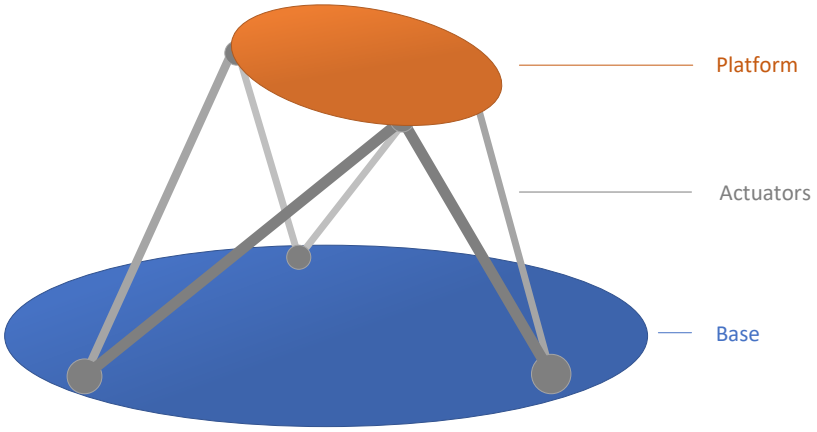

Figure 1.3: A schematic representation of a Stewart platform

1.4. Hydraulic control valves

A hydraulic servo system makes use of a valve that controls the flow. Such a valve converts the electrical/mechanical signal into a corresponding hydraulic power through movement of the spool. Several control valve types exist and a main distinction can be made between on-off, proportional, and servo control valves.

As the name suggests on-off valves can be either switched on or off which results in limited control performance as only two states for the spool can be used to steer the system. These type of valves are however the cheapest valves as the electronics are simple as well as the mechanical structure.

When the spool can be placed at any position between its outer limits it is referred to as a proportional control valve. A proportional control valve therefore will allow for better control performance as any position between the two outer limits can be achieved. These types of valves mostly make use of proportional solenoids without position feedback to control the spool position [30].

Most servo valves use sensors to measure the spool position which can be used as feedback for the control of this spool position. A schematic of an electro-hydraulic two-stage servo-valve is shown in figure 1.4 as clarification. Adding sensors such as a LVDT can improve the control performance of the system but also adds cost to the valve [38]. The feedback of the position is generally included because of hysteresis and nonlinearity [41].

Proportional valves have a slower response than servo-valves due to the fact that they have less force available as they are directly exerting a force on the spool [45], larger dead band due to the fact that they are often machined with less precision, and have more hysteresis [44]. They were however a lot cheaper than the servo-valves and more reliable [23] .

The SRS needs to be accurately controlled and therefore electro-hydraulic servo-valves are used to control the flow to the hydraulic actuators. The servo-valve used for the SRS is a three-stage electro-hydraulic servo-valve. A magnetic torque motor drives a flapper that controls the pressure on the spool of the second stage which will in turn move. Due to the movement the flow is allowed to move through the output ports of the second stage to the third stage which again drives another spool which is called the main spool. The thirds stage has the purpose of power amplification. The output flows of the third stage are transferred by means of transmission lines to the hydraulic actuator. If another spool stage would be added to the two-stage valve configuration as shown it would entail a three-stage valve.

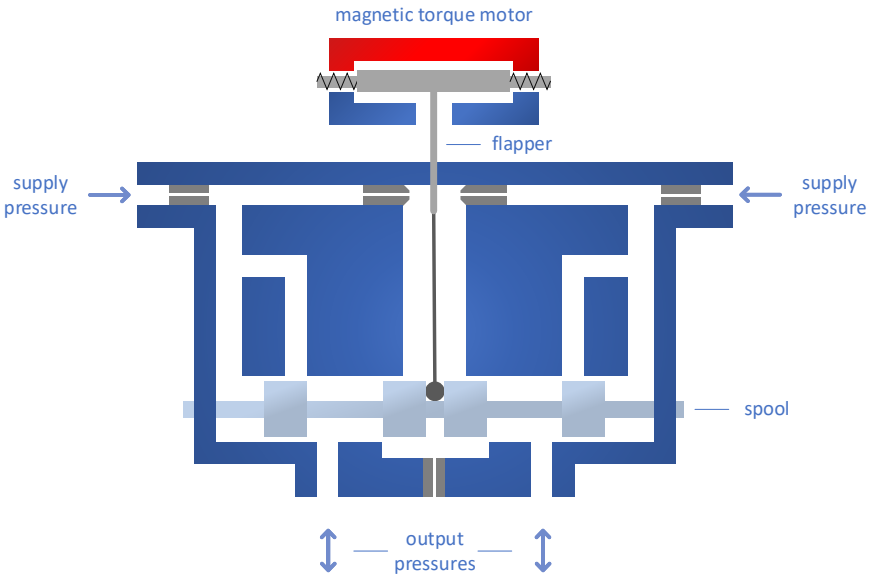

Figure 1.4: A schematic representation of a two-stage electro-hydraulic servo-valve

The servo-valve is a highly nonlinear system due to phenomena such as torque-motor nonlinearities which cause deviations in the the dynamics behavior for large inputs and non-linear spool port flows which influences the flow gains and equilibrium pressures [39].

1.5. Hydraulic Actuators

The servo-valve outputs two pressures to the hydraulic actuator that creates a pressure difference between the two sides of the piston. The piston will in turn exert a force on the platform through the rod connected to it. Several linear hydraulic actuators exist such as double-rod, single-rod and double-concentric linear actuators. A schematic drawing of the different types of linear hydraulic actuators is shown in figure 1.5.

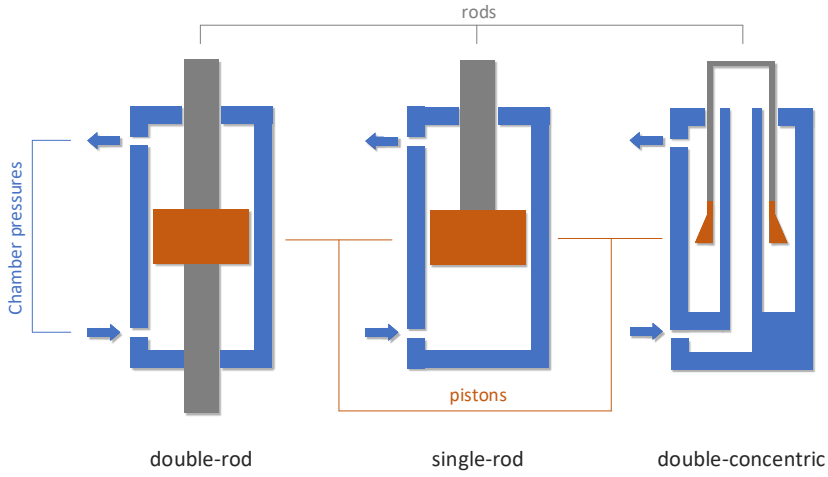

Figure 1.5: Schematic representation of linear hydraulic actuators. On the left, middle and right a double, single and double-concentric hydraulic actuator is shown respectively.

The advantage of a single-rod linear actuator is that it only has one moving end. The advantage of a double-rod is that it is more stiff and therefore has better dynamic properties [39]. The double-concentric actuator combines the advantages of both but is more expensive due to complexity of the part. For the SRS a double-concentric actuator is chosen as high performance is required.
The hydraulic actuator shows nonlinear behavior due to factors such as oil compressibility which influences the actuator stiffness with position and hydrostatic bearing leakage which effect the steady state spool flow characteristics [39].

1.6. Hydraulic Gough-Stewart platform control

When an input is given to the servo-valve it will indirectly cause the hydraulic actuator to exert a force on the platform which will in turn cause a movement of this end effector. In order to give the right inputs to the six valves present in the SRS a controller is needed that calculates the required input to follow the provided reference trajectory to the simulator. Due to the many nonlinearities present in the electro-hydraulic servo-valves, hydraulic actuators and Gough-Stewart platform and the requirement for high control performance a controller is needed that can accurately control this highly nonlinear system. It would be desirable to have little difference between the reference trajectory given to the controller and the realized trajectory. Several of such controllers have been designed in the past of which a fairly new controller based on Incremental Nonlinear Dynamic Inversion (INDI) has shown promising results [16]. This INDI controller will therefore be used in this thesis.

1.7. Servo-valve saturations

An input to the magnetic torque motor causes the flapper to move. The bigger the input to the motor the larger the deflection. At a certain moment the deflection will however not increase anymore by increasing the input further as it will have reached its maximum position. Increasing the input to the valve will therefore not have any direct additional effect on the output of the servo-valve. At this point the servo-valve is therefore said to have saturated. A visual representation of such a saturation case is shown in figure 6.3

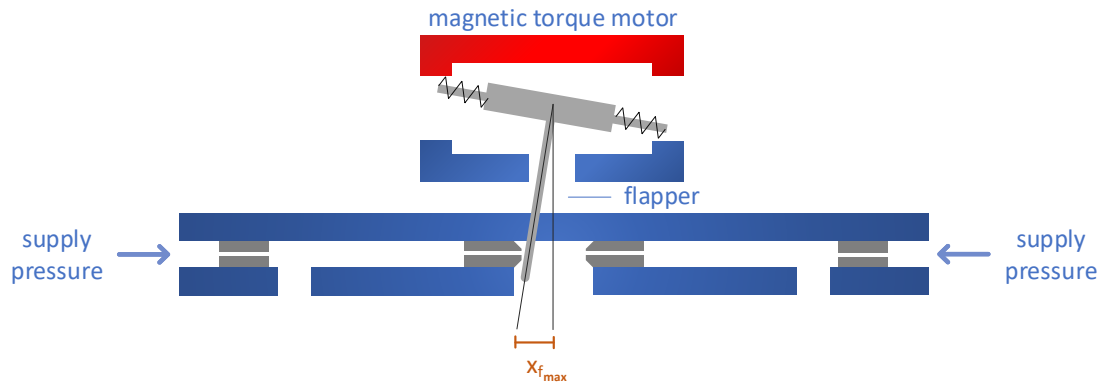

Figure 1.6: The maximum deflection of the flapper in the electro-hydraulic servo-valve presented in a schematic representation

At this moment it is unknown whether such servo-valve saturations occur for the SRS during nominal operation and what effect it has on the INDI controller. It is therefore of interest to investigate the presence and effect of such saturations in order to deal with the effects if necessary.

1.8. Oscillations

G. Schothorst has found that for the SRS the interaction between the dynamics of the transmission lines and servo-valve can cause the system to become unstable and start to oscillate at the natural frequency of the transmission lines at around 200 Hz [39]. S.H. Koekebakker then designed filters for the ΔP controller to

prevent the system from getting into this resonance mode [22]. Y. Huang has also found that his INDI controller encountered this problem without the proper filters [16]. The setup of the SRS has however changed and therefore the presence of this resonation should be re-evaluated as the adaptations such as new sensors might have influence this effect. It is also found that the INDI controller has undesirable oscillations in the low-frequency region which should also be investigated.

1.9. Problem Statement

A new INDI controller has been designed for the SIMONA Research Simulator. At this moment it is unknown what the effects of servo-valve saturations on this controller are and if they should be mitigated. Besides this, undesirable frequencies in both the low- and high-frequency region are present.

1.10. Research Questions

- Does the control performance of the INDI controller for the SIMONA Research Simulator increase by taking saturations of the electro-hydraulic servo-valve into account?
  - Do servo-valve saturations occur during nominal operation?
  - What are the effects of servo-valve saturations on the controller?
  - Is it possible to mitigate the negative effects due to servo-valve saturations?
- Can the undesirable oscillations present in the low- and high-frequency region of the INDI controller for the SIMONA Research Simulator be eliminated?
  - What is the reason for these oscillations?
  - Is it possible to eliminate or reduce these undesirable frequencies?
- How does the INDI controller for the SIMONA Research Simulator behave when a model is used to determine the main spool position of the electro-hydraulic servo-valve instead of measurements?

2

Modelling of the SRS

A model of the flight simulator can provide much insight in the dynamic behavior of the flight simulator. Such a model can also be used in simulation to design a controller and test its performance. For the SRS the modelling can be differentiated twofold, that is the modelling of an individual hydraulic leg and modelling of the Stewart platform driven by the six legs.

2.1. Modelling the servo-system

In 1997 during the development of the SRS, research has been performed on modelling long-stroke hydraulic servo-systems by G. Schothorst. [39] In his research he has accurately modeled the hydraulic servo-system for the SRS. He modeled the servo-valve, hydraulic actuator, and transmission line dynamics and validated his models on the SRS. His work will serve as the foundation for modelling the hydraulic servo-system in this thesis. Figure 2.1 gives a global overview of the components of the hydraulic servo-system as depicted by Schothorst and how they interact with each other.

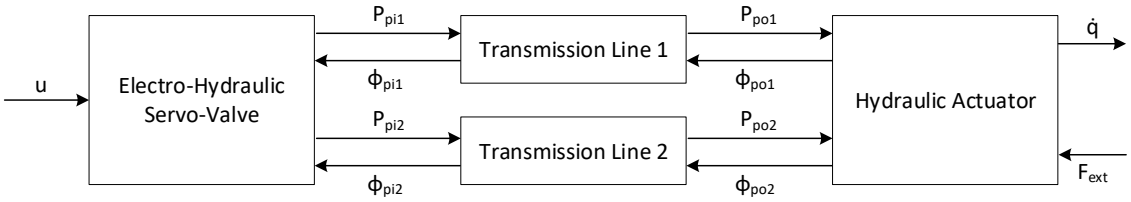

Figure 2.1: Interactions between the components of the hydraulic servo system

The following sections serve as a rehearsal for the modeling work done by Schothorst regarding the hydraulic servo-system and treat each of the components as indicated by figure 2.1. For a more detailed explanation of each of the components the reader is referred to the work by Schothorst. [39] Some adaptations have been made to the model as well by Y. Huang [17]

2.1.1. Electro-hydraulic servo-valve

The SRS makes use of a three-stage electro-hydraulic servo-valve to control the pressure in the hydraulic actuator. The three-stage valve consists of a typical two-stage valve which is used to drive a third stage. An electro-magnetic torque motor is used to move an armature which is rigidly connected to the flapper. This flapper in turn moves closer to either one of the nozzles, allowing the flow to decrease through this nozzle and increase for the other nozzle. The difference in flows through the nozzles in turn generates a pressure difference on the spool, which will start to move accordingly. The flapper is also connected mechanically to the second-stage spool resulting in a mechanical feedback link between the spool and flapper position. A schematic representation of the second-stage valve is presented in figure 1.4. In this figure i_{ca} indicates the

input current to the torque motor, P_s is the supply pressure, x_f is the flapper deflection at the nozzles, x_s is the second-stage spool position, and P_{m1} and P_{m2} are the second-stage output pressures.

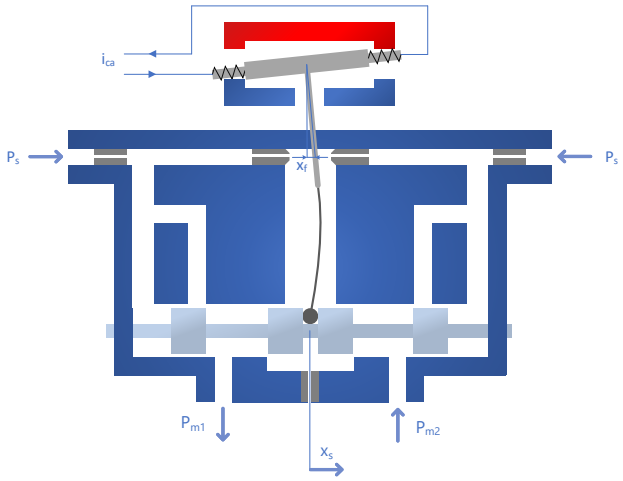

Figure 2.2: Schematic representation of the hydraulic servo-valve components and interactions

For the SRS a three-stage servo-valve is used which means that the two-stage servo-valve is extended by another stage which adds another power amplification to the system. The last stage has another spool which is referred to as the main spool which is driven by the hydraulic outlets of the previous stage. The movement of the main spool will change the outlet pressures of the third stage to the transmission lines which can be used to drive a hydraulic actuator. The third stage is presented schematically in figure 2.3. In this figure the main spool position is indicated by x_m, and P_{p1} and P_{p2} are the output pressures of the third stage.

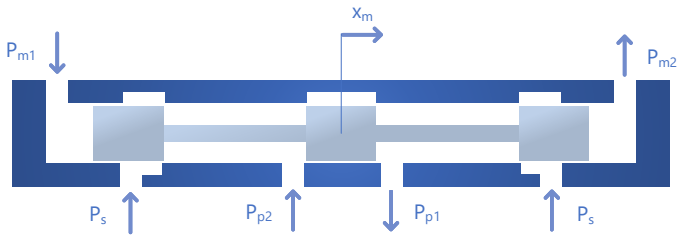

Figure 2.3: The third stage of the electro-hydraulic servo-valve presented in a schematic fashion

In order to obtain an accurate model of the servo valve an analytical model as proposed by Schothorst is used. The overview of the model components and interactions is shown in figure 2.4 In this thesis the Coulomb friction on the spools will not be modeled as Schothorst found that this has a negligible effect on the valve dynamics. [39] Each of the blocks which are modeled are explained in more detail in this section by means of elaboration on the mathematical formulation of each component.

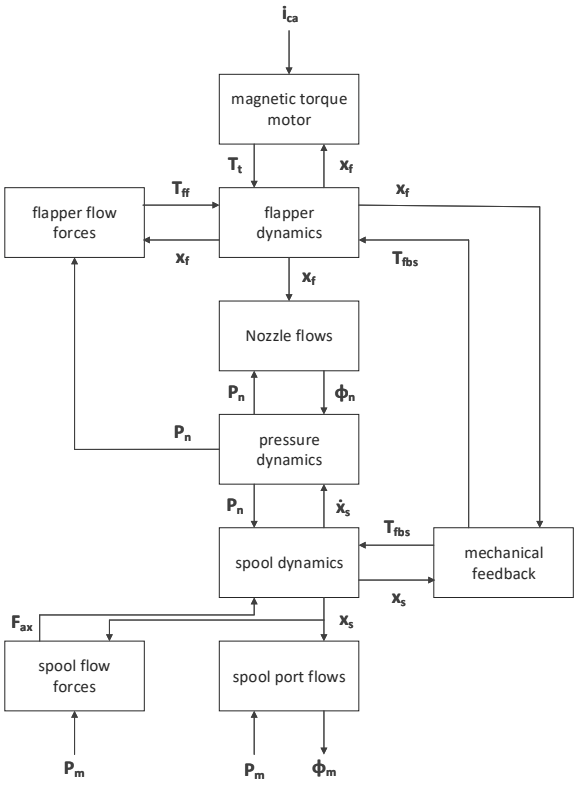

Figure 2.4: An overview of the components and interactions for the two-stage servo-valve model [39]

Non-linear torque motor

The servo-valve is controlling the flow through positioning the flapper closer to either one of the nozzles. The flapper is driven by an electro-magnetic torque motor that allows for positioning the flapper closer to either side. The current to the torque motor is linearly related to the control input as shown by equation 2.1. In this equation i_{ca} is the input current to the motor, K_{ca} is the current amplifier gain, and u is the control input.

$$i_{ca} = K_{ca} u \tag{2.1}$$

The current caused by an input will in turn cause the electro-magnetic motor to generate a torque. The relation between the input current and the generated torque by the motor T_t can be described by equation 2.2 [28] [42], where μ_0 is the magnetic permeability of air, A_g is the gap normal in the magnetic flux direction, M_0 the magnetomotive force, N the number of windings of the coil, l_a it the armature length, x_g is the flapper deflection distance at the tip, and g the gap distance of the armature in neutral position.

$$T_t = \frac{\mu_0 A_g l_a}{4} \left[\left(\frac{M_0 + i_{ca} N}{g - x_g} \right)^2 - \left(\frac{M_0 - i_{ca} N}{g + x_g} \right)^2 \right] \tag{2.2}$$

The relation of the flapper deflection distance at the tips and at the nozzles is given by equation 2.3, which follows from simple geometric algebra. In this equation l_f the flapper length.

$$x_g = \frac{l_a}{l_f} x_f \tag{2.3}$$

It can can however be assumed that the torque is linearly dependent on the input current when the rotations are assumed to be small for the servo-valve. [28] The linearized relation between the torque generated by the motor and the input current is given by equation 2.4. [39] This equation will be used in simulation instead of 2.2. In this equation K_t is the torque motor gain and K_b is the torque motor magnetic stiffness.

$$T_{t,lin} = K_t i_{ca} + K_b x_f \tag{2.4}$$

Flapper dynamics
The torque generated by the motor will drive the flapper, which is also influenced by other external torques due to viscous friction, bending of the flapper, flow forces, and the mechanical feedback mechanism. The relation between these influences and the flapper position is given by equation 2.5. [4] In this equation J_a represents the inertia of the flapper, B_a the viscous friction coefficient of the flapper, K_a the equivalent flapper spring constant, T_{ff} the torque due to the nonlinear flow forces, T_{fbs} the torque due to the mechanical feedback mechanism.

$$\frac{J_a}{l_f}\ddot{x}_f = T_t - B_a\dot{x}_f - K_a x_f + T_{ff} - T_{fbs} \tag{2.5}$$

Non-linear nozzle flows
The flows through the nozzles will also influence the pressure dynamics, which in turn influences the flow forces on the flapper. It is therefore of interest to take this effect into account. According to Schothorst the nozzle flows ϕ_{n1} and ϕ_{n2} can be modeled using equations 2.6 and 2.7 [39]. In these equations C_d is the discharge coefficient, D_n the nozzle diameter, x_{f0} the distance between the flapper and nozzle in neutral position, ρ the density of the hydraulic fluid, C_d is the discharge coefficient, $P_{ni}, i = 1,2$ the nozzle pressures, and P_{n3} the nozzle outlet pressure.

$$\phi_{n1} = C_d \pi D_n (x_{f0} + x_f)\sqrt{2\frac{P_{n1} - P_{n3}}{\rho}} \tag{2.6}$$

$$\phi_{n2} = C_d \pi D_n (x_{f0} - x_f)\sqrt{2\frac{P_{n2} - P_{n3}}{\rho}} \tag{2.7}$$

Non-linear flow forces on flapper
The flows through the nozzles together with the pressure dynamics exert forces on the flapper resulting in a corresponding torque. According to Schothorst [39] the torque on the flapper due to the non-linear flow forces can be modeled by equation 2.8.

$$T_{ff} = \frac{\pi}{4} D_n^2 l_f \left(\left[1 + \frac{16C_d^2}{D_n^2}(x_{f0}^2 + x_f^2) \right] (P_{n1} - P_{n2}) + \left[\frac{16C_d^2}{D_n^2} 2 x_{f0} x_f \right] (P_{n1} + P_{n2} - 2P_{n3}) \right) \tag{2.8}$$

Pressure dynamics
The flapper-nozzle system will control the second stage by means of changing the flows through the nozzles through displacing the flapper. The dynamics of the pressure in the second stage that the flapper-nozzle system is controlling can be described using equations 2.9 and 2.10 which follow from the mass balances of the valve chambers. [25] In these equations ϕ_{01} and ϕ_{02} are the flows through the inlet restrictions, E is the oil bulk modulus, A_s the spool side area, A_{n3} the orifice area.

$$\dot{P}_{n1} = \frac{E}{V_{n1}}(\phi_{01} - \phi_{n1} + A_s\dot{x}_s) \tag{2.9}$$

$$\dot{P}_{n2} = \frac{E}{V_{n2}}(\phi_{02} - \phi_{n2} - A_s\dot{x}_s) \tag{2.10}$$

$$\dot{P}_{n3} = \frac{E}{V_{n3}}\left(\phi_{n1} + \phi_{n2} - C_d A_{n3}\sqrt{2\frac{P_{n3} - P_t}{\rho}} \right) \tag{2.11}$$

The flows through the inlet restrictions can be described by equations 2.12 and 2.13. [39] In these equations A_0 represents the inlet restriction orifice area.

$$\phi_{01} = C_d A_0 \sqrt{2\frac{P_s - P_{n1}}{\rho}} \tag{2.12}$$

$$\phi_{02} = C_d A_0 \sqrt{2\frac{P_s - P_{n2}}{\rho}} \tag{2.13}$$

Spool dynamics
The dynamics of the spool can be described by the equation of motion of the spool as presented in equation 2.14 [25], where M_s is the mass of the spool, w_s the viscous friction coefficient, l_{fbs} the feedback spring length, F_{cs} the force due to Coulomb friction, and F_{ax} the axial flow force.

$$M_s\ddot{x}_s = A_s(P_{n2} - P_{n1}) - w_s\dot{x}_s - \frac{T_{fbs}}{l_f + l_{fbs}} - F_{cs} - F_{ax} \tag{2.14}$$

Mechanical Feedback
In order to generate a feedback link between the flapper and valve-spool position a spring like connection between the two is established. This connection will therefore create a controlling torque acting on both the spool and flapper. The effect of this feedback on the spool can be modeled using equation 2.15. In this equation K_{fbs} is the feedback spring constant.

$$T_{fbs} = K_{fbs}\left[\frac{l_f + l_{fbs}}{l_f}x_f + x_s\right] \tag{2.15}$$

If ball clearance is present equation 2.16 is used to determine whether the torque is equal to zero or calculated using equation 2.15 where c_b is the ball clearance.

$$-c_b \leq \left(\frac{l_f + l_{fbs}}{l_f}\right)x_f + x_s \leq c_b \tag{2.16}$$

Non-linear spool port flows
The flows that exit the two-stage servo-valve to the third stage are influenced by the return pressure, supply pressure, pressures from the previous stage, and the leakage flows. These flows ϕ_{m1} and ϕ_{m2} from the second stage to the third and vice-versa can be modeled using equations 2.17 and 2.18. [39] [28] [40] In this equation $\phi_{l,s1}$ and $\phi_{l,s1}$ are the second stage leakage spool port flows, and A_{s1}, A_{s2}, A_{s3} and A_{s4} are the second stage spool port opening areas.

$$\phi_{m1} = C_d A_{s1}\sqrt{2\frac{P_s - P_{m1}}{\rho}} - C_d A_{s2}\sqrt{2\frac{P_{m1} - P_t}{\rho}} + \phi_{l,s1} - \phi_{l,s2} \tag{2.17}$$

$$\phi_{m2} = C_d A_{s3}\sqrt{2\frac{P_{m2} - P_t}{\rho}} - C_d A_{s4}\sqrt{2\frac{P_s - P_{m2}}{\rho}} + \phi_{l,s3} - \phi_{l,s4} \tag{2.18}$$

The spool port opening areas are modelled using equations 2.19 and 2.20,where h_x is second stage spool port opening width, d_{si} is the port underlap for port i of the second stage, and c_{rs} is the radial clearance of the second stage spool and the bushing.

$$A_{si} = \begin{cases} h_s\sqrt{(x_s + d_{si})^2 + c_{rs}^2} & x_s \geq -d_{si} \\ 0 & x_s < -d_{si} \end{cases} \quad i = 1,3 \tag{2.19}$$

$$A_{si} = \begin{cases} h_s\sqrt{(d_{si} - x_s)^2 + c_{rs}^2} & x_s \leq d_{si} \\ 0 & x_s > d_{si} \end{cases} \quad i = 2,4 \tag{2.20}$$

In order to obtain the leakage flows the quadratic equations presented in 2.21 have to be solved. [39] These equations model both a laminar and turbulent part of the leakage flow and η represents the dynamic viscosity of oil. The axial force from the third stage on the second stage can be calculated using equation 2.22.

$$\begin{array}{lll} \frac{\rho}{2C_d h_s^2 c_{rs}^2}\phi_{l,s1}^2 - \frac{12\eta(x_s + d_{s1})}{h_s c_{rs}^3}\phi_{l,s1} & = P_s - P_{m1}, & x_s < -d_{s1} \\ \frac{\rho}{2C_d h_s^2 c_{rs}^2}\phi_{l,s2}^2 + \frac{12\eta(x_s - d_{s2})}{h_s c_{rs}^3}\phi_{l,s2} & = P_{m1} - P_t, & x_s > \ d_{s2} \\ \frac{\rho}{2C_d h_s^2 c_{rs}^2}\phi_{l,s3}^2 - \frac{12\eta(x_s + d_{s3})}{h_s c_{rs}^3}\phi_{l,s3} & = P_{m2} - P_t, & x_s < -d_{s3} \\ \frac{\rho}{2C_d h_s^2 c_{rs}^2}\phi_{l,s4}^2 + \frac{12\eta(x_s - d_{s4})}{h_s c_{rs}^3}\phi_{l,s4} & = P_s - P_{m2}, & x_s > \ d_{s4} \\ \phi_{l,si} & = 0, & x_s \geq -d_{si} \\ \phi_{l,si} & = 0, & x_s \leq \ d_{si} \end{array} \tag{2.21}$$

$$F_{ax} = 2cos(\theta)C_d[A_{s1}(P_s - P_{m1}) - A_{s2}(P_{m1} - P_t) + A_{s3}(P_{m2} - P_t) - A_{s4}(P_s - P_{m2})] \tag{2.22}$$

Third stage

The previous stage can be used to control a third stage which is also the case for the SRS. Modeling the third stage is very alike to modeling the second stage. In the third stage the pressure dynamics can be neglected due to the fact that the operating frequency of the spool is much smaller than the natural frequency. Neglecting the pressure dynamics implies that the spool dynamics are related to the other model variables as depicted by equations 2.23 and , which represent the mass and force balance in the main spool chambers respectively. [39] In these equations A_m is the main spool side area.

$$\phi_{m1} = \phi_{m2} = A_m \dot{x}_m \tag{2.23}$$

$$A_m(P_{m1} - P_{m2}) = 0 \rightarrow P_{m1} = P_{m2} \tag{2.24}$$

The spool of the third stage, which we will call the main spool from now on, is driven by the previous stage. The position of this main spool is measured electronically and fed back such that it can be used as feedback signal in the control loop. The control law used for the SRS is depicted by equation 2.25, where K_{pm} and K_{dm} are the proportional and differential feedback gains, $\bar{u}$ the normalized input signal, $\bar{x}_m$ the normalized main spool position, and $\bar{i}_{ca}$ the resulting normalized current.

$$\bar{i}_{ca} = K_{pm}(\bar{u} - (1 + K_{dm}s)\bar{x}_m) \tag{2.25}$$

The flows between the hydraulic actuator and the third stage are modeled in a similar fashion as the flows between the second and third stage and are presented by equations 2.26 and 2.27. In these equations $\phi_{l,mi}$ represents the third stage leakage flow and A_{mi} is the main spool port opening area for port i.

$$\phi_{p1} = C_d A_{m1}\sqrt{2\frac{P_s - P_{p1}}{\rho}} - C_d A_{m2}\sqrt{2\frac{P_{p1} - P_t}{\rho}} + \phi_{l,m1} - \phi_{l,m2} \tag{2.26}$$

$$\phi_{p1} = C_d A_{m3}\sqrt{2\frac{P_{p2} - P_t}{\rho}} - C_d A_{m4}\sqrt{2\frac{P_s - P_{p2}}{\rho}} + \phi_{l,m3} - \phi_{l,m4} \tag{2.27}$$

In which the main spool port opening areas are modelled using equations 2.28 and 2.29, where h_m is main spool port opening width, d_{mi} is the port underlap for port i, c_{rm} is the radial clearance of the main spool and the bushing.

$$A_{mi} = \begin{cases} h_m\sqrt{(x_m + d_{mi})^2 + c_{rm}^2} & x_m \geq -d_{mi} \\ 0 & x_m < -d_{mi} \end{cases} \quad i = 1,3 \tag{2.28}$$

$$A_{mi} = \begin{cases} h_m\sqrt{(d_{mi} - x_m)^2 + c_{rm}^2} & x_m \leq d_{mi} \\ 0 & x_m > d_{mi} \end{cases} \quad i = 2,4 \tag{2.29}$$

The leakage flows in the third stage are modeled similarly to the approach for the second stage. The equations used to determine the leakage flows are given by the equations in 2.30.

$$\begin{array}{lll} \frac{\rho}{2C_d h_m^2 c_{rm}^2}\phi_{l,m1}^2 - \frac{12\eta(x_m + d_{m1})}{h_m c_{rm}^3}\phi_{l,m1} & = P_s - P_{p1}, & x_m < -d_{m1} \\ \frac{\rho}{2C_d h_m^2 c_{rm}^2}\phi_{l,m2}^2 + \frac{12\eta(x_m - d_{m2})}{h_m c_{rm}^3}\phi_{l,m2} & = P_{p1} - P_t, & x_m > d_{m2} \\ \frac{\rho}{2C_d h_m^2 c_{rm}^2}\phi_{l,m3}^2 - \frac{12\eta(x_m + d_{m3})}{h_m c_{rm}^3}\phi_{l,m3} & = P_{p2} - P_t, & x_m < -d_{m3} \\ \frac{\rho}{2C_d h_m^2 c_{rm}^2}\phi_{l,m4}^2 + \frac{12\eta(x_m - d_{m4})}{h_m c_{rm}^3}\phi_{l,m4} & = P_s - P_{p2}, & x_m > d_{m4} \\ \phi_{l,mi} & = 0, & x_m \geq -d_{mi} \\ \phi_{l,mi} & = 0, & x_m \leq d_{mi} \end{array} \tag{2.30}$$

2.1.2. Simulation of the servo-valve models

Schothorst also performed system identification from which he obtained the coefficients for a simplified and reduced fourth order three-stage model. For a more detailed explanation of this the reader is referred to his work. [39] The model for the first two stages is presented by the equations in 2.31 and corresponding coefficient values given by tabular 2.1.

$$\begin{bmatrix} \dddot{\tilde{x}}_f \\ \ddot{\tilde{x}}_f \\ \ddot{\tilde{x}}_s \\ \Delta\ddot{P}_n \end{bmatrix} = \begin{bmatrix} -c_1 & -c_2 & c_3 & c_4 \\ 1 & 0 & 0 & 0 \\ 0 & 1 & -c_5 & c_6 \\ 0 & -c_7 & 1 & -c_8 \end{bmatrix} \begin{bmatrix} \dot{\tilde{x}}_f \\ \tilde{x}_f \\ \tilde{x}_s \\ \Delta P_n \end{bmatrix} + \begin{bmatrix} -c_9 \\ 0 \\ 0 \\ 0 \end{bmatrix} i_{ca} \tag{2.31}$$

c_1	4.29e3	c_6	1.00e4
c_2	2.96e7	c_7	9.93e-1
c_3	2.30e10	c_8	4.40e3
c_4	1.13e11	c_9	2.68e10
c_5	1.00e2	c_{10}	1.27e2
K_{pm}	8.00	K_{dm}	4.90e-4

Table 2.1: Identified coefficient values for the reduced flapper nozzle model as identified by Schothorst [39]

Besides the coefficients for the first two stages, Schothorst also identified the coefficient to model the interaction between the flapper-nozzle and the third stage. The structure used by Schothorst for identification is given by figure 2.5. In this figure f_1 represents the function for the nonlinearities present in the system, c_{10} is an identified coefficient, ,$\bar{x}_s$ is the normalized second-stage spool position and $\bar{\phi}_m$ is the normalized flow to the main spool stage.

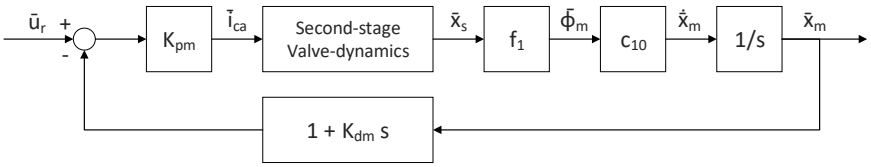

Figure 2.5: The structure used for the identification of the flapper-nozzle model and third stage parameters [39]

In order to simulate the analytical model values are needed for the parameters used by the model. Schothorst has determined and identified these parameters for the servo-valve of the SRS [39], which are presented in table 2.2 for convenience.
The responses of both the analytical model as well as the identified fourth order model to a step response of 0.1 are shown in figure 2.6. As can be observed there is a difference between both models and according to Schothorst the identified model is also the model that most accurately represents the servo-valve. Both models are used to check stability, but the identified model will be used as the main model for the simulations.

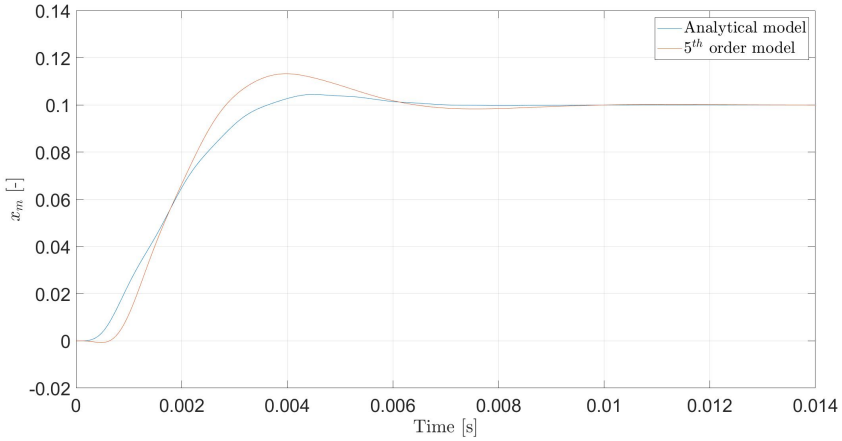

Figure 2.6: Responses of the analytical and 5^{th} order model to an step input of 0.1 at t=0

c_{rm}	=	$1.60\ 10^{-6}$	$[m]$	B_a	=	$2.50\ 10^{-2}$	$[N\,m\,s/m]$
c_{rs}	=	$1.95\ 10^{-6}$	$[m]$	C_d	=	0.60	$[-]$
d_{m1}	=	$8.00\ 10^{-6}$	$[m]$	D_n	=	$6.00\ 10^{-4}$	$[m]$
d_{m2}	=	$8.00\ 10^{-6}$	$[m]$	E	=	$1.00\ 10^{9}$	$[N/m^2]$
d_{m3}	=	$8.00\ 10^{-6}$	$[m]$	J_a	=	$1.00\ 10^{-7}$	$[kg\,m^2]$
d_{m4}	=	$8.00\ 10^{-6}$	$[m]$	K_a	=	$3.34\ 10^{3}$	$[N\,m/m]$
d_{s1}	=	$3.90\ 10^{-6}$	$[m]$	K_b	=	$3.26\ 10^{3}$	$[N\,m/m]$
d_{s2}	=	$3.90\ 10^{-6}$	$[m]$	K_{fbs}	=	120	$[N\,m/m]$
d_{s3}	=	$3.90\ 10^{-6}$	$[m]$	K_t	=	0.783	$[N\,m/m]$
d_{s4}	=	$3.90\ 10^{-6}$	$[m]$	K_{ca}	=	$6.00\ 10^{-3}$	$[A/V]$
g	=	$4.00\ 10^{-4}$	$[m]$	K_{ms}	=	$6.25\ 10^{-3}$	$[V/m]$
h_m	=	$4.00\ 10^{-2}$	$[m]$	K_{pm}	=	2.50	$[-]$
h_s	=	$4.00\ 10^{-3}$	$[m]$	M_0	=	$1.00\ 10^{3}$	$[A]$
l_a	=	$1.00\ 10^{-2}$	$[m]$	M_s	=	$1.40\ 10^{-2}$	$[kg]$
l_f	=	$1.00\ 10^{-2}$	$[m]$	N	=	600	$[-]$
l_{fbs}	=	$2.00\ 10^{-2}$	$[m]$	P_s	=	$1.40\ 10^{7}$	$[N/m^2]$
w_s	=	20	$[m]$	P_t	=	0.00	$[N/m^2]$
x_{f0}	=	$6.29\ 10^{-5}$	$[N\,s/m]$	V_{n1}	=	$4.10\ 10^{-7}$	$[m^3]$
A_0	=	$1.26\ 10^{-7}$	$[m^2]$	V_{n2}	=	$4.10\ 10^{-7}$	$[m^3]$
A_g	=	$1.66\ 10^{-5}$	$[m^2]$	V_{n3}	=	$2.50\ 10^{-7}$	$[m^3]$
A_m	=	$3.14\ 10^{-2}$	$[m^2]$	η	=	$2.50\ 10^{-7}$	$[kg/m\,s]$
A_{n3}	=	$4.10\ 10^{-7}$	$[m^2]$	μ_0	=	$4\pi\ 10^{-7}$	$[V\,s/A\,m]$
A_s	=	$4.95\ 10^{-5}$	$[m^2]$	ρ	=	850	$[kg/m^3]$

Table 2.2: Parameters used for the simulation of the electro-hydraulic servo-valve of the SRS as identified by Schothorst [39]

2.1.3. Transmission lines

Huang [16] has modelled the transmission lines for the SRS, who adopted the approaches as first proposed by Yang et al. [43] Huang found that only the first resonance mode around 200 Hz was relevant for the SRS and therefore modelled the transmission lines as two-second order systems. The second order system to be used for simulation is presented in equation 2.32 with dissipation number $D_n t$ line impedance constant Z_0 and undamped natural frequencies of node i λ_{ci} given by equations 2.33, 2.34 and 2.35 respectively. In the model L is the line length, r_h is the cross-section radius, A_0 is the cross-section area, ν_{kin} is the kinematic viscosity, ρ_0 is the oil density, and c_0 is the speed of sound in oil. The implementation of the model by Huang [16] will be used in simulation.

$$\begin{bmatrix} \dot{P}_{pi} \\ \dot{\phi}_{po} \end{bmatrix} = \begin{bmatrix} 0 & -(-1)^{i+1} Z_0 \lambda_{c_i} \\ -\frac{(-1)^{i+1}\lambda_{c_i}}{Z_0 \alpha^2} & -\frac{8\beta}{\alpha} \end{bmatrix} \begin{bmatrix} P_{pi,i} \\ \phi_{po,i} \end{bmatrix} + \begin{bmatrix} 0 & -\frac{2Z_0}{D_n t} \\ \frac{2}{Z_0 D_n t \alpha^2} & 0 \end{bmatrix} \begin{bmatrix} P_{po} \\ \phi_{pi} \end{bmatrix} \tag{2.32}$$

$$D_n t = \frac{L \nu_{kin}}{c_0 r_h^2} \tag{2.33}$$

$$Z_0 = \frac{\rho c_0}{A_0} \tag{2.34}$$

$$\lambda_{ci} = \frac{\pi(i-0.5)}{D_n t} \tag{2.35}$$

The values used for the simulation of the transmission lines for the SRS as found by Huang are presented in table 2.3. The first eigenmode is relevant according to the analysis by Huang and therefore i=1 is chosen for the simulations.

L	=	$1.60\ 10^{-6}$	$[m]$	ρ_0	=	$2.50\ 10^{-2}$	$[kg/m^3]$
r_h	=	$1.95\ 10^{-6}$	$[m]$	c_0	=	0.60	$[-]$
A_0	=	$8.00\ 10^{-6}$	$[m^2]$	i	=	1	[-]
ν_{kin}	=	$8.00\ 10^{-6}$	$[m^2/s]$				

Table 2.3: Parameters to be used for simulations of the SRS transmission lines

2.1.4. Hydraulic actuator

The servo-valve is driving the hydraulic actuator which is presented schematically by figure 2.7, where q is the leg extension from the neutral position, ϕ_{p1} and ϕ_{p2} are the flows from the transmission lines to the hydraulic actuator, ϕ_{l1} and ϕ_{l2} are the leakage flows for the first and second chamber respectively, V_1 and V_2 are the volumes in the first and second chamber, P_1 and P_2 are first and second actuator chamber pressures, and A_p the piston area. This figure is not an accurate representation of a double-concentric hydraulic actuator, but serves as clarification.

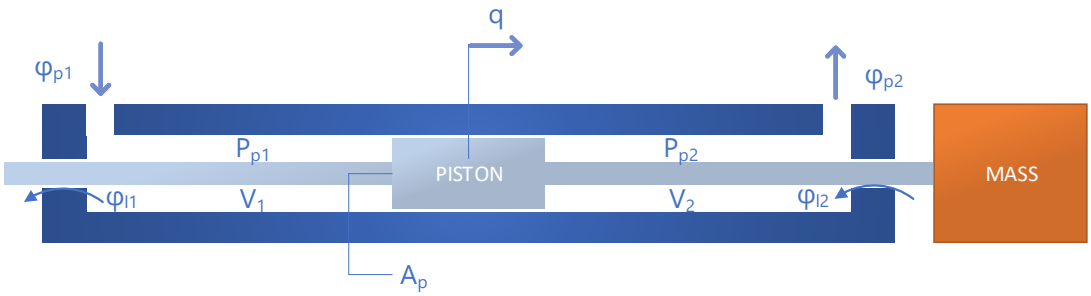

Figure 2.7: A hydraulic actuator representation attached to a mass M

According to Schothorst [39] the pressure dynamics of the chambers can be described by equations 2.36 and 2.37, where the velocity of the piston $\dot{q}$ follows from the dynamics of the system and the chamber flows ϕ_{p1} and ϕ_{p2} follow from the interaction of the system with the servo-valve and transmission lines.

$$\dot{P}_{p1} = \frac{E}{V_m + A_p q}(\phi_{o1} - \phi_{l1} - A_p \dot{q}) \tag{2.36}$$

$$\dot{P}_{p2} = \frac{E}{V_m - A_p q}(\phi_{l2} - \phi_{o2} + A_p \dot{q}) \tag{2.37}$$

According to Schothorst the leakage flows ϕ_{l1} and ϕ_{l2} can be calculated using equations 2.38 and 2.39 for a double-concentric hydraulic actuator.

$$\phi_{l1} = \phi_{l,b4} \tag{2.38}$$

$$\phi_{l1} = -\phi_{l,b2} + \phi_{l,b3} \tag{2.39}$$

In these equations $\phi_{l,bi}$ represents the leakage flow for bearing i. The Leakages for each bearing can be calculated using equations 2.40, 2.41, 2.42 and 2.43, where LP_{bi} represents the leakage parameter for bearing i that has been identified by Schothorst. [39]

$$\phi_{l,b1} = LP_{b1}(P_s - P_t) + A_{p,b1}\dot{q} \tag{2.40}$$

$$\phi_{l,b2} = LP_{b2}(P_s - P_{p2}]) - A_{p,b2}\dot{q} \tag{2.41}$$

$$\phi_{l,b3} = LP_{b3}(P_{p2} - P_t) + A_{p,b3}\dot{q} \tag{2.42}$$

$$\phi_{l,b4} = LP_{b4}(P_{p1} - P_t) - A_{p,b4}\dot{q} \tag{2.43}$$

2.1.5. Simplified hydraulic actuator model

The aforementioned equations together will be used to model the hydraulic actuator in simulation. When some additional assumptions are made and a change of coordinates is applied a simpler model can also be obtained. The small term due to the flow derivatives is dropped as well as the term including the oil stiffness derivative which is assumed to be zero at the mid position and can therefore be dropped after the change of coordinates. The simplified mathematical representation can be observed in equation 2.44. For a more detailed derivation the reader is referred to the work by Koekebakker. [22] The new equation provides a more simplified model of the actuator, but is far more compact and suitable for control purposes.

$$\dot{P}_L = 2C_m(q)(\phi_n\sqrt{1 \pm P_L/P_s}u - L_{lm}P_L - A_p\dot{q}) \tag{2.44}$$

In this simplified equation $\dot{P}_L$ is the actuator pressure difference that is equal to the difference between the first and second actuator chamber pressures such that $\dot{P}_L = \dot{P}_{p1} - \dot{P}_{p2}$, L_{lm} is the main leakage parameter, ϕ_n is the maximum valve flow, and C_m the position dependent oil stiffness to be calculated using equation 2.45, where V_m is the volume of the chamber when the actuator is in the middle position.

$$C_m = \frac{1}{2}\left(\frac{E}{V_m + A_p q} + \frac{E}{V_m - A_p q}\right) \tag{2.45}$$

2.1.6. Simulation of the hydraulic actuator models

To exemplify that there are some differences between the simplified and full model of the hydraulic actuator a simulation is executed where a sinusoidal input to the hydraulic actuator model is given for both models. For the simulation a mass of 1500 kg is attached to the actuator and gravity is neglected. The results of the simulation can be found in figure 2.8. The parameters that were used for the full and simplified hydraulic actuator models for the simulations can be found in tables 2.4, 2.5 and 2.6 respectively.

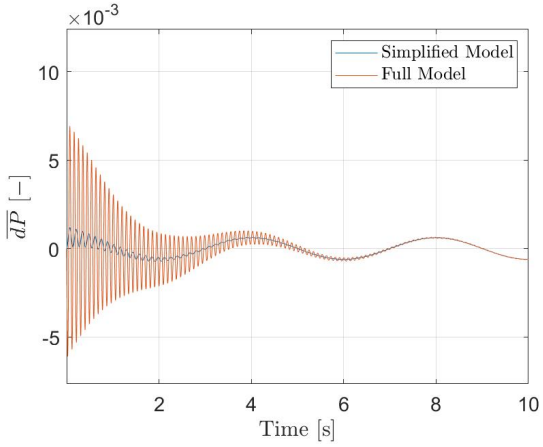

(a) The pressure output of the hydraulic actuator models

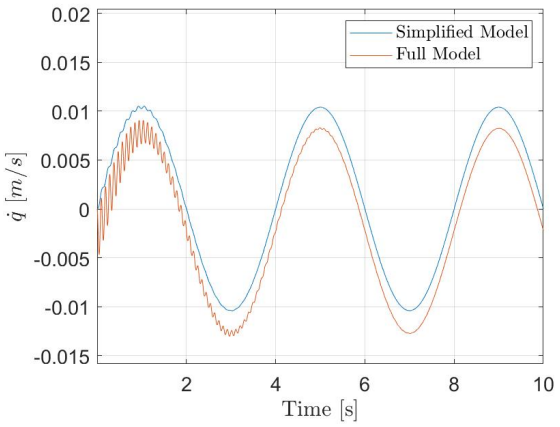

(b) The pressure output of the hydraulic actuator models

Figure 2.8: Responses of the hydraulic actuator models to a sinusoidal input with a frequency of 0.25 Hz and an amplitude of 0.01

Symbol	Value
LP_{b1}	7.80E-13
LP_{b2}	7.80E-13
LP_{b3}	8.00E-13
LP_{b4}	1.35E-12

Table 2.4: Leakage parameters for bearing 1-4

Symbol	Value
$A_{p,b1}$	5.00E-6
$A_{p,b2}$	5.00E-6
$A_{p,b3}$	6.30E-6
$A_{p,b4}$	3.80E-6

Table 2.5: Virtual piston areas for bearing 1-4

Symbol	Description	Value
ϕ_n	maximum valve flow	2.6E-3
L_{lm}	main leakage parameter	3.8187E-12
A_p	piston area	2.5E-3
P_s	supply pressure	1.6E7
P_t	return pressure	0
E	oil stiffness	1E9
V_m	actuator volume at middle position	1.9725E-3

Table 2.6: Parameters used for the hydraulic actuator models

From both models it can be seen that the hydraulic actuator is indeed a velocity generator as the sinusoidal input to the actuator results in a sinusoidal output in the velocity of equal phase and a magnitude that lies in the same order of magnitude. The simplified hydraulic model does however create a different response which should be taken into account. For this reason the full model will be used for simulation purposes and the simplified model only for control.

2.2. Modelling the Stewart platform

The dynamics of the Stewart platform are modeled as a platform that can be moved by means of six linear actuators. Y. Huang has applied the Newton-Euler approach to obtain the closed form equations for the platform of the SRS. [17] Huang has chosen this approach as it allows for calculating forward as well as backward dynamics which will be needed for the modeling the platform as well as controlling it. His model will also be used for simulation of the dynamics and control of the Stewart-platform of the SRS and is recapitulated below.

In order to define the position, speed and acceleration of the platform two reference frames are used of which the first is the body frame E_a which in this case is attached to the moving platform and secondly the inertial frame E_b of which the origin lies at the static base. The position of the platform and the velocity of the platform are defined by $\mathbf{z} = [\mathbf{c}^T, \boldsymbol{\phi}^T]^T$ and $\dot{\boldsymbol{s}} = [\dot{\mathbf{c}}^T, \boldsymbol{\omega}_p^T]^T$ respectively, with $\boldsymbol{\omega_p}$ the angular velocity of the moving platform. The derived dynamic equations for the SRS platform are given by 2.46. [8]

$$\mathbf{M(z)}\,\ddot{\boldsymbol{s}} + \boldsymbol{\beta}(\dot{\boldsymbol{x}}, \boldsymbol{z}) = \mathbf{HF} \tag{2.46}$$

where $\boldsymbol{M}$ and $\boldsymbol{\eta}$ are given by equations 2.47 and 2.48 respectively.

$$\mathbf{M} = \begin{bmatrix} M\mathbf{E}_3 & -M\mathbf{R} \\ M\mathbf{R} & \mathbf{I}_p + M(R^2\boldsymbol{E}_3 - \boldsymbol{R}\boldsymbol{R}^{\boldsymbol{T}}) \end{bmatrix} + \sum_{n=1}^{6} \begin{bmatrix} \mathbf{Q}_i & -\mathbf{Q}_i\widetilde{\boldsymbol{q}}_i \\ \widetilde{\boldsymbol{q}}_i\mathbf{Q}_i & -\widetilde{\boldsymbol{q}}_i\mathbf{Q}_i\widetilde{\boldsymbol{q}}_i \end{bmatrix} \tag{2.47}$$

$$\boldsymbol{\beta} = \begin{bmatrix} M\{\boldsymbol{\omega}_p \times (\boldsymbol{\omega}_p \times \boldsymbol{R}) - \mathbf{g}\} \\ \boldsymbol{\omega}_p \times \mathbf{I}_p + MR \times \{(\boldsymbol{\omega}_p \cdot \boldsymbol{R})\,\boldsymbol{\omega}_p - \mathbf{g}\} \end{bmatrix} + \sum_{n=1}^{6} \begin{bmatrix} \boldsymbol{V}_i \\ \boldsymbol{q}_i x \boldsymbol{V}_i \end{bmatrix} \tag{2.48}$$

In these equations $\boldsymbol{Q}$ and $\boldsymbol{V}$ contain inertial and dynamic properties for the specific system in matrix format. The vector containing the six actuator forces is given by $\boldsymbol{F}$ and is shown in equation 2.49. $\boldsymbol{H}$ is the vector containing the column input-output transformations, which is presented in equation 2.50

$$\mathbf{F} = \begin{bmatrix} F1 & F2 & F3 & F4 & F5 & F6 \end{bmatrix} \tag{2.49}$$

$$\mathbf{H} = \begin{bmatrix} \mathbf{l}_i^T & (\mathbf{q} \times \mathbf{l}_i)^T \end{bmatrix}^T \tag{2.50}$$

The above equations can be used to represent the dynamics for the SRS, which are needed for both the simulation as well as the control of the system. This preliminary thesis focuses mainly on the inner loop control and therefore the reader is referred to other works for a more complete explanation and derivation of these closed form equations of motion for the Stewart platform. [8] [17]

3

General control strategy

When an input is given to the electro-hydraulic servo-valve it will move the flapper in the servo-valve resulting in a change in the flow, the resulting flow will in turn generate a pressure difference across the hydraulic actuator. The pressure difference across the hydraulic actuator will then cause a force on the platform. Each of the six hydraulic legs can be given an input and in turn exert a force on the platform allowing it to move. In order to control these inputs to let the platform follow a desired trajectory a control algorithm is needed that tries to minimize the error between the desired trajectory, called the reference, and the measured trajectory. The reference trajectory to be tracked will contain the position, velocity, and acceleration at each time instance. Using inverse kinematics the trajectory can be converted to actuator extensions and velocities of each of the legs. The dynamics present in the SRS are highly nonlinear due to the dynamics of both the Stewart platform and the hydraulic servo-systems and therefore a controller is needed that can handle these nonlinearities whilst tracking the desired actuator extensions and velocities. Several control algorithms exist with the goal of minimizing the control error, while being able to handle these nonlinearities. This chapter will treat some of these algorithms and give a more detailed elaboration on the control strategy used for the SRS.

3.1. Position servo control

In hydraulic control three common tracking tasks can be identified which are position, velocity and force control. For the SRS the tracking task is of the positioning type as the goal is to accurately position the platform at each time instance. In position servo control the extension of each leg is measured and compared to the desired extension so that a corresponding error can be obtained which is then used by the controller to determine the input to be sent to the servo-valve. In this type of control it is often assumed that the dynamics are slow such that transient terms can be neglected. Due to the dynamics of the resulting transient system it can therefore be controlled with a controller with proportional and integral action. [27]

When pressure measurements are available it is beneficial to use the pressure difference as feedback for the controller as well for damping purposes. [40] If a feedforward term of the pressure is also available it can be used together with the pressure measurement signal in the pressure feedback loop to obtain better input-output performance especially in the high-frequency region. [39] The block diagram of such a system is schematically presented in figure 3.1, where q_d and q_d are the desired and measured actuator extension, u_r is the reference input to the servo-valve of the hydraulic actuator, and P_{ff} and P_L are the feedforward and measured pressure difference.

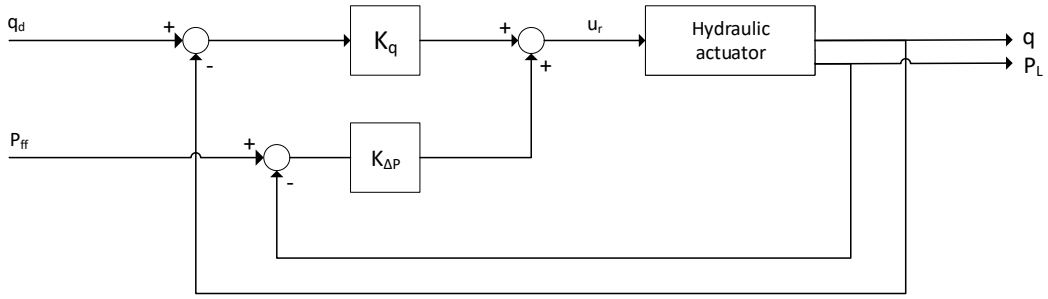

Figure 3.1: Block diagram of a position servo controller with pressure difference feedback and feedforward compensation

Schothorst did however identify some limitations of such a control strategy which is that the bandwidth of such a controller is limited to the natural frequency of the open loop system if no pressure difference feedback is used. A feedforward pressure difference term is also needed to improve the performance in the high-frequency region, but it severely degrades the performance in the low-frequency region. This degradation is due to the introduction of a pair of complex zeros that vary with the loading conditions. [39] Therefore, for a position servo controller trade-offs need to be made.

3.2. State feedback control

A way to reduce the amount of sensitivity of the controller to loading conditions is by means of full state feedback such that the poles of the closed loop system can be placed at desirable locations. Full state feedback can be achieved by adding velocity feedback to the position servo controller. Therefore the desired pressure q_d and measured pressure q_m are added to the controller such that the error between them can also be fed back. With the inclusion of this feedback damping of the complex pairs is achieved and the low-frequency performance is not severely degraded anymore by adding pressure difference feed forward compensation [39]. A schematic representation of the full state feedback controller is given by figure 3.2.

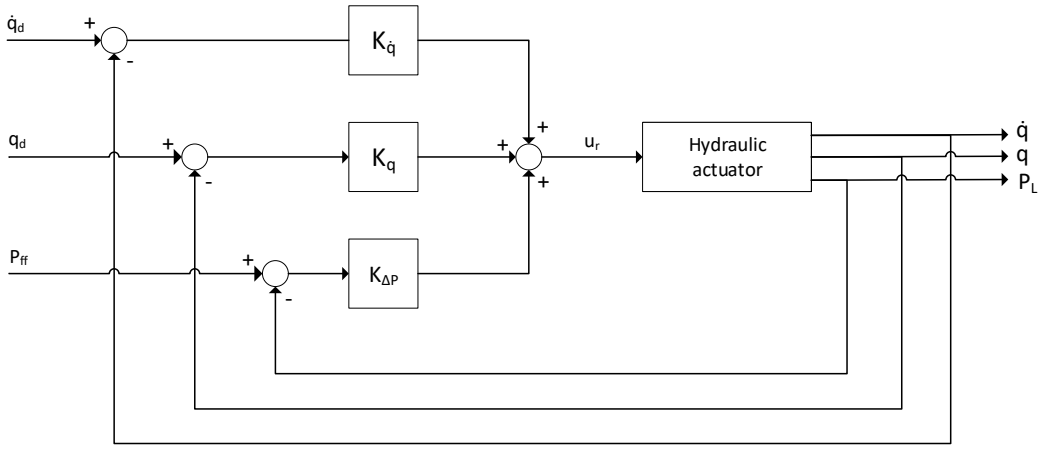

Figure 3.2: Block diagram of a full state feedback controller with pressure difference feedback and feedforward compensation

Even though this controller shows increased performance when compared to the position servo controller it still has some downsides that should be mentioned. One of which is that the frequency response has been

improved, but the bandwidth of the controller is still limited. The load dependence of the closed loop system in terms of pole locations has not yet been eliminated and therefore the performance of the controller still varies with the loading conditions. [39]

3.3. Cascade ΔP Control

In order to completely remove the load dependence of the controller a different control structure can be used which is called Cascade ΔP Control. The method was first introduced by Sepheri et al. [33] and was then further advanced and realized by Heintze et al. [15] This control strategy splits up the control problem into two smaller problems. First a loop is designed around the hydraulic actuator using pressure feedback such that a force reference can be supplied to the closed loop system. The hydraulic actuator therefore has been changed from a velocity generator to a force generator by means of this loop. Around this loop it is now possible to design another closed loop controller that controls the motion by providing force references to the inner loop controller. This controller is a model-based feedforward controller that is widely applied [1]. The outer-loop controller makes use of a feedforward force signal F_{ff}, which in this case is calculated using the trajectory and the inverse dynamics of the Stewart platform. Therefore model information is used to obtain this feedforward term. The desired actuator length q_d and velocity $\dot{q}_d$ are calculated using the trajectory and the inverse kinematics of the hexapod. Using the feedforward force and differences between the desired and measured actuator leg extensions q_d and velocities $\dot{q}_d$ the reference force F_{ref} The control strategy is presented in the structure for the SRS by means of a block diagram in figure 3.3.
It should be noted that in this diagram the inverse kinematics and dynamics, needed to calculate the desired actuator velocities and extensions, and feedforward forces respectively, are also included as opposed to figures 3.1 and 3.2. They are included due to the fact that this is also the control strategy that is currently being used for the SRS and the diagram therefore provides a more thorough overview of the current controller.

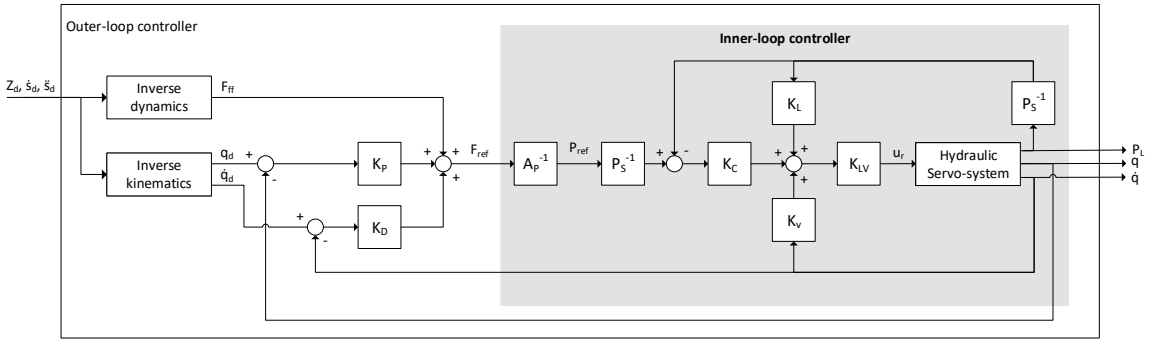

Figure 3.3: A cascaded control structure with inner loop force control and outer loop motion control

$$K_L = \frac{L_{lm}}{\phi_n} \qquad (3.1) \qquad K_V = \frac{A_p}{\phi_n} \qquad (3.2) \qquad K_{LV} = \frac{1}{\sqrt{1 \pm P_L / P_S}} \qquad (3.3)$$

The Cascade ΔP controller for the SRS was first designed by Schothorst for the single hydraulic actuator case. [39] Koekebakker then took this design and implemented it for the whole simulator. [22] It is now also still the controller used during nominal operation.
In order to calculate the feedforward term inverse dynamics of the Stewart-platform are used and some of the gains are calculated based on model information as shown by equations 3.1, 3.2 and 3.3, where L_{lm} is the main leakage parameter, ϕ_n is the maximum valve flow, A_p is the piston area, and P_S is the supply pressure. The other gains are to be tuned. Some of the gains as well as the inverse dynamics are therefore based on model information and therefore the controller is sensitive to model mismatches and disturbances. It would therefore be desirable to have a controller that is less sensitive to these uncertainties and still able to accurately track the references. Such a controller is available and will be discussed in the next section.

3.4. Generalized cascaded structure with INDI

The strategy of splitting up the control problem into two separate problems to deal with the load dependence can also be adopted for different inner and outer loop controllers as the ones depicted in figure 3.3. If this dual strategy is generalized the structure can be represented as figure 3.4.

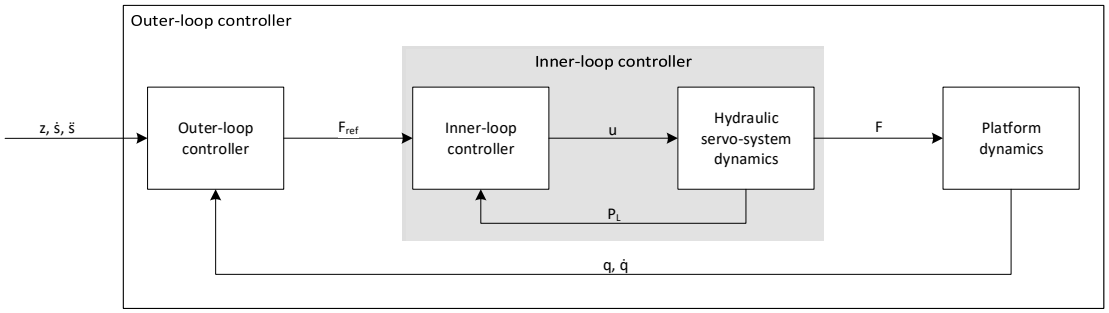

Figure 3.4: A generalized hydraulic cascaded control structure

This structure was also used by Huang for the SRS, who used a cascaded structure with both an inner and outer loop Incremental Nonlinear Dynamic Inversion (INDI) controller. [16] The advantage of INDI controllers is that they use less model information and are therefore more robust against model uncertainty. The controllers have also shown to be more accurate in terms of tracking performance. [16] These controllers together with the currently implemented cascade ΔP controller will therefore be used as a basis in this thesis. In the next chapters INDI in general and the specific controllers for the SRS will be discussed in more detail.

4

Inner loop INDI controller

The current CdP controller makes significant use of model information to determine the inner loop controller gains. It would be beneficial to have a controller that is less dependent on model parameters, making it is more robust against uncertainties in these parameters. For this reason Huang has investigated and implemented a novel Incremental Nonlinear Dynamic Inversion (INDI) controller as inner loop controller for the SRS [18]. This chapter will discuss the general principle of this INDI controller and adaptations done to the filter and control gains to increase both the stability and performance of it. At the end the topic of sensitivity to model mismatches and sensor delays of the controller is treated.

4.1. Incremental Nonlinear Dynamic Inversion

The principle of INDI is to calculate increments to the control input instead of the whole control input at each time instance [34]. A first order Taylor expansion is applied to the model of the system to obtain the format to be used for the incremental structure. Due to this structure a lot of model information disappears from the equation and is replaced by sensor information. This makes the controller less dependent on model information than other model-based controllers. The controller does however become more dependent on the accuracy of the measurements [34]. The INDI principle has been successfully applied in practice to various flight control applications such as Micro Air Vehicle disturbance rejection [36] and passenger aircraft control [14]. The approach as developed by the Control & Simulation department at the TU Delft is discussed in this section.

To demonstrate the principles of INDI the nonlinear input-affine control system as presented by equation 4.1 is considered. In this equation $\mathbf{x}$ is the state vector of the system, $\mathbf{y}$ is the output vector, $\mathbf{f(x)}$ and $\mathbf{h(x)}$ are vector field in $\mathbb{R}^n$ and $\mathbb{R}^m$ respectively, and $\mathbf{G(x)}$ is the state-dependent $n \times m$ control effectiveness matrix.

$$\begin{aligned} \dot{\mathbf{x}} &= \mathbf{f(x)} + \mathbf{G(x)}\,\mathbf{u} \\ \mathbf{y} &= \mathbf{h(x)} \end{aligned} \tag{4.1}$$

The principle of INDI is based on a first order Taylor expansion around the system at the previous time. The incremental properties of this expansion can then be used to calculate the new input based on the old input and measurements. Equation 4.3 is obtained we set the output vector equal to the derivative of the state vector and apply a first order taylor expansion to the above control affine system.

$$\mathbf{y} = \dot{\mathbf{x}} = \dot{\mathbf{x}}_0 + \frac{\partial}{\partial \mathbf{x}} \left[\mathbf{f(x)} + \mathbf{G(x)}\,\mathbf{u}\right]_{\mathbf{x}_0,\mathbf{u}_0} (\mathbf{x} - \mathbf{x}_0) + \frac{\partial}{\partial \mathbf{u}} \left[\mathbf{f(x)} + \mathbf{G(x)}\,\mathbf{u}\right]_{\mathbf{x}_0,\mathbf{u}_0} (\mathbf{u} - \mathbf{u}_0) \tag{4.2}$$

$$\mathbf{y} = \dot{\mathbf{x}} = \dot{\mathbf{x}}_0 + \frac{\partial}{\partial \mathbf{x}} \left[\mathbf{f(x)} + \mathbf{G(x)}\,\mathbf{u}\right]_{\mathbf{x}_0,\mathbf{u}_0} (\mathbf{x} - \mathbf{x}_0) + \mathbf{G(x)}\,(\mathbf{u} - \mathbf{u}_0) \tag{4.3}$$

To simplify this equation the time-scale separation principle will be applied [7]. When the sampling rate is high enough and the actuator dynamics are considerably faster than the general system dynamics it can be assumed that $\mathbf{x}_0 \cong \mathbf{x}$ while at the same time $\mathbf{u}_0 \neq \mathbf{u}$. Because of this assumption a term in equation 4.3 drops and equation 4.4 is obtained

$$\dot{\mathbf{x}} = \dot{\mathbf{x}}_0 + \mathbf{G(x)}\,(\mathbf{u} - \mathbf{u}_0) \tag{4.4}$$

It is now possible to rewrite equation 4.4 for the control input and set the new control input to this rewritten equation, which is called the virtual control $\boldsymbol{\nu}$, equal to $\dot{\mathbf{x}}$ resulting in equation 4.5

$$\mathbf{u} = \mathbf{u}_0 + \mathbf{G}^{-1}(\mathbf{x})\ (\boldsymbol{\nu} - \dot{\mathbf{x}}_0) \tag{4.5}$$

The above equation shows that the control law does not depend on $\mathbf{f(x)}$ anymore and therefore uses less model information. The controller is therefore more robust against uncertainties to this part of the model. The only model information left is contained by the control effectiveness matrix $\boldsymbol{G(x)}$. It should however be noted that an additional term $\mathbf{x}_0$ has been added, which represents the new measurements to be included. The performance sensitivity of the controller has therefore shifted from model to measurement accuracy [34].

4.2. Application to the inner loop

Huang [18] used the simplified expression for the hydraulic servo-system as derived by Schothorst [39] as a basis for the INDI controller. This simplified expression is already explained in more detail in chapter 2 and is shown again by equation 4.6 for convenience.

$$\dot{P}_L = 2C_m(q)\left(\phi_n\sqrt{1 \pm P_L/P_S}u - L_{lm}P_L - A_P\dot{q}\right) \tag{4.6}$$

$$\phi_n = C_d A_m \sqrt{\frac{P_S}{\rho}} \tag{4.7}$$

$$C_m(q) = \frac{1}{2}\left(\frac{E}{V_1(q)} + \frac{E}{V_2(q)}\right) \tag{4.8}$$

$$\begin{aligned} V_1(q) &= V_m + A_P q \\ V_2(q) &= V_m - A_P q \end{aligned} \tag{4.9}$$

Equation 4.10 is obtained when the Taylor expansion and the time-scale separation principle are applied to equation 4.6. Using the time-scale separation principle all terms are neglected that are not part of the control effectiveness term in the expansion.

The sampling frequency that is used for the SRS is 5 kHz. The bandwidth of the servo-valve lies around 250 Hz and the specified closed loop bandwith of the controller at 15 Hz [39]. Therefore, the actuator dynamics and sampling frequency lie at least an order of magnitude higher than the system dynamics. This is why the time-scale separation principle can be applied and the terms drop in the Taylor expansion.

$$\dot{P}_L = G(x)(u - u_0) = 2C_m(q)\phi_n\sqrt{1 \pm P_L/P_S}\,(u - u_0) \tag{4.10}$$

The above equation is rewritten for the control input and $\dot{P}_L$ is chosen as virtual control such that equation 4.11 is obtained. This equation represents the basic form of the INDI control law to be used for the inner loop controller of the SRS.

$$u = u_0 + G(x)^{-1}(\nu - \dot{P}_{L0}) = u_0 + \frac{1}{2C_m(q)\phi_n\sqrt{1 \pm P_L/P_S}}(\nu - \dot{P}_{L0}) \tag{4.11}$$

In practice the control input is sent to an electro-hydraulic servo-valve which adds delay and additional effects such as saturations to the system. The commanded value to the servo-valve represents the main-spool position to be achieved. For this reason it would be more accurate to change u to x_m due to the dynamics present of the servo valve as presented by equation 4.12, where S represents the servo-valve dynamics. The new differential equation describing the system is presented by equation 4.13

$$x_m = S\ u \tag{4.12}$$

$$\dot{P}_L = 2C_m(q)\left(\phi_n\sqrt{1 \pm P_L/P_S}x_m - L_{lm}P_L - A_P\dot{q}\right) \tag{4.13}$$

When a Taylor expansion is applied to equation 4.13 and the equation is presented in the time domain it can be represented as equation 4.14. Equation 4.15 is obtained when 4.12 is inserted in equation 4.14 and then rewritten. This equation if then transformed to the Laplace domain such that equation 4.16 is obtained. This can be simplified to 4.17 through dividing by equal terms on both sides.

$$\dot{P}_L(t) = \dot{P}_L(t-\Delta t) + G(x)(x_m(t) - x_m(t-\Delta t)) \tag{4.14}$$

$$\dot{P}_L(t) - \dot{P}_L(t-\Delta t) = +G(x)S(u(t) - u(t-\Delta t)) \tag{4.15}$$

$$(1 - e^{-\Delta ts})\dot{P}_L(s) = G(x)S(1 - e^{-\Delta ts})U(s) \tag{4.16}$$

$$\dot{P}_L(s) = G(x)\,S\,U(s) \tag{4.17}$$

Equation 4.18 is obtained when equation 4.11 is rewritten in the time-domain. After conversion from the time-domain to the Laplace domain equation 4.19 can be obtained, which can be rewritten to equation 4.20

$$u(t) - u(t-\Delta t) = G(x)^{-1}(v - \dot{P}_L(t-\Delta t)) \tag{4.18}$$

$$(1 - e^{-\Delta ts})U(s) = G(x)^{-1}(V(s) - e^{-\Delta ts}\dot{P}_L) \tag{4.19}$$

$$U(s) = G(x)^{-1}\frac{V(s) - e^{-\Delta ts}\dot{P}_L}{1 - e^{-\Delta ts}} \tag{4.20}$$

Insertion of equation 4.20 in 4.17 results in equation 4.21. This can be rewritten to 4.23, which represents the dynamics in the Laplace domain between the input from the valve $V(s)$ and the pressure difference derivative $\dot{P}_L$.

$$\dot{P}_L(s) = \frac{S\,V(s) - S\,e^{-\Delta ts}\dot{P}_L}{1 - e^{-\Delta ts}} \tag{4.21}$$

$$(1 - e^{-\Delta ts} + S\,e^{-\Delta ts})\dot{P}_L(s) = S\,V(s) \tag{4.22}$$

$$\dot{P}_L(s) = \frac{S}{1 - e^{-\Delta ts} + S\,e^{-\Delta ts}}V(s) \tag{4.23}$$

From equation 4.23 it can be found that the servo-valve dynamics S show up in the numerator. In the denominator the valve dynamics allow the term $-e^{-\Delta ts} + S\,e^{-\Delta ts}$ to be present which would disappear when the valve dynamics would not be present. The extra term in the denominator introduces phase delay in the system that has a negative impact on the phase margin. If we approximate S with the 5^{th} order valve model and set Δt equal to 0.0002 we can represent the transfer function in the complex plane as shown by figure 5.2. In this figure it can be seen that a pole is present in the Right Half Plane (RHP) that could lead to unstable behavior.

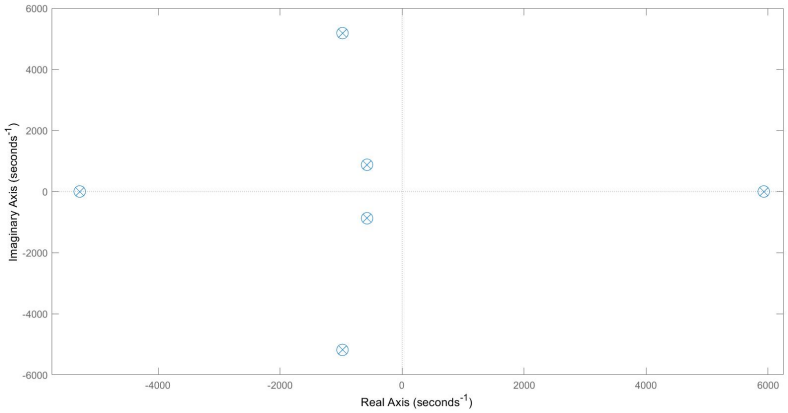

Figure 4.1: Pole-zero plot of equation 4.23 with S as the 5^{th} order servo valve model and Δt equal to 0.0002. The time delays are approximated using the pade approximation method [11]

In order to get rid of this RHP pole the servo-valve dynamics are added to the incremental feedback signal of the INDI controller. By adding the servo-valve dynamics to this signal the two delay terms in the denominator cancel. This results in a transfer function that only has the servo-valve dynamics term. The presence of the servo-valve dynamics is to be expected as they are not taken into account by the dynamic inversion. The resulting transfer function is shown by equation 4.24.

$$\dot{P}_L(s) = SV(s) \tag{4.24}$$

In practice the measurement of x_m should be used instead of the previous commanded value, such that the servo-valve dynamics are taken into account for the signal. The resulting system is shown in block diagram format in figure 4.2. In the figure the electro-hydraulic servo-valve as well as the hydraulic actuator are included. The block Z^{-1} represents an unit delay in the discrete time domain and the block $\frac{Z-1}{T_s Z}$ the discrete time derivative.

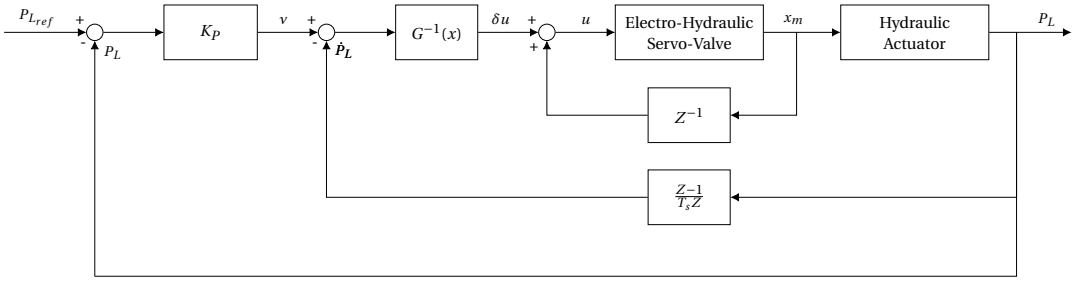

Figure 4.2: Block diagram of the inner loop INDI controller using x_m as the incremental feedback

4.3. Filter design

Schothorst found that for the SRS unstable interactions between the transmission lines and servo-valve dynamics are present. These interactions can result in resonation at the natural frequency of the transmission lines [39]. It is therefore possible that an oscillation presents itself during operating with a frequency around 200 Hz and amplitude that increases with time.

Both Schothorst and Huang have found these oscillations to be present during experiments with their controllers. Schothorst dealt with this issue by implementing a dynamic feedback compensator that creates phase lead as well as gain attenuation in the critical frequency region and delays the feedback signal to move these frequencies away from their unstable region. The filter design includes three filters C1, C2, and C3 placed at the feedback signal, input signal, and reference signal respectively.

Huang slightly adapted these filters such that they better fit the INDI controller by splitting up the C1 filters in two new filters C6 and C5 which are placed on the pressure change derivative feedback and pressure change feedback signals respectively. Due to the fact that the inner feedback signal, which in this case is the pressure difference derivative feedback signal, needs to be synchronized with the incremental loop the C5 filter is also applied this loop [16]. The need for synchronization will be treated in more detail in the next section. The C4 filter constitutes the C5 filter with an additional derivative term. The discrete time derivative block can be omitted due to this additional term. The filter design by Huang will be taken as basis. The block scheme representation of the inner loop controller with additional filters is shown in figure 4.3, with corresponding transfer functions given by the equations presented by 4.25.

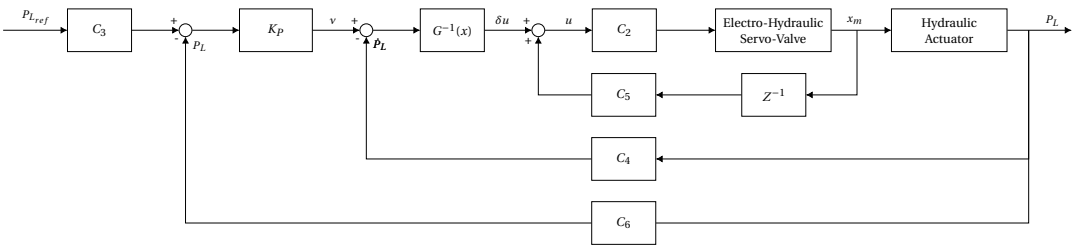

Figure 4.3: Block diagram of the inner loop INDI controller including the filter design

$$C_1 = \frac{1}{\frac{1}{(2\pi 75)^2}s^2 + \frac{2\,0.3}{2\pi 75}s + 1}, \qquad C_2 = \frac{1}{\frac{1}{2\pi 100}s + 1}, \qquad C_3 = \frac{\frac{1}{(2\pi 200)^2}s^2 + \frac{2\,0.2}{2\pi 200}s + 1}{\frac{1}{(2\pi 400)^2}s^2 + \frac{2\,0.2}{2\pi 400}s + 1}\,\frac{1}{\frac{1}{(2\pi 150)^2}s^2 + \frac{2\,0.6}{2\pi 150}s + 1}$$
$$C_4 = \frac{(2\pi 35)^2\, s}{s^2 + 2\,0.3(2\pi 35) + (2\pi 35)^2}, \quad C_5 = \frac{(2\pi 35)^2}{s^2 + 2\,0.3(2\pi 35) + (2\pi 35)^2}, \quad C_6 = \frac{(2\pi 50)^2}{s^2 + 2\,0.3(2\pi 50) + (2\pi 50)^2} \tag{4.25}$$

4.4. Synchronization of the INDI loops

The simple control structure of the inner part of the INDI controller presented in figure 4.4 will be used to demonstrate the need for synchronization of the incremental loop and the inner feedback loop. In this structure a filter A is placed on the inner feedback loop of the controller and B on the incremental loop of the controller.

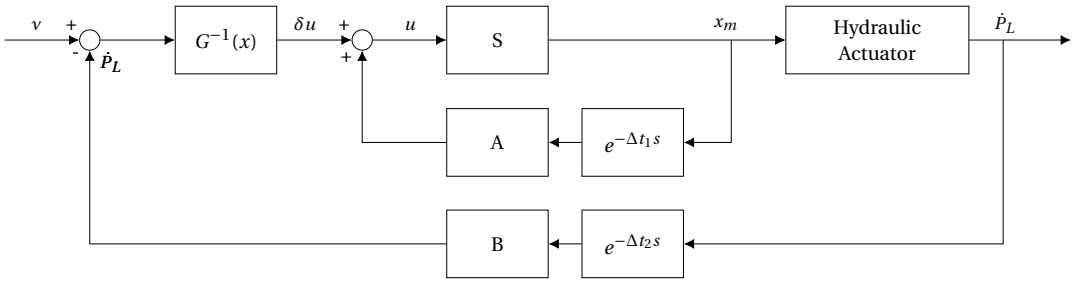

Figure 4.4: Block diagram of the linearization loop of the inner loop INDI controller including delays and filters on the incremental and feedback signals

Considering the inner linearization loop with the aforementioned delays and filters it is possible to represent the input signal to the servo-valve as equation 4.26. In this equation A and Δt_1 represent the filter an delay for the incremental loop. B an Δt_2 represent the filter an delay for the feedback loop. Equation 4.29 is obtained when the equation is transformed to the Laplace domain and manipulated.

$$u(t) = u(t-\Delta t)\,S\,A + G(x)^{-1}(v - \dot{P}_L(t-\Delta t)\,B) \tag{4.26}$$

$$u(t) - u(t-\Delta t)\,S\,A = G(x)^{-1}(v - \dot{P}_L(t-\Delta t)\,B) \tag{4.27}$$

$$(1 - e^{-\Delta t_1 s}\,S\,A)U(s) = G(x)^{-1}(V(s) - e^{-\Delta t_2 s}\,B\,\dot{P}_L) \tag{4.28}$$

$$U(s) = G(x)^{-1}\,\frac{V(s) - e^{-\Delta t_2 s}\,B\,\dot{P}_L}{1 - e^{-\Delta t_1 s}\,S\,A} \tag{4.29}$$

Equation 4.29 is inserted into equation 4.17 such that equation 4.30 is obtained. This can be manipulated to equation 4.32. This equation represents the transfer function between the virtual input V(S) and the pressure difference $\dot{P}_L(s)$.

$$\dot{P}_L = \frac{S\,V(s) - S\,e^{-\Delta t_2 s}\,B\,\dot{P}_L}{1 - e^{-\Delta t_1 s}\,S\,A} \tag{4.30}$$

$$(1 - S\,A\,e^{-\Delta t_1 s}\,A + S\,B\,e^{-\Delta t_2 s})\dot{P}_L(s) = S\,V(s) \tag{4.31}$$

$$\dot{P}_L(s) = \frac{S}{1 - S\,A\,e^{-\Delta t_1 s} + S\,B\,e^{-\Delta t_2 s}}\,V(s) \tag{4.32}$$

Δt_1 and Δt_2 can be assumed to be equal when the delays in both measurement signals are equal. Using this assumption equation 4.33 is obtained.

$$\dot{P}_L(s) = \frac{S}{1 - S\,e^{-\Delta t s}(A - B)}\,V(s) \tag{4.33}$$

Equation 4.33 shows that the term in the denominator would disappear only if the filters A and B are equal. If the filters are equal only the valve dynamics S remain. For now it is assumed that the delays are not present. It is also assumed that filter A and servo-valve dynamics S are equal to 1, resulting in equation 4.34.

$$\dot{P}_L(s) = \frac{1}{B} V(s) \tag{4.34}$$

Equation 4.34 shows that for any value of B that is not equal to 1 the input and output would not directly relate. This shows that the performance degrades when the filters in both loops are not equal.

It was assumed that there was no delay for the two signals. The delays can however cause poles to show up in the Right Half Plane (RHP). This assumption is removed again to demonstrate the possibility for existence of these RHP poles. It is assumed that there is no delay in the incremental signal, but there is a delay in the feedback signal of the inner INDI feedback loop. It is also assumed that filters A and B and the servo-valve dynamics S are not present. Using these assumptions equation 4.35 is obtained from 4.32.

$$\dot{P}_L(s) = \frac{1}{e^{-\Delta t_2 s}} V(s) \tag{4.35}$$

This equation proves that the output does not directly relate to the input when a delay Δt_2 is present and no delay Δt_1. The closed loop system tracking performance is therefore less for the system with this delay. With the Padè approximation we can approximate $e^{-\Delta t_2 s}$ by equation 4.36 [11]. This can be used to obtain the approximation for equation 4.35 resulting in 4.37.

$$e^{-sT} \cong \frac{\frac{2}{T} - s}{\frac{2}{T} + s} \tag{4.36}$$

$$\dot{P}_L(s) = \frac{1}{e^{-\Delta t_2 s}} V(s) \cong \frac{\frac{2}{\Delta t_2} + s}{\frac{2}{\Delta t_2} - s} V(s) \tag{4.37}$$

Equation 4.37 shows that any positive delay in the feedback signal would cause the transfer function to contain a pole in the right half plane. This pole could cause unstable output behavior. It is therefore of importance to keep the delays and the filters in both loops equal such that these right half plane poles do not show up in the transfer function.

4.5. Simulation of the baseline controllers

A simulation is now be performed to create understanding of the performance of the current CdP and INDI inner loop controllers as implemented on the SRS. For the inner loop CdP controller the gains are chosen to be equal to the gains as currently implemented on the SRS. For the inner loop CdP controller this means that the K_v, K_c, and K_L gains are equal 0.8, 0.5, and 0.025 respectively. It is however found that a K_v of 0.9 as proposed by Koekebakker [22] gave better results and in order to fairly compare the two control strategies of different nature both gains will be used for the evaluation.

For the inner loop INDI controller there is only a single proportional gain in the linear controller, which is set to 80. For the simulation the full hydraulic actuator model is used together with the 5^{th} order servo-valve model. The model for the transmission lines is included as well. The outputs of both controllers to an alternating step response with an amplitude of 0.1 and period of 0.5s are shown in figure 4.5.

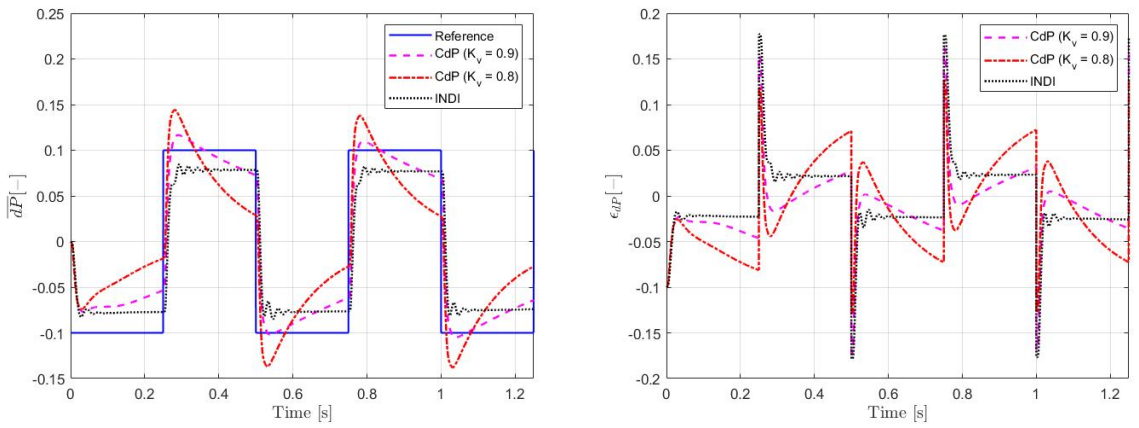

(a) Pressure responses

(b) Control errors

Figure 4.5: Responses of the baseline CdP controllers with two different K_v gains and baseline INDI controller to an alternating step reference

The performance of the INDI controller and the CdP controller with a K_v of 0.9 lie close to each other with an MAE and RMSE of 0.0354 and 0.0412, and 0.0237 and 0.0303 respectively. The CdP controller is performing slightly better for this specific reference. A K_v of 0.8 is currently being used for the SRS. The CdP controller with the gain of 0.8 shows worse performance when compared to the INDI controller with an MAE and RMSE of 0.0435 and 0.0499 respectively. It can also be seen that the INDI controller has a more consistent steady state error and that at this moment only a proportional gain is used in the linear controller. In the next section the addition of integral gain will therefore be treated. To get a more thorough evaluation of the performance the responses of the controllers to a sinusoidal reference will be evaluated. The sinusoid to be tracked has a frequency of 1 Hz and an amplitude of 0.1. The responses can be observed in figure 4.6

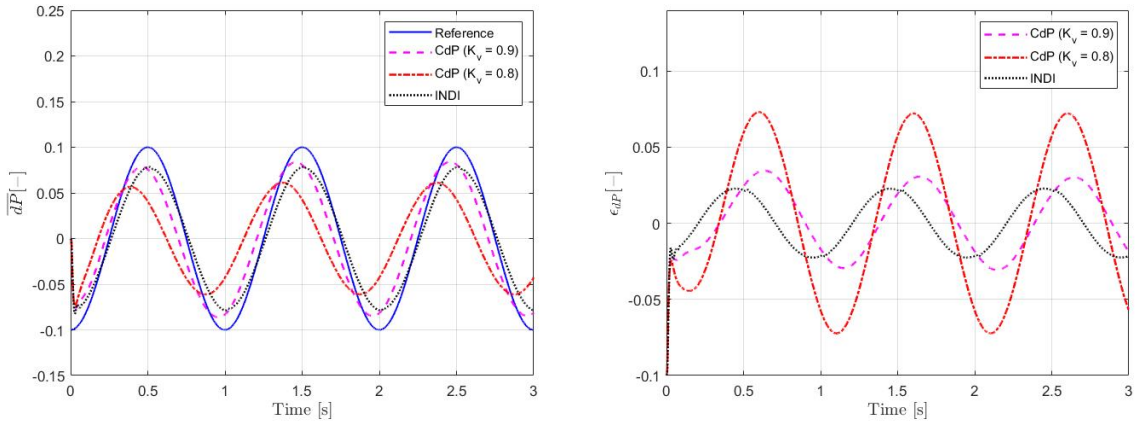

(a) Pressure responses

(b) Control errors

Figure 4.6: Responses of the baseline CdP controllers with two different K_v gains and baseline INDI controller to a sinusoidal reference

For this reference the INDI controller is performing best with an MAE of 0.0152 and a RMSE of 0.0175 as opposed to the best performing CdP controller with an MAE of 0.0191 and RMSE of 0.0218. Therefore, for these references the controllers lie close together in terms of performance. The known advantage of INDI is however that it can deal with unrealistic amounts of model uncertainty and model mismatches, which was also found by Huang during his experiments on the SRS [16]. The aforementioned possibility for improvement by adding integral gain to the linear controller in the INDI controller together with the advantage of robustness against such uncertainties and mismatches makes the INDI controller a promising controller. Huang has also found in his experiments that the controller does indeed outperform the CdP controller for the SRS and is more robust against model mismatches and uncertainties [16].

4.6. Simulation of controller with integral gain and adjusted filters

Figure 4.5 shows that there is a steady-state error for the INDI controller and that also a slight oscillation is present. In order to remove the transient error an integral gain will be added to the linear controller so that a PI controller is obtained. To reduce the oscillations the gain is reduced from 80 to 60 and the damping of the C4 and C5 filters will be raised from 0.3 to $0.5\sqrt{2}$. The resulting controller is shown in figure 4.7.

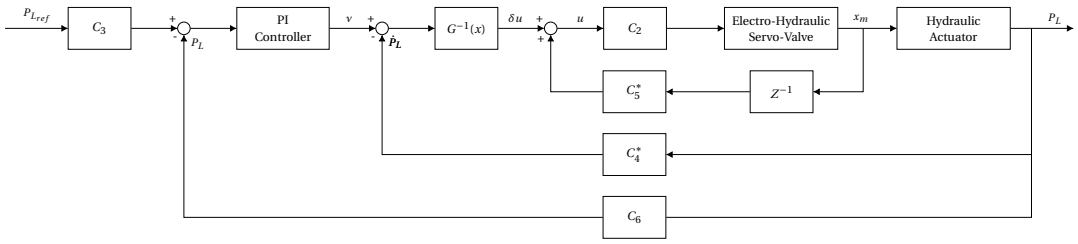

Figure 4.7: Block diagram of the inner loop INDI controller using the adjusted filter design

$$C_4^* = \frac{(2\pi 35)^2\, s}{s^2 + 2\ 0.707(2\pi 35) + (2\pi 35)^2}, \quad C_5^* = \frac{(2\pi 35)^2}{s^2 + 2\ 0.707(2\pi 35) + (2\pi 35)^2} \tag{4.38}$$

These changes will decrease the control performance in terms of MAE and RMSE, but will increase stability which was found to be of relevance for the current SRS controller especially when delay is present in the measurement signals. The responses of the adjusted controller with varying integral gains are given by figure 4.8.

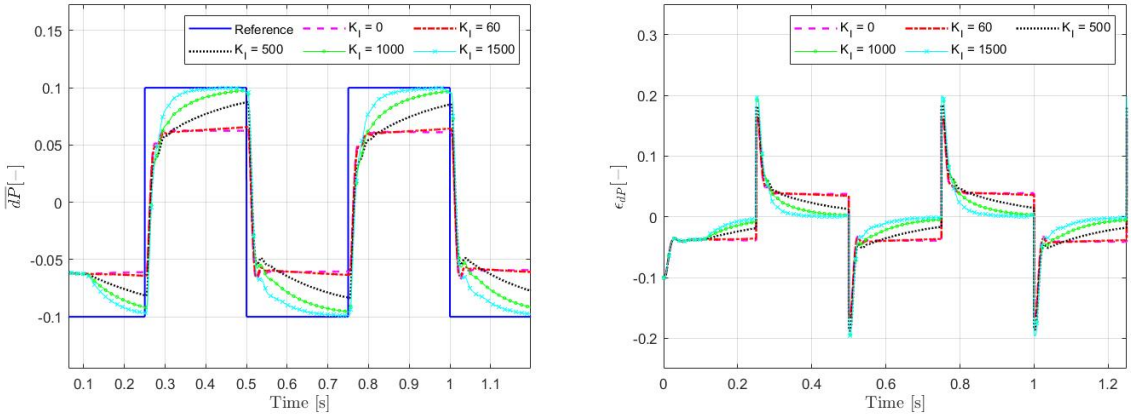

(a) Pressure responses

(b) Control errors

Figure 4.8: Responses of the inner loop INDI controller with adjusted filter gains and varying integral gain to an alternating step reference

The figure shows that the added integral gain does indeed increase the performance in terms of tracking error for the step reference and decreases the steady state error in comparison to the controller without. The sinusoidal reference is also simulated again with this varying integral gain and is shown in figure 4.9.

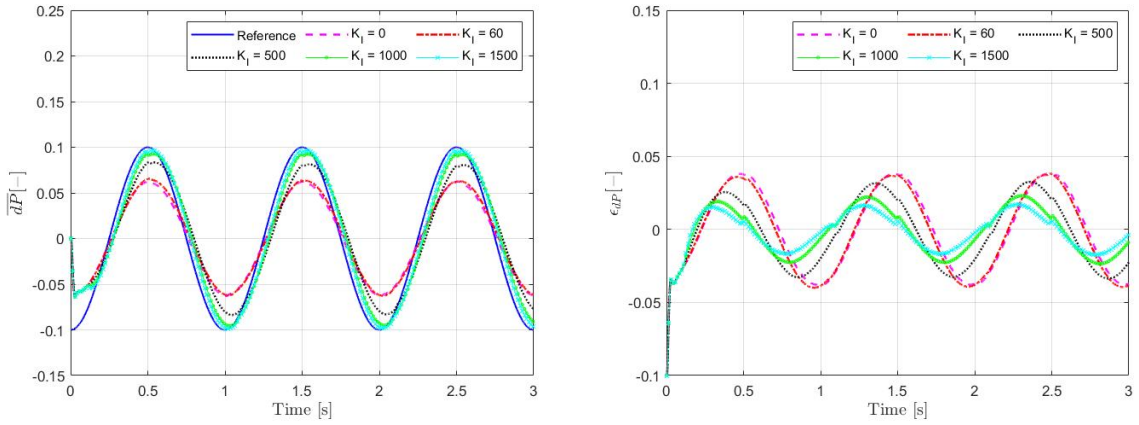

(a) Pressure responses

(b) Control errors

Figure 4.9: Responses of the inner loop INDI controller with adjusted filter gains and varying integral gain to a sinusoidal reference

In the sinusoidal tracking case it is also obvious that the tracking error reduces with increasing gain and therefore the gain of 1500 is chosen as gain for the controller to be used throughout the rest of this work.

4.7. Sensitivity to model mismatches

A known advantage of INDI is that it is more robust against model mismatches and uncertainties. [2] In this section mismatches will be introduced into the model to evaluate the sensitivity of both the CdP controller and INDI controller to these mismatches. Two parameters are used to exemplify the mismatches which are chosen to be the oil density ρ and the hydraulic actuator piston area A_p. The mismatch is varied between 0% and 25% and the resulting responses of the CdP controller to the sinusoidal reference are shown in figure 4.10

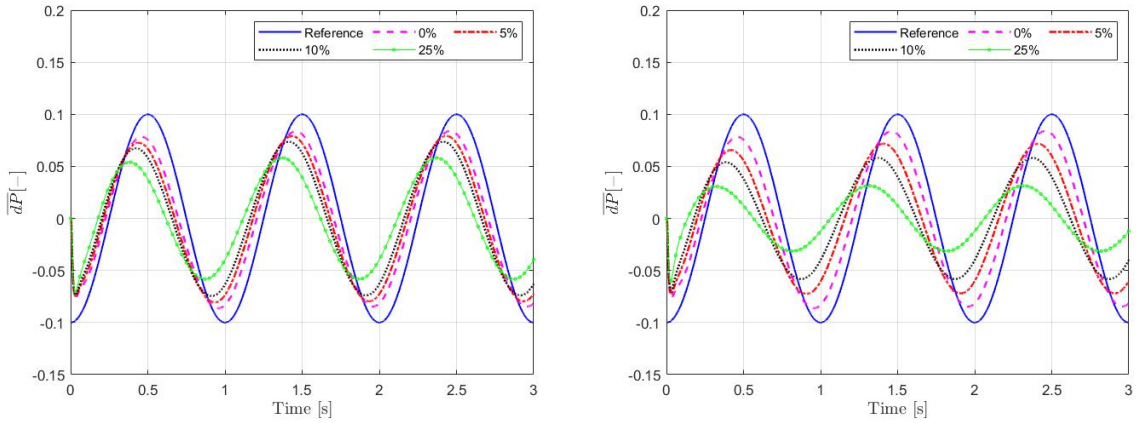

(a) Mismatch of the oil density ρ

(b) Mismatch of the hydraulic actuator piston area A_p

Figure 4.10: Responses of the CdP controller with a K_v of 0.9 and varying offsets for the sinusoidal reference

Figure 4.10 shows that the inner loop CdP controller is indeed sensitive to model mismatches and that it would be beneficial to have a controller that is more robust against these. The presumption that INDI is more robust against these mismatches will therefore be evaluated through simulation. The same mismatches will be applied for the evaluation of the INDI controller. The resulting outputs are shown in figure 4.11.

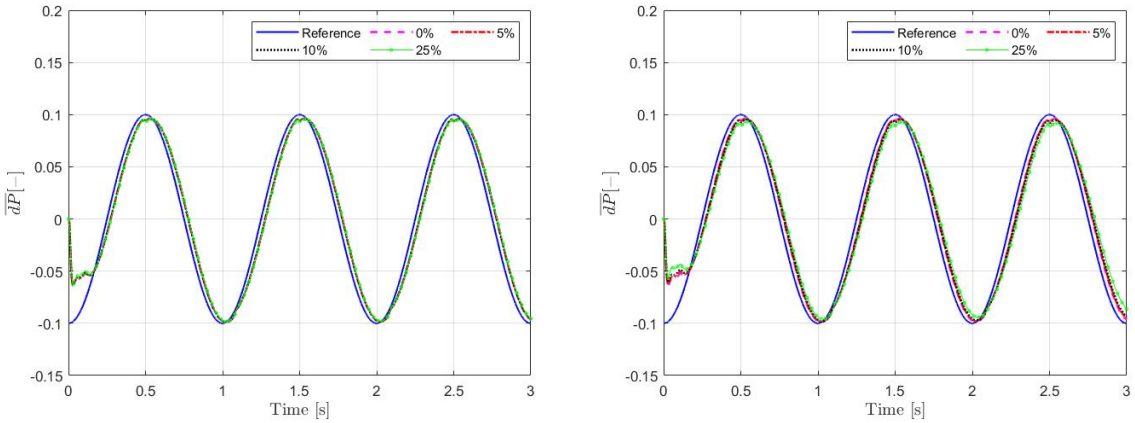

(a) Mismatch of the oil density ρ

(b) Mismatch of the hydraulic actuator piston area A_p

Figure 4.11: Responses of the INDI controller with varying offsets for the sinusoidal reference

From comparison of figures 4.10 and 4.11 it becomes clear that the INDI controller is indeed more robust against the given mismatches which once again confirms the robustness of INDI against model mismatches.

5

Inner loop INDI controller without servo-valve measurements

In previous chapters it was assumed that the measurements for the main spool of the servo-valve were available for the controller. This assumption is valid for the SRS, but in practice it can be difficult to obtain these measurements from the servo-valve. It is not standard practice for the manufacturer to allow for easy extraction of this data. Modifications to the servo-valve might have to be made to extract these measurements. It is therefore of interest for the control to be independent of these measurements. In this chapter it is discussed how a model of the servo-valve is to be used instead of measurements for the inner loop INDI controller.

5.1. Control structure with a servo-valve model

In order to use a model instead of measurements the commanded signal to the valve is taken and used forwarded through a servo-valve model. In order to keep the system stable all the same filters will still have to be applied just as for the case where measurements are used. The control structure for the inner loop using a model is shown in figure 5.1.

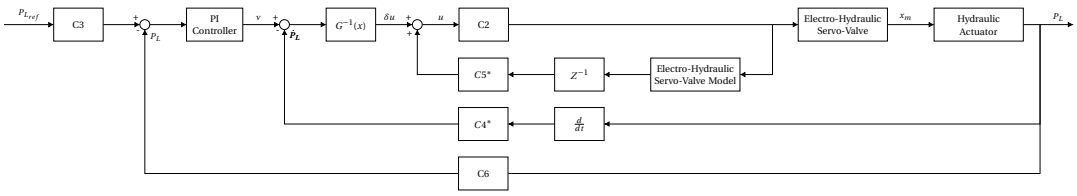

Figure 5.1: Block diagram of the inner loop controller using a servo-valve model instead of measurements

5.2. The three-stage electro-hydraulic servo-valve models

Schothorst has identified a 5^{th} order model for the servo-valve of the SRS which will be used. [39] The proposed model by Schothorst is using a different control law than the SRS. Therefore, the model of the pilot valve will be used together with the proper control law to obtain the appropriate model for the servo-valve used in the SRS. The model he proposed for the pilot valve with accompanying identified coefficients can be found in equation 5.1 and table 5.1 respectively.

$$\begin{bmatrix} \dddot{\tilde{x}}_f \\ \ddot{\tilde{x}}_f \\ \dot{\tilde{x}}_s \\ \Delta\dot{P}_n \end{bmatrix} = \begin{bmatrix} -c_1 & -c_2 & c_3 & c_4 \\ 1 & 0 & 0 & 0 \\ 0 & 1 & -c_5 & c_6 \\ 0 & -c_7 & 1 & -c_8 \end{bmatrix} \begin{bmatrix} \ddot{\tilde{x}}_f \\ \dot{\tilde{x}}_f \\ \tilde{x}_s \\ \Delta P_n \end{bmatrix} + \begin{bmatrix} -c_9 \\ 0 \\ 0 \\ 0 \end{bmatrix} \bar{i}_{ca} \tag{5.1}$$

c_1	4.29e3	c_6	1.00e4
c_2	2.96e7	c_7	9.93e-1
c_3	2.30e10	c_8	4.40e3
c_4	1.13e11	c_9	2.68e10
c_5	1.00e2	c_{10}	1.27e2
K_{pm}	8.00	K_{dm}	4.90e-4

Table 5.1: Identified coefficient values for the reduced flapper nozzle model

Using the model as presented by equation 5.1, the control law shown by 5.2, and the relation between the pilot stage spool position and main spool position derivative as shown by equation 5.3 the new model for the three-stage valve of the SRS is obtained as shown by equation 5.4.

$$\bar{i}_{ca} = K_{pm}(\bar{u}_r - (1 + K_{dm}s)\bar{x}_m) \tag{5.2}$$

$$\dot{\bar{x}}_m \cong c_{10}\bar{x}_s \tag{5.3}$$

$$\begin{bmatrix} \dddot{\tilde{x}}_f \\ \ddot{\tilde{x}}_f \\ \dot{\tilde{x}}_s \\ \Delta\ddot{P}_n \\ \dot{\tilde{x}}_m \end{bmatrix} = \begin{bmatrix} -c_1 & -c_2 & c_3 + c_9c_{10}K_{pm}K_{dm} & c_4 & c_9K_{pm} \\ 1 & 0 & 0 & 0 & 0 \\ 0 & 1 & -c_5 & c_6 & 0 \\ 0 & -c_7 & 1 & -c_8 & 0 \end{bmatrix} \begin{bmatrix} \ddot{\tilde{x}}_f \\ \dot{\tilde{x}}_f \\ \tilde{x}_s \\ \Delta P_n \\ \tilde{x}_m \end{bmatrix} + \begin{bmatrix} -c_9K_{pm} \\ 0 \\ 0 \\ 0 \\ 0 \end{bmatrix} \bar{i}_{ca} \tag{5.4}$$

When a servo-valve is bought the supplier often also delivers data that can be used to generate a 2^{nd} order model of the servo-valve. It is therefore of interest to see what performance a 2^{nd} order model delivers when used in the controller. In order to obtain such a model the 5^{th} order model is used to obtain a reduced model. Part of the pole-zero map for the 5^{th} order model is shown in figure 5.2.

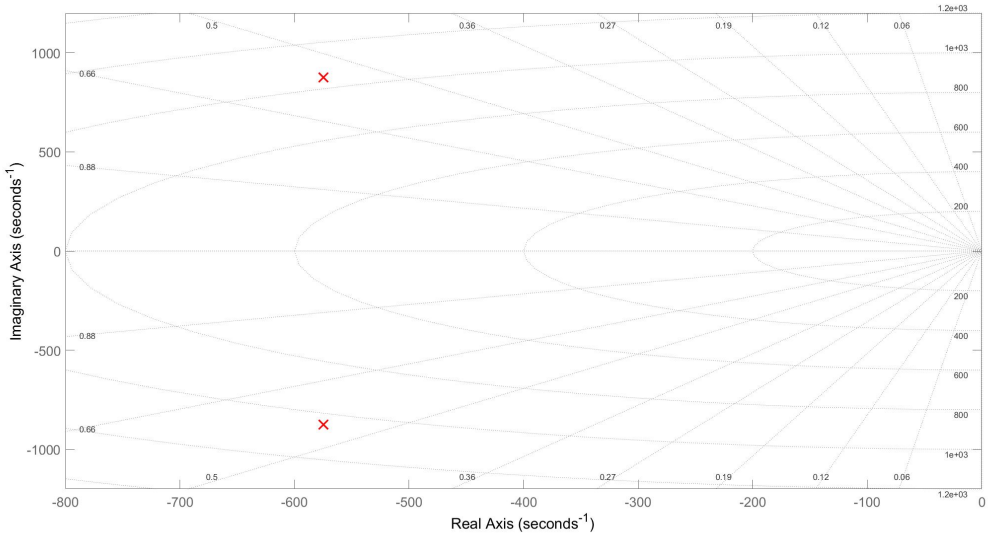

Figure 5.2: Pole zero map for the dominant 5^{th} order model poles of the electro-hydraulic three-stage servo-valve

This pole-zero map shows that the dominant poles lie around $(-575, \pm 876i)$. From these we can extract the natural frequency as well as the damping coefficient of the dominant poles as shown by equations 5.5, 5.6 and 5.7. These can then be used to create the 2^{nd} order model shown by equation 5.8.

$$\omega_n = \sqrt{(Re)^2 + (Im)^2} = \sqrt{(-575)^2 + (876)^2} = 1048[rad/s] \tag{5.5}$$

$$f_n = \frac{\omega_n}{2\pi} = \frac{1048}{2\pi} = 167[Hz] \tag{5.6}$$

$$\zeta = \frac{Re}{\omega_n} = \frac{576}{1048} = 0.550 \tag{5.7}$$

$$\frac{\bar{x}_m}{\bar{u}_r} = \frac{1}{s^2 + 2\zeta\omega_n + \omega_n^2} \tag{5.8}$$

A step response of the 5^{th} order model can be used to determine the time constant of a potential 1^{st} order model. This time constant can be determined using how long it takes the valve to reach $(1-1/e)$%, which is almost equal to 63.2% of its final value. Using the 5^{th} order model a time constant of $1.93E^{-3}$ is obtained, which can be used for the 1^{st} order model as presented by equation 5.9.

$$\frac{\bar{x}_m}{\bar{u}_r} = \frac{1}{\tau s + 1} = \frac{1}{1.93E^{-3}s + 1} \tag{5.9}$$

5.3. Step responses of valve models

The responses of the resulting servo-valve models to a step input of 0.1 are shown in figure 5.3 for the four available models. Slight differences are to be found between the analytical model and the reduced models even for the 5^{th} order model. The 5^{th}, 2^{nd} and 1^{st} order models can now be used in the controllers and the implications of these differences will be shown through simulation in the next section.

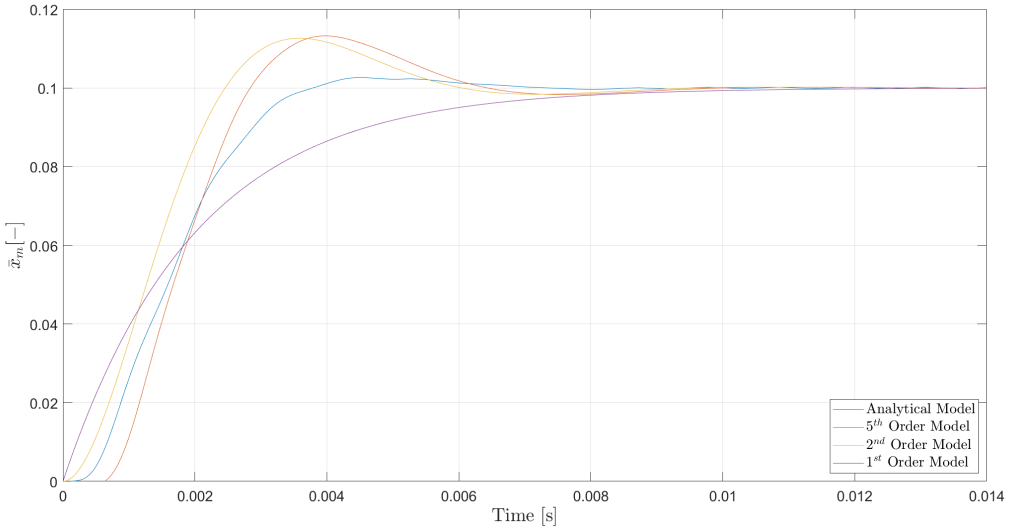

Figure 5.3: Responses of the different servo-valve models to a step input of 0.1

5.4. Simulation results

The responses of the controller using measurements as well as the aforementioned valve models to a sinusoidal reference with an amplitude of 0.1 and a frequency of 1 Hz are shown in figure 5.4.

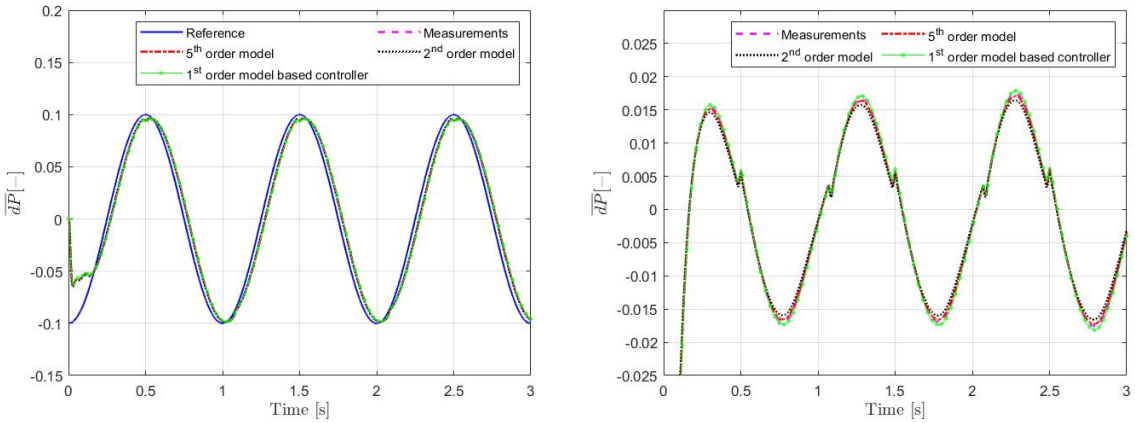

(a) Pressure responses

(b) Control errors

Figure 5.4: Responses of the INDI controller with varying feedback signals for the main spool valve position for the sinusoidal reference

Figure 5.4 shows that the use of either measurements or a valve model nor the order of this model have a major impact on the stability and performance of the controller. This is of great interest as this indicates that it is not necessary to extract and process the signal for the main spool position from the electro-hydraulic servo-valve. For some hydraulic control applications the process of implementing the inner loop INDI controller is therefore simplified.

6

Servo-valve saturations

A common problem in control is that of input saturations that introduces an abrupt nonlinearity into the system [9]. These saturations may lead to phenomena like wind-up [13] and instability [31]. Various solutions exist to deal with this problem, such as designing a controller that adapts itself in the saturation regime like a fuzzy adaptive controller [10], including adaptations that prevent the relevant elements from winding-up [5] or by applying robust control techniques [6]. Another option would be to adjust the reference based on the amount of saturation to prevent the relevant elements from acting upon the saturation, which is exactly what a technique called Pseudo Control Hedging [21] does. In this chapter it will be shown that saturations do occur during nominal operation of the SRS and what the effects of the saturations are on the INDI controller. Hereafter Pseudo Control Hedging (PCH) is implemented to mitigate the negative effects imposed by the saturations. The results of the INDI controller including PCH are shown at the end of this chapter.

6.1. Prove for saturation

In order to decide whether or not it is important to deal with the consequences of servo-valve saturations it would make sense to first look if they do occur at all during nominal operation. The SRS has several safety and performance limits and three of them are the maximum extension of a hydraulic leg q_{max} which equals 0.575 m, velocity of the leg extension v_{max} equal to 1.0 m/s and the maximum acceleration of the leg extension which equals 10m/s^2. The inner loop INDI controller is tracking force references which can be directly related to the acceleration. It is therefore convenient to investigate the presence of saturations for certain acceleration references, which in this case will be a cosine reference with amplitude a_{max} and frequency f as shown by equation 6.1.

$$a(t) = a_{max}\, cos(2\pi f t) \tag{6.1}$$

The limit of the acceleration is reached when a_{max} equals 10 m/s^2. This poses one of the constraints for this reference. To determine the a_{max} at which the velocity limit is reached for this reference it is necessary to first integrate equation 6.1 such that equation 6.2 is obtained.

$$v(t) = \frac{a_{max}\, sin(2\pi f t)}{2\pi f} \tag{6.2}$$

The constraint for the velocity lies at 1.0 m/s as mentioned earlier which arises due to the fact that the servo-valve starts to saturate above this value. Therefore we can rewrite equation 6.2 to show the maximum acceleration as function of frequency due to this constraint as shown by equation 6.3, where it is used that the maximum value of $sin(2\pi f t)$ is 1.

$$a_{max} = 2\pi f\, v_{max} = 2\pi f \tag{6.3}$$

The constraint of the acceleration due to the extension limit will be obtained through integration of equation 6.2 such that equation 6.4 is obtained. The constant for the integration is determined using the fact that the velocity is 0 at t=0. By transforming the result, using the fact that the maximum of $sin(2\pi f t)$ is 1 and that q_{max} = 0.575 equation 6.6 can be obtained.

$$q(t) = \frac{a_{max}}{2\pi f}\left(\frac{1}{2\pi f} - \frac{cos(2\pi f t)}{2\pi f}\right) \tag{6.4}$$

$$q_{max} = \frac{a_{max}}{2\pi f}\left(\frac{1}{2\pi f} - \frac{-1}{2\pi f}\right) = \frac{2a_{max}}{4\pi^2 f^2} \tag{6.5}$$

$$a_{max} = \pi^2 f^2 q_{max} = \pi^2 f^2 0.575 \tag{6.6}$$

It is now possible to plot all the constraints as a function of f such that the lines that represent the constraints for a_{max} are obtained. The resulting plot is shown in figure 6.1 where the white, blue and black line represent the constraints. The green area is the area where the constraints are not violated and the servo-valve does not saturate. The orange area is the area where only the velocity constraint is violated and therefore saturation is occurring. The red area is the area where at least one of the other constraints is violated. The fact that the orange area does exist therefore means that servo-valve saturation can occur during nominal operation. An example saturation case is an acceleration cosine reference with an amplitude of $8m/s^2$ and a frequency of 1Hz.

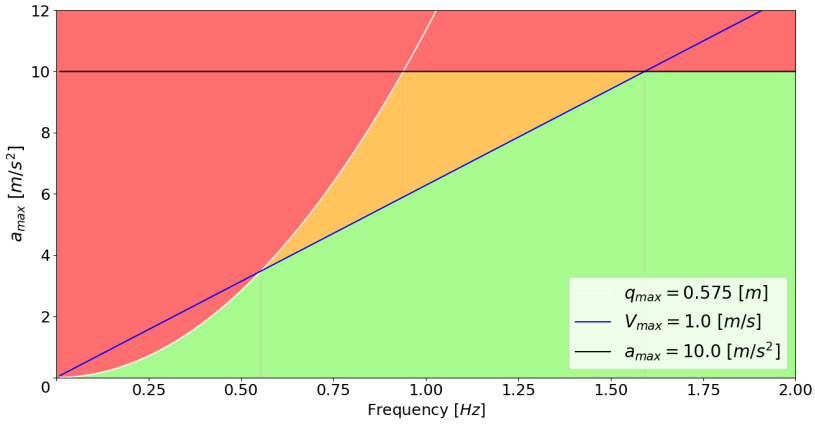

Figure 6.1: Plot of the operating constraints for the SRS for a cosine acceleration reference with varying frequency and amplitude

6.2. Effects of saturations

Now that it has been shown that saturations can occur it is important to better understand the effect of such saturations on the inner loop INDI controller. For the evaluation the basic structure of the controller again without filtering and with proportional and integral gain is considered. The structure is shown in figure 6.2.

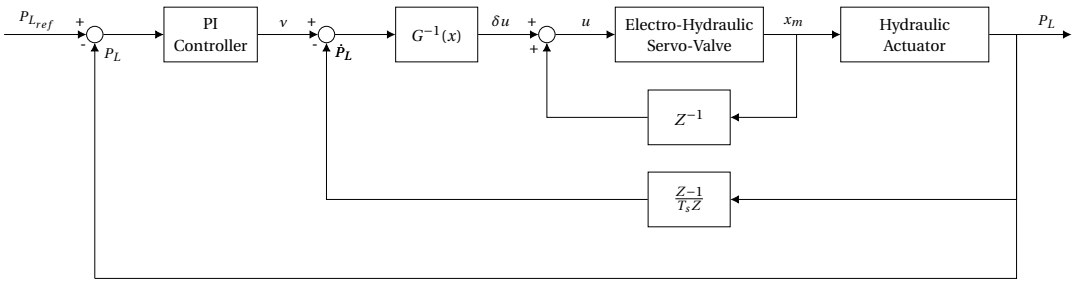

Figure 6.2: Block diagram of the inner loop controller without filters and with an outer linear PI controller

The saturation is taken into account due to the fact that the measured main spool position is used instead of the commanded value for the incremental loop. When the valve saturates, so will the value used for the incremental loop of the INDI controller. This ensures that this loop does not keep increasing further during saturation. For the outer linear controller this is not the case. If integral action is present, it will build up during saturation causing integrator wind-up. This wind-up has a negative impact on the control performance.

In order to exemplify the above a normalized pressure reference with an amplitude of 0.375 and a frequency of 0.94Hz will be tracked by the inner loop controller for both the case where the linear controller does have an integral gain and for the case where it does not. The response of the controllers can be observed in figure 6.3. The commanded and measured servo-valve input as well as the increment to the commanded can be found in figure 6.4

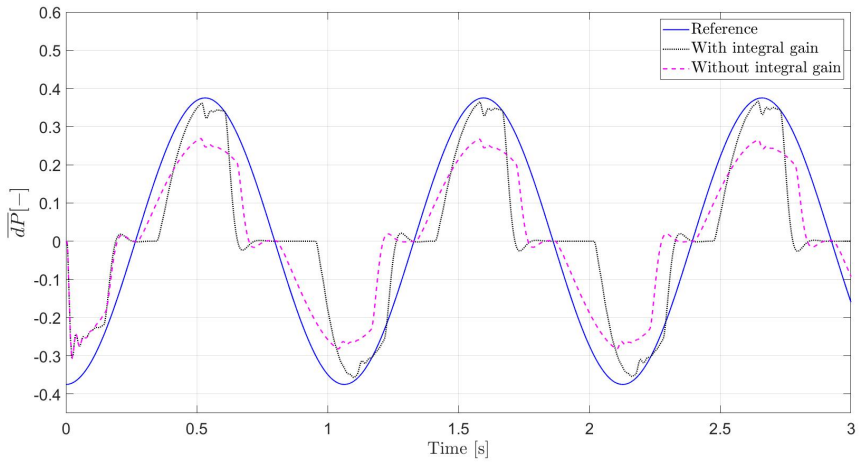

Figure 6.3: Responses of the controller with and without integral gain for a reference with a frequency of 0.75 Hz and an amplitude that corresponds to an acceleration of 9.4 m/s^2

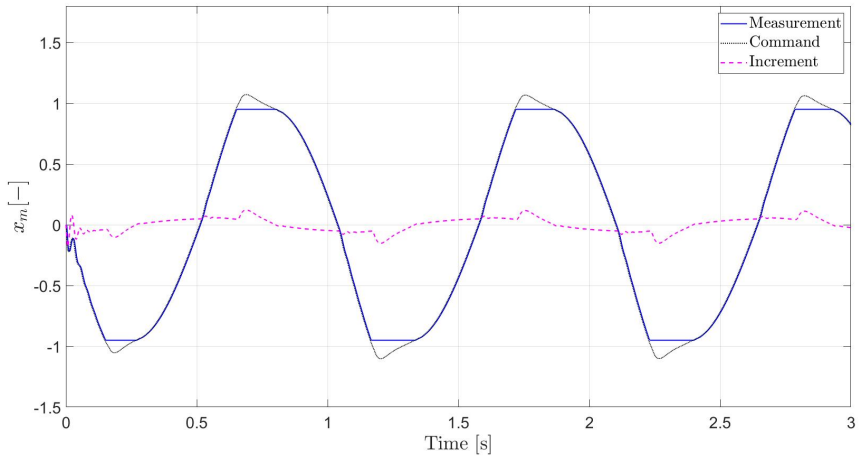

Figure 6.4: Commanded and measured servo-valve main spool position, and INDI increment of the controller with and without integral gain for a reference with a frequency of 0.75 Hz and an amplitude that corresponds to an acceleration of 9.4 m/s^2

In the above figures it can be seen that integral wind-up occurs after saturation for the controller with integral gain. As soon as the servo-valve saturates and the pressure therefore drops to zero the wind-up starts to build up. After saturation the controller without integral gain starts to directly follow the reference again, but the controller with integral gain takes longer as it has to counter the wind-up.

6.3. Pseudo Control Hedging

A strategy to prevent wind-up is adjusting the reference in such a way that the controller will actually never see the point where it saturates. Pseudo Control Hedging (PCH) is such a strategy that prevents the controller from seeing effects such as saturation. [21] It uses the difference between the commanded value to the actuator and the realized value to determine the amount that it should hedge back the reference. The amount it should hedge back is subtracted from the reference using a reference model that allows for the subtraction. The hedging prevents adaptive elements present in the system from acting upon certain system characteristics. [21] One of such characteristics is the saturation. PCH has been effectively applied to various controllers such as nonlinear helicopter flight control using INDI [35], fault tolerant flight control [26] and reusable launch vehicle control [20].

Let us again consider the control law for the INDI controller as presented by equation 6.7 where ν is the virtual control.

$$u = u_0 + G(x)^{-1}(\nu - \dot{x}_0) \tag{6.7}$$

This equation can be rewritten for the virtual control such that equation 6.8 is obtained. The difference between the commanded virtual control and the effective virtual control should be determined to obtain the amount of ineffective virtual control to be hedged , which is presented mathematically by equation 6.9.

$$\nu = \dot{x}_0 + G(x)(u - u_0) \tag{6.8}$$

$$\nu_h = \nu_{com} - \nu_{eff} \tag{6.9}$$

When equation 6.8 is inserted in equation 6.9 for both the commanded virtual control and the effective virtual control it is possible to obtain equation 6.10 that can be simplified to equation 6.11. [35]

$$\nu_h = [u_0 + G(x_0)(u_{com} - u_0)] - \left[u_0 + G(x_0)(u_{eff} - u_0)\right] \tag{6.10}$$

$$\nu_h = G(x_0)\left(u_{com} - u_{eff}\right) \tag{6.11}$$

x_m will be used for the effective input as this is the measured value of the realized main spool position to the valve. In this way equation 6.12 is obtained. This equation represents the virtual control hedge to be subtracted from the reference sent to the INDI controller.

$$\nu_h = G(x_0)\left(u_{com} - x_m\right) \tag{6.12}$$

The virtual control to be hedged back can be subtracted after the PI controller such that the rest of the loop would not see the reference including saturation. The identified problem does however lie at the PI controller where the integral action is winding up during saturation. Therefore, it would be better to hedge the reference back earlier at the point of the force reference. In order to do this we have to use a reference model that momentarily contains the pressure derivative in it such that the virtual control can be subtracted at this point. The used reference model is shown by equation 6.13 and comprises a first order low-pass filter.

$$\frac{P_{L_h}}{P_{L_{ref}}} = \frac{K_{ref}}{s + K_{ref}} \tag{6.13}$$

In this filter we momentarily have the pressure derivative after the gain and at this point the virtual control to be hedged can be subtracted from the reference as shown by the block diagram in figure 6.5. In this block diagram both the PCH as well as the reference model are added to the controller including the filters again.

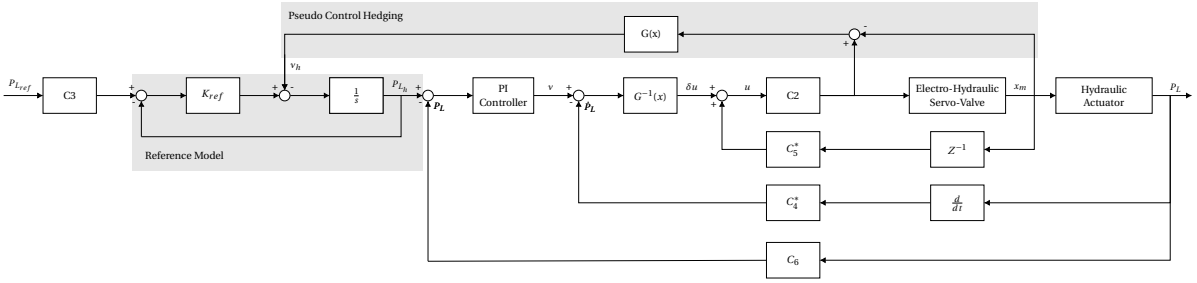

Figure 6.5: Inner loop INDI structure in block diagram format with PCH and the reference model included

One problem arises in the reference model when the virtual control is hedged back. The effectiveness of the hedge is dependent on the reference gain K_{ref} as shown by equation 6.14 that represents the transfer function from v_h to P_L. The effect of the hedge becomes less when the reference gain increases.

$$\frac{P_L(s)}{v_h(s)} = \frac{1}{s + K_{ref}} \tag{6.14}$$

Because the effectiveness of the hedge depends on the reference gain another gain for the hedge is added such that the effectiveness can be tuned. The resulting controller shown by figure 6.6.

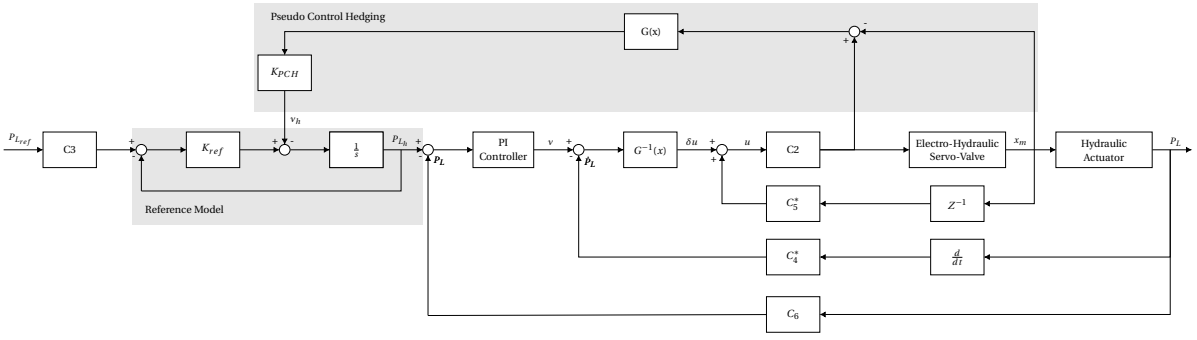

Figure 6.6: Inner loop INDI structure in block diagram format with PCH and the reference model included with the hedging gain K_{PCH}

Now it is possible to simulate the adjusted controller that includes the PCH adjustment for the same reference where saturation occurred with both proportional and integral gain. The result of these simulations with varying values for the virtual control hedge gain K_{PCH} are shown in figure 6.7.

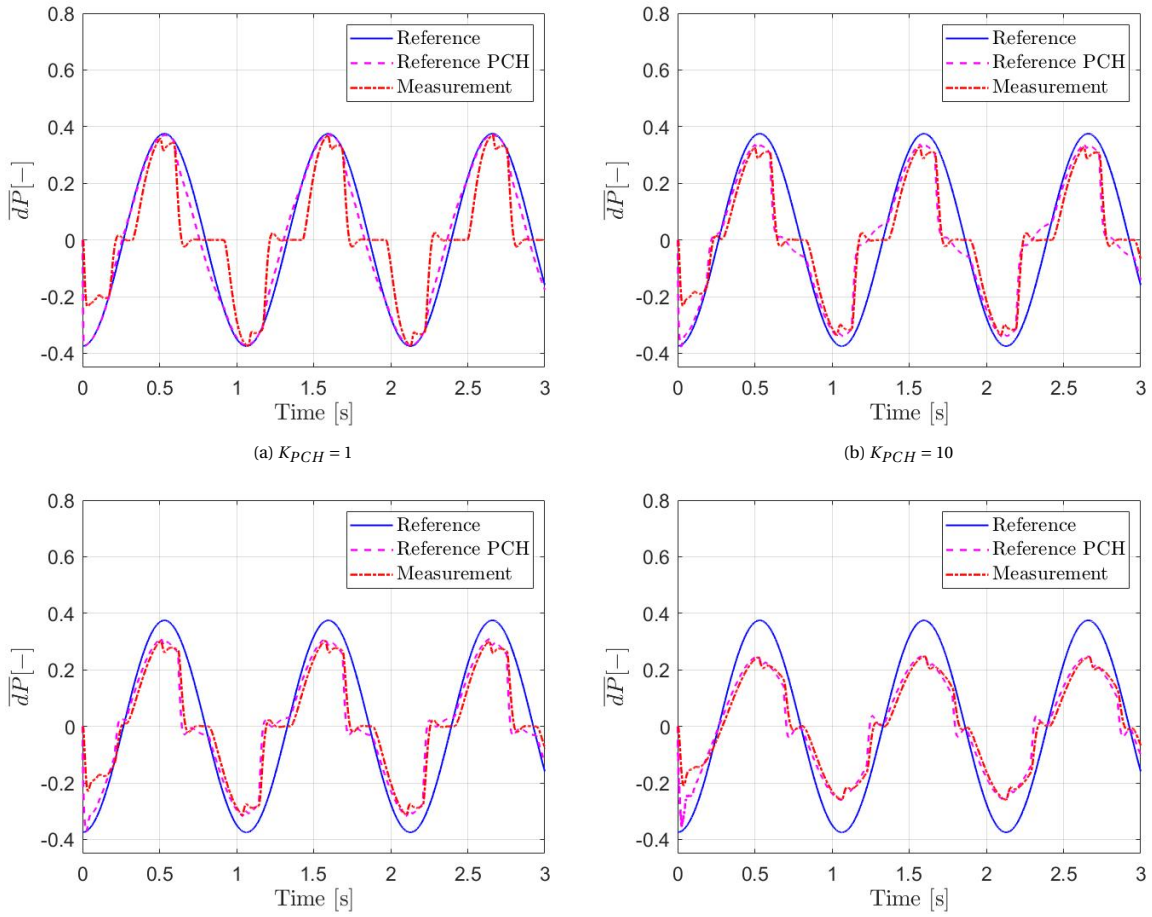

(a) $K_{PCH} = 1$

(b) $K_{PCH} = 10$

(c) $K_{PCH} = 20$

(d) $K_{PCH} = 50$

Figure 6.7: Responses of the controller to a reference that leads to saturation with varying gains K_{PCH} for the PCH

While varying the gain K_{PCH} it becomes clear that the hedging is indeed more effective if the gain increases. Unfortunately, the hedge is not only taking the saturation into account, but also the valve dynamics. Therefore, the hedge is also subtracting the difference between the input and output due to the dynamics of the servo-valve. Which can be shown through inserting equation 6.15 into 6.12 such that equation 6.16 is obtained. It can clearly be seen that indeed any effect is taken into account due to the dynamics of the valve and not only the saturation.

$$u_{eff} = x_m = u\,S \tag{6.15}$$

$$v_h = G(x_0)\,u_{com}(1 - S) \tag{6.16}$$

With the hydraulic actuator we do have the advantage that it is known that the servo-valve will saturate for inputs that are higher than 1. Therefore it would be possible to only hedge back the amount of the input above 1 such that only the saturation and no other dynamics of the valve are taken into account. In this way the hedge can be effective in the case when saturation occurs and have no effect otherwise. Therefore the hedge as presented by equation 6.17 will be used that can be presented in block diagram format as shown by figure 6.8.

$$\nu_h = G(x_0)\,(u_{com} - sat(u_{com})) \tag{6.17}$$

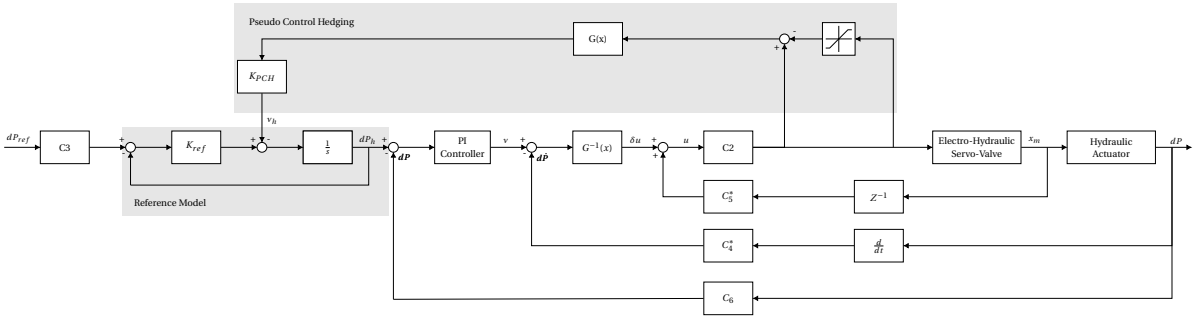

Figure 6.8: Inner loop INDI structure in block diagram format with the adjusted PCH and the reference model included

When the simulation is now executed with the adjusted PCH and same reference as before it can be seen that the hedging does indeed become more effective with increasing hedging gain and that it only effectively hedges during saturation such that no performance is lost during nominal operation. The simulation results are shown in figure 6.10 in which it can also be seen that a gain of 20 is enough to prevent wind-up and appropriately adjusts the reference. For this reason the adjusted PCH together with the gain of 20 will be considered. In figure 6.9 the simulated measured main spool position of the servo-valve for the same simulation can be observed, where it can be seen that the commanded value does indeed stay below the saturation point of 1.0.

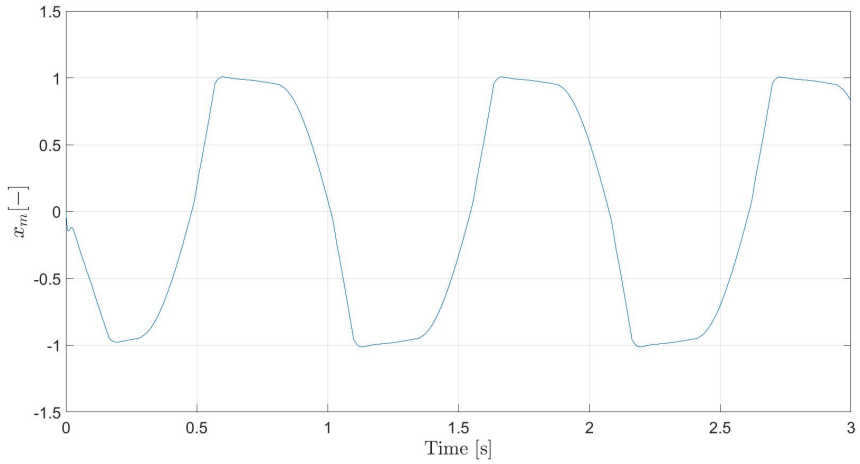

Figure 6.9: Simulated valve measurement of a reference that leads to saturation for the adjusted variant of the PCH

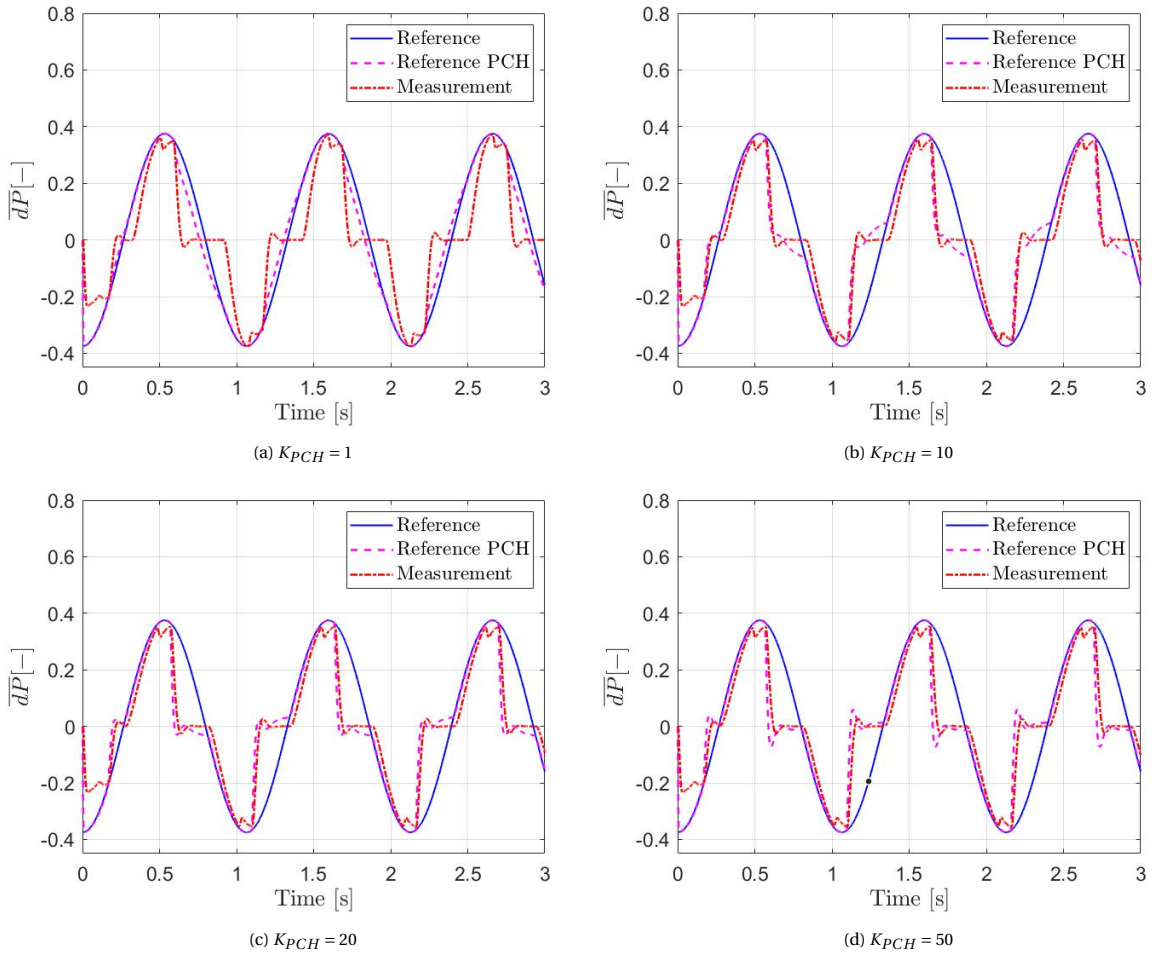

(a) $K_{PCH} = 1$

(b) $K_{PCH} = 10$

(c) $K_{PCH} = 20$

(d) $K_{PCH} = 50$

Figure 6.10: Responses of the controller to a reference that leads to saturation with vayring gains K_{PCH} for the adjusted variant of the PCH

7

Outer loop control

The outer loop controller for the cascaded control strategy uses the given trajectory to calculate the forces for each leg. In the case of the SRS this is done by using a common model-based feedforward control approach. [1] The principle of this controller has already been explained in the chapter about the general control strategy, but for convenience the diagram is shown again in figure 7.1. The figure includes the inner loop CdP controller, but in this chapter various inner loop controllers will be used.

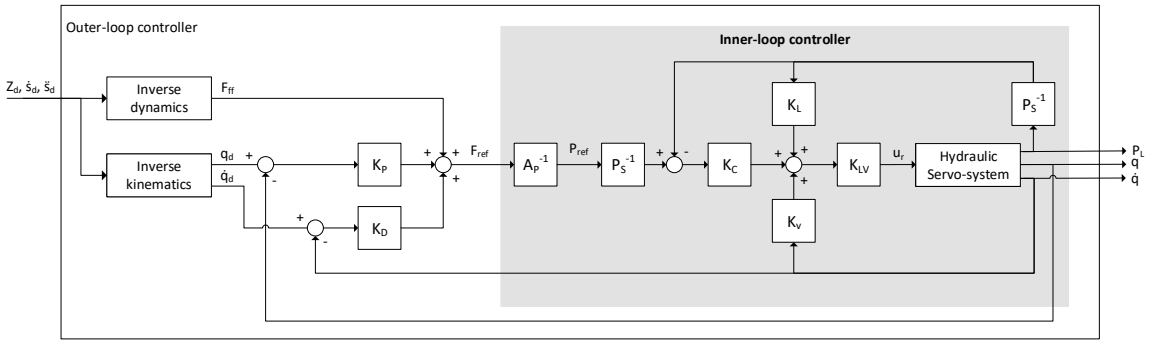

Figure 7.1: A cascaded control structure with inner loop force control and outer loop motion control

Figure 7.1 shows that a feedforward force term is calculated using the inverse dynamics of the hexapod and that the errors between the desired and measured actuator positions and velocities follow from the inverse kinematics of the platform and the measured values. The control law can also be represented mathematically as presented by equation 7.1. This preliminary thesis focuses on the inner loop controller and therefore the reader is referred to other works for specific details on the outer loop control as well as the dynamics and kinematics. [39] [17]

$$\boldsymbol{F_{ref}} = \boldsymbol{F_{ff}} + K_P(\boldsymbol{q_d} - \boldsymbol{q}) + K_D(\dot{\boldsymbol{q}}_{\boldsymbol{d}} - \dot{\boldsymbol{q}}) \tag{7.1}$$

Y. Huang has also designed an outer loop INDI controller for the SRS [19], but this is considered to be out of scope for this preliminary thesis as the focus lies on the control of the inner loop. Therefore, only the original outer-loop controller as implemented on the SRS is considered as this is the controller that will be used in simulation.

7.1. Performance comparison of inner loop controllers

A simulation is now executed using this outer loop controller in combination with the original CdP inner loop controller to serve as a baseline for the performance. The results of this simulation are given in figure 7.2. In the simulation the controller is tracking a given trajectory that can be converted to leg extensions through the inverse kinematics.

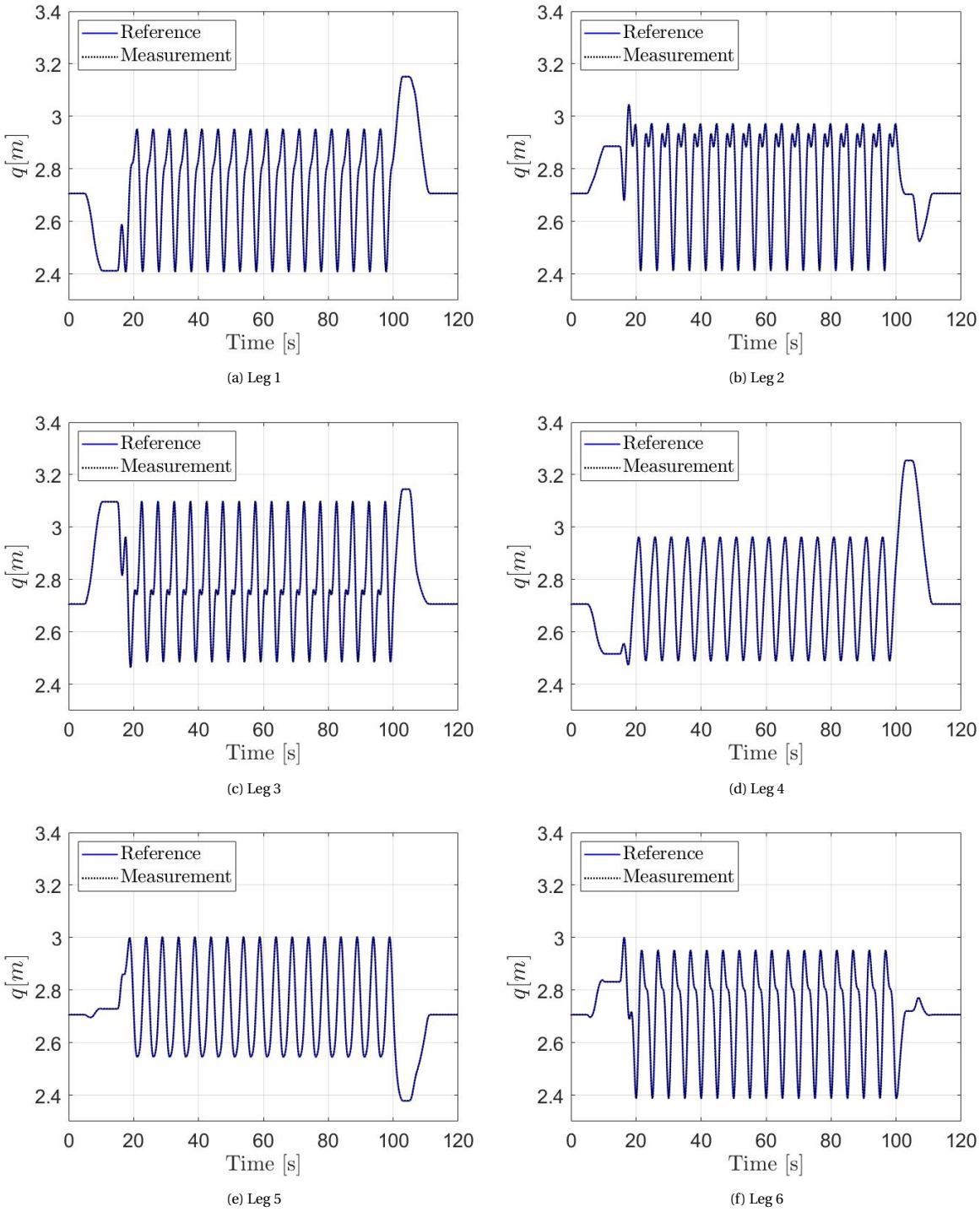

(a) Leg 1

(b) Leg 2

(c) Leg 3

(d) Leg 4

(e) Leg 5

(f) Leg 6

Figure 7.2: Outer loop tracking of the leg extensions for each of the six legs for the complete CdP controller

From the above figures it can be seen that the controller is stable and tracks the reference. It is however difficult to say anything about the performance on this scale as the reference and measurement lie close together in the plots for each of the six legs. The same reference will be used throughout this chapter for the other controllers and therefore it will only be shown once as these will not provide any further insight for any of the controllers. Therefore, the errors are plotted for the outer loop tracking and the pressure tracking for the inner loop controller. For the original controller with the CdP inner loop controller the outer loop extension errors are given by figure 7.4 and the inner loop pressure tracking is presented by 7.3.

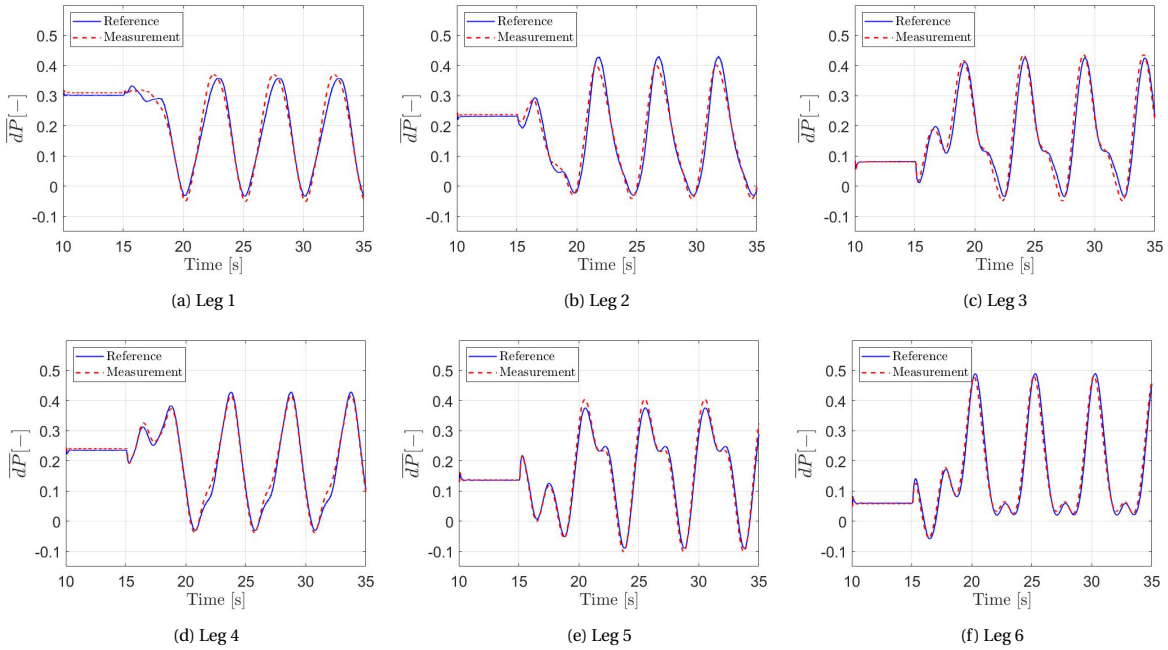

(a) Leg 1 (b) Leg 2 (c) Leg 3

(d) Leg 4 (e) Leg 5 (f) Leg 6

Figure 7.3: Inner loop tracking of the leg extensions for each of the six legs for the complete CdP controller

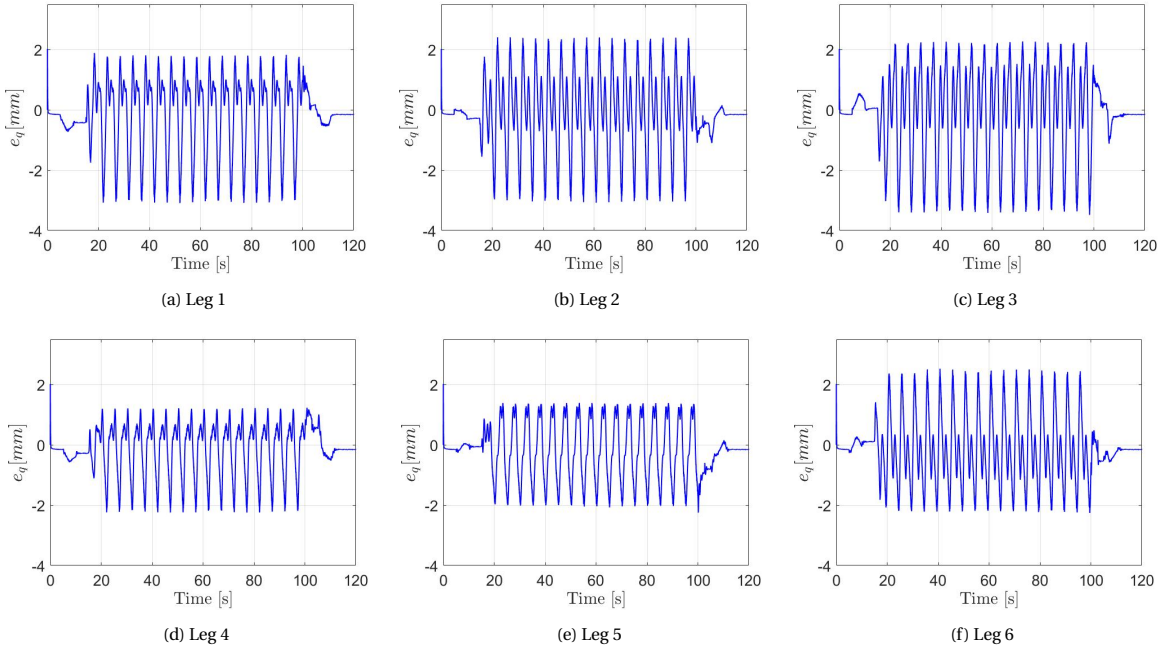

(a) Leg 1 (b) Leg 2 (c) Leg 3

(d) Leg 4 (e) Leg 5 (f) Leg 6

Figure 7.4: Outer loop tracking error of the leg extensions for each of the six legs for the complete CdP controller

Figure 7.4 shows that the maximum error in terms of extension of the legs is about 2mm for the 6 legs. Also the inner pressure tracking leaves some room for improvement as can be seen in figure 7.3, as there is still visible deviation between the reference and the measured pressure. This was to be expected from the earlier analysis for the single actuator case. It is expected that the outer loop performance will also increase when the deviation between the reference and measured pressure becomes less and therefore improvement is desirable.

The next simulation to be performed is for the baseline INDI controller. The only adjustment made to the

original INDI controller as designed by Huang [16] is to adjust the damping of the C4 and C5 filters for stability reasons. This also allows for a fair comparison between the controller with and without integral gain as the increase in damping and the decrease in frequency for the filter have a negative impact on the control performance. The results of the simulation can be observed in figures 7.5 and 7.5.

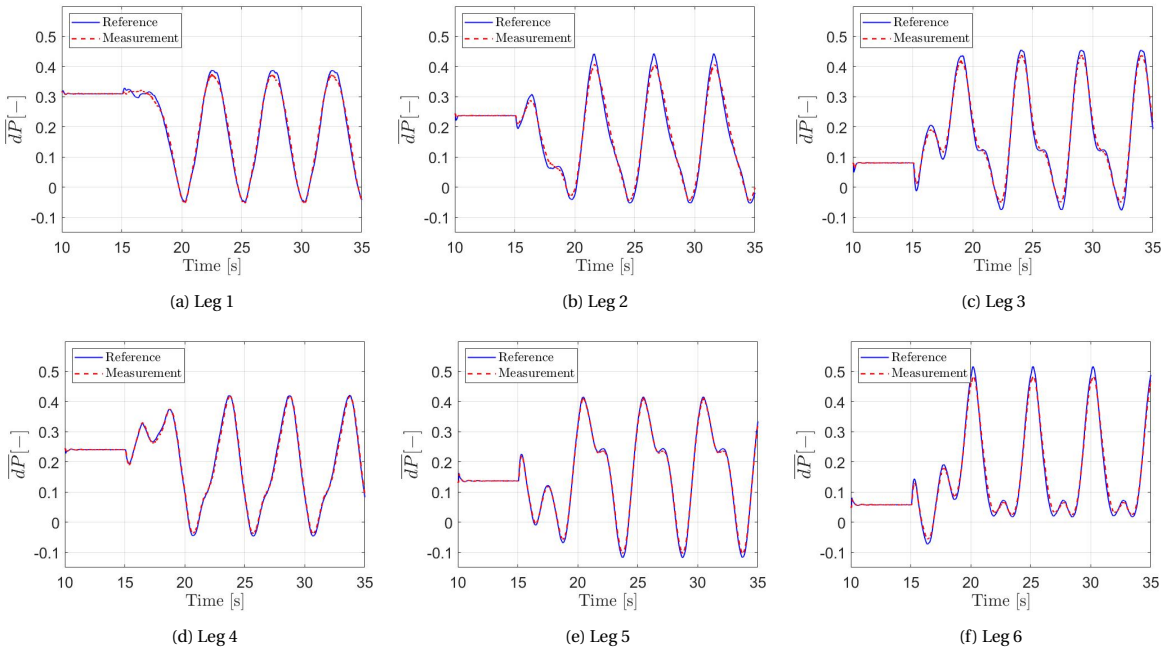

(a) Leg 1 (b) Leg 2 (c) Leg 3

(d) Leg 4 (e) Leg 5 (f) Leg 6

Figure 7.5: Outer loop tracking of the leg extensions for each of the six legs for the controller with the baseline inner INDI controller

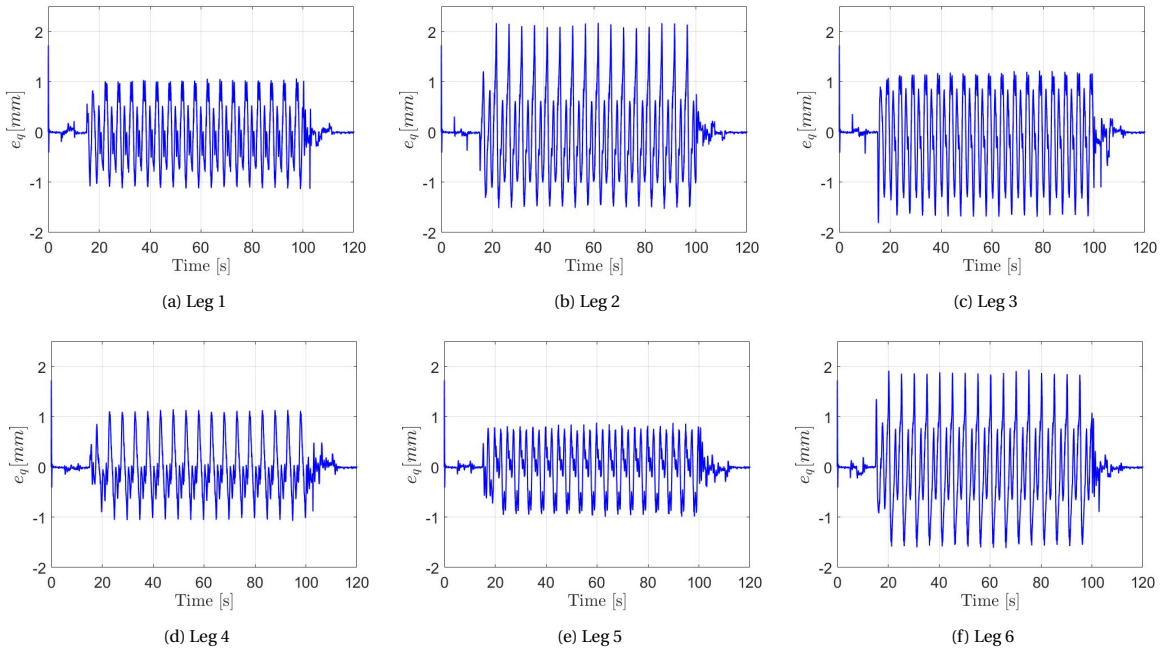

(a) Leg 1 (b) Leg 2 (c) Leg 3

(d) Leg 4 (e) Leg 5 (f) Leg 6

Figure 7.6: Outer loop tracking error of the leg extensions for each of the six legs for the controller with the baseline inner INDI controller

The baseline INDI controller does indeed outperform the CdP controller with an maximum extension error that deviates between 1-2 mm for the legs as shown by figure 7.5. This result was expected as well because

Huang [16] already found these results. The improvement of the INDI controller is also shown in simulation in the previous chapters for the single actuator case. There is however still room for improvement especially for the inner loop as can be observed in figure 7.6. Therefore, for the next simulation the controller is used that includes integral action such that figures 7.7 and 7.8 are obtained.

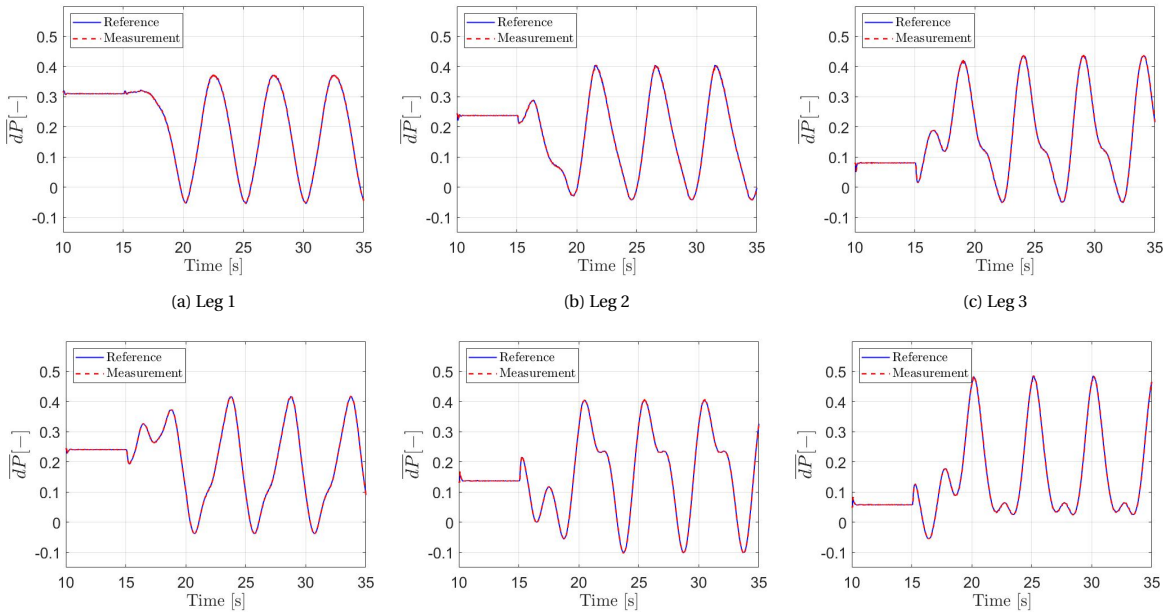

(a) Leg 1 (b) Leg 2 (c) Leg 3

(d) Leg 4 (e) Leg 5 (f) Leg 6

Figure 7.7: Outer loop tracking of the leg extensions for each of the six legs for the controller with the inner INDI controller with adaptations

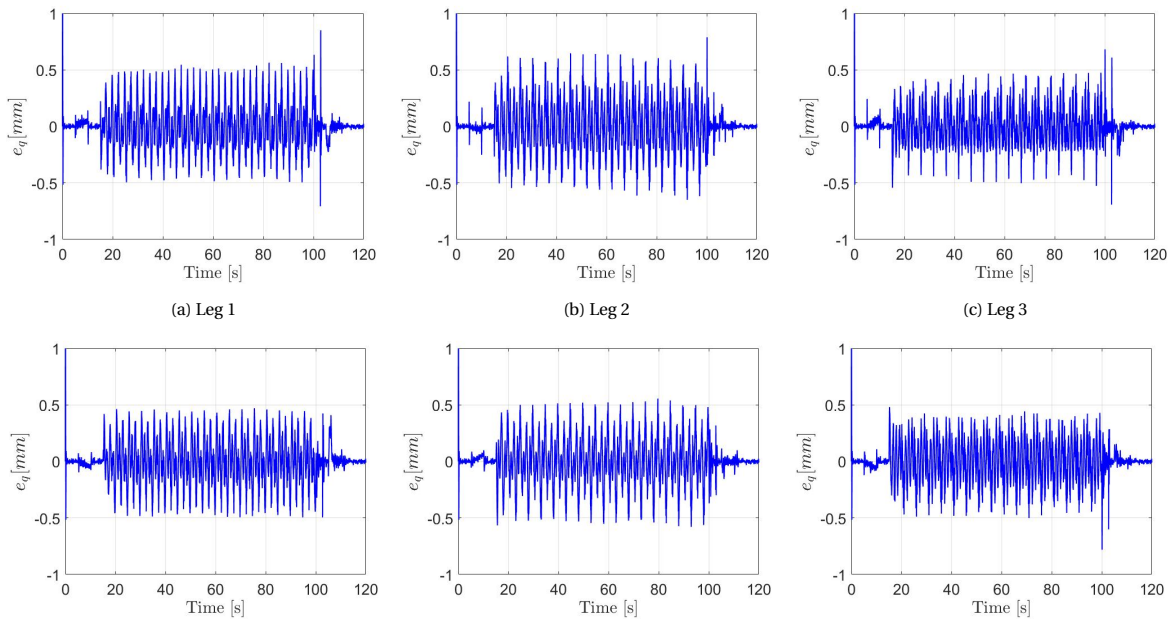

(a) Leg 1 (b) Leg 2 (c) Leg 3

(d) Leg 4 (e) Leg 5 (f) Leg 6

Figure 7.8: Outer loop tracking of the leg extensions for each of the six legs for the controller with the inner INDI controller with adaptations

The inner loop INDI controller that now includes integral action shows better performance in simulation than the controller without such action. This can be observed in terms of control error by the outer loop.

The increase in performance of the inner loop directly translates to the outer loop. This can be clearly seen in figure 7.7 where the maximum leg extension error for each leg is reduced to about 0.5mm and shows less deviation between the legs as well. The inner loop pressure tracking is also improved greatly, as shown by figure 7.8.

7.2. Saturation

To evaluate the ability of the adaptations made to deal with the problems that arise due to saturation a sinusoidal heave reference is to be tracked by the new adapted controller in simulation. The heave signal increases in amplitude over time such that the servo-valve slowly starts to saturate and the saturation and accompanying effects will therefore have increased in magnitude for each period. The tracking of the leg extension can be found in figure 7.9 with accompanying error in figure 7.10. In order to get a better understanding of the behavior occurring in the inner loop the pressure tracking is shown in figure 7.11, where the adjusted reference by the PCH is also shown.

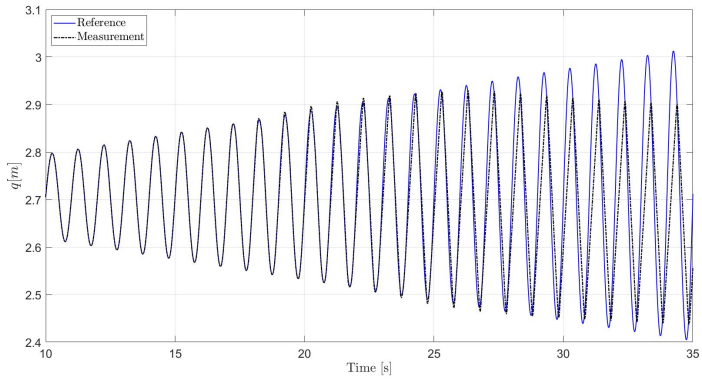

Figure 7.9: Position tracking for leg 1 of the controller with the inner loop INDI controller with adaptations for a sinusoidal reference that leads to saturation

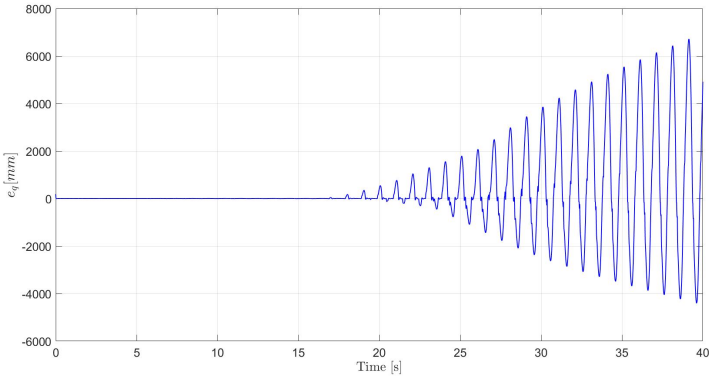

Figure 7.10: Position tracking error for leg 1 of the controller with the inner loop INDI controller with adaptations for a sinusoidal reference that leads to saturation

From the above figures it becomes clear that the error does increase during saturation which is to be expected as no additional action can be applied at this point anymore to reduce the error. The controller does however remain stable and no wind-up effects are to be found in the figures. Therefore it looks like the PCH is working properly, but to get a better idea of what is happening the inner loop tracking should be analyzed.

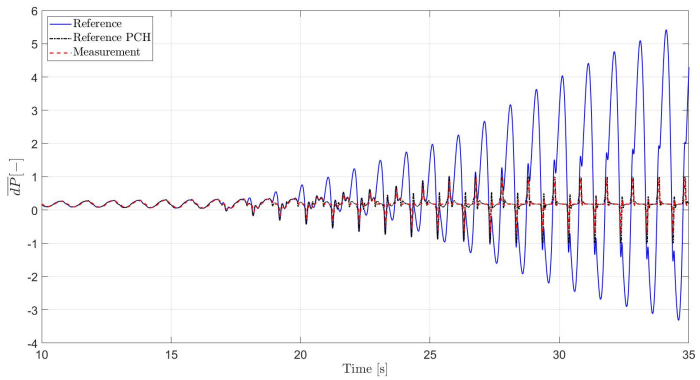

Figure 7.11: Commanded valve position for leg 1 of the controller with the inner loop INDI controller with adaptations for a sinusoidal reference that leads to saturation

The tracking of the inner loop, which is to be found in figure 7.11, shows the adjusted PCH reference which is indeed different from the original reference. The controller is also nicely following the adjusted reference and in figure 7.12 it can be seen that the input to the servo-valve remains bounded and below the value of 1 at which it starts to saturate.

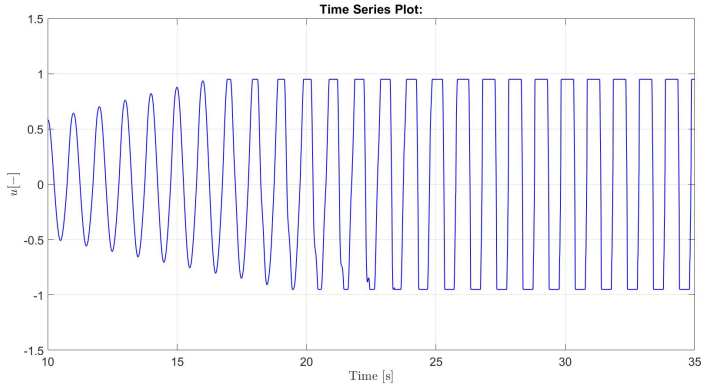

Figure 7.12: A cascaded control structure with inner loop force control and outer loop motion control

The PCH adjustment including integral gain for the inner loop linear controller is therefore also behaving as expected when applied to the full hexapod simulation case as is properly adjusts the reference to prevent the linear controller from adapting to the saturation. The next step would therefore be to test the behavior in an experiment on the simulator.

7.3. Servo-valve model based controller

As stated earlier it would be beneficial for industry to use a valve model instead of measurements for the main spool position of the servo-valve as it can be difficult to extract these measurements from the servo-valve and manipulate them such that they can be used for control. The next simulation shows the responses of the controller with a 1^{st} order model instead of measurements. The result can be found in figures 7.13, 7.14 and 7.15.

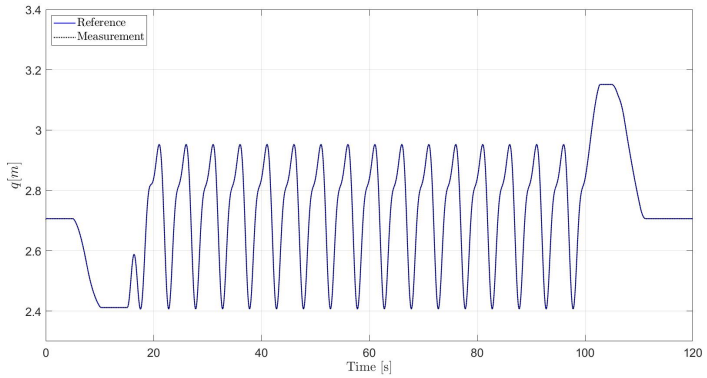

Figure 7.13: Position tracking using the controller with the inner loop INDI controller that uses a model instead of measurements for the main spool position of the servo-valve

At first glance it looks like the controller is adequately tracking the position reference considering figure 7.13. The controller remains stable and show no unexpected behavior when compared to the other responses obtained earlier. Therefore it is now interesting to zoom in and take a look at the control error as well as the inner loop tracking.

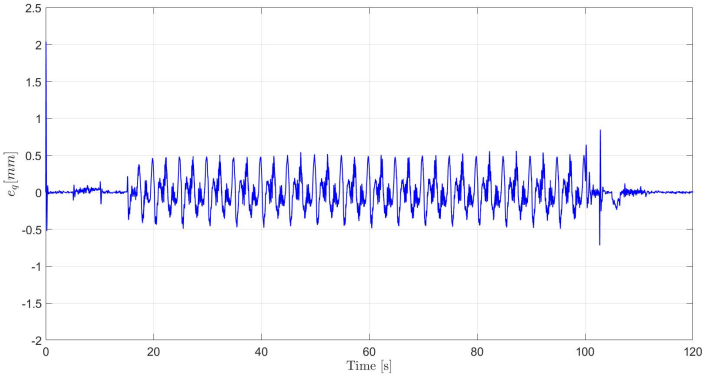

Figure 7.14: Position tracking error of the controller with the inner loop INDI controller that uses a model instead of measurements for the main spool position of the servo-valve

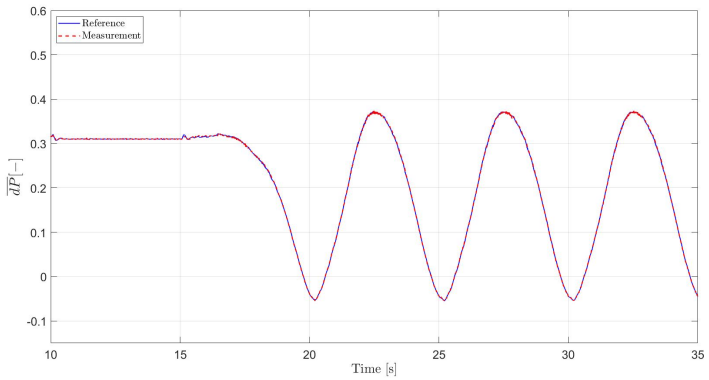

Figure 7.15: Pressure tracking using the controller with the inner loop INDI controller that uses a model instead of measurements for the main spool position of the servo-valve

Figures 7.14 and 7.15 show that there is not much difference in simulation between using the measurements and using a valve model. The outer loop control error and inner loop pressure tracking are showing similar behavior. It would therefore be interesting to check whether the simulations do align with reality. Therefore the results will have to be validated during an experiment on the SRS.

8

Discussion & conclusion

The problem statement mentioned the presence of two types of instabilities. From analysis, simulation and other literature it was found that the synchronization of the inner INDI controller loop is of importance and that the controller can become unstable when there is a time delay between the two. The design of the filters in these loops is also essential for the stability. It is however currently not known if these factors are really the reason for the instabilities, as further investigation and validation using experiments are required. It should also be noted that PCH is one of several possibilities to deal with the problems that arise due to the saturation of the servo-valve. Other integrator wind-up techniques do exist that might also tackle the problem. There is however one distinct benefit to PCH, which is that it can be applied to any linear controller used for the inner loop INDI controller and therefore the linear controller can be adjusted without having to redesign the PCH.

In this thesis the outer loop control using INDI, which had already been investigated and implemented by Y. Huang [16], is not considered. It is expected that this outer loop controller would lead to bigger performance gains for the complete SRS controller. This is however out side the scope for this work.

Furthermore it has been found that the performance of the inner loop INDI controller can be increased by adding integral gain to the linear controller in the INDI controller. The performance in terms of maximum extension error has shown to have decreased from 2mm to 0.5mm when integral action is added to the controller. For stability reasons the gain will have to be reduced from 80 to 60 and the damping will have to be increased from 0.3 to 0.707. This will reduce the inner loop control performance, but increase the overall stability of the system.

It is also found that the inner loop INDI controller without integral gain is able to handle the electro-hydraulic servo-valve saturation, but that this is not the case when integral action is added. The integral action will wind-up during saturation, which decreases the overall control performance and can lead to unexpected behavior. Pseudo Control Hedging is found to be an appropriate method to prevent the integral wind-up for the INDI controller due to promising results in simulation. The commanded input to the servo-valve by the controller stays below the saturation point and therefore prevents the controller from acting upon the saturation.

Lastly it is found that it is possible in simulation to replace the measurement of the main spool position of the servo-valve by a servo-valve model so that the measurements are not needed anymore in the INDI controller. It is also found and proven in this preliminary thesis that it is important for both the stability and performance of the controller to synchronize the inner loop feedback and incremental loops. The adaptations which were considered in this preliminary thesis are therefore all to be implemented in the INDI controller for the Simona Research Simulator so that the results found in simulation can be validated.

9

The road ahead

The next steps to be taken all relate to implementing the adaptations on the SRS. In order to do this it will first be needed to obtain a stable baseline controller. The controller has become unstable in the new setup of the SRS and therefore the reason for this instability will have to be found and dealt with. Hereafter, a detailed test plan will have to be made which is to be executed on the simulator. The test plan will contain the adaptations to be made to the controller on the SRS as well as the step-by-step approach for testing the adaptations. After the experiments the data will have to be processed such that the results can be used for comparison with the simulations. The results and conclusions drawn from the analyses are to be used for the final paper. Below the aforementioned steps are listed in another format for clarity.

- Find the reason for the instabilities of the controller in the new setup
- Create a test plan for the experiments related to the controller stability
- Create a test plan for the experiments related to the controller adaptations
- Implement the adaptations to the INDI controller in the SRS
- Execute the experiments according to the test plan
- Process the data acquired from the experiments on the SRS
- Write the paper

Bibliography

[1] H. Abdellatif and B. Heimann. Advanced model-based control of a 6-dof hexapod robot: A case study. *IEEE/ASME Transactions On Mechatronics*, 15(2):269–279, 2009.

[2] P. Acquatella, W. Falkena, E. van Kampen, and Q.P. Chu. Robust nonlinear spacecraft attitude control using incremental nonlinear dynamic inversion. In *AIAA Guidance, Navigation, and Control Conference*, page 4623, 2012.

[3] S.K. Advani. The basic research simulator programme and the industrial and aerospace community: Opportunities for cooperative research. *Delft University of Technology, Faculty of Aerospace Engineering, Report LR-662*, 1991.

[4] A. Akers and S.J. Lin. Dynamic analysis of flapper-nozzle valve. *ASME Trans. J. Dyn. Sys. Meas. Control*, 113:163–167, 1991.

[5] A.T. Azar and F.E. Serrano. Design and modeling of anti wind up pid controllers. In *Complex system modelling and control through intelligent soft computations*, pages 1–44. Springer, 2015.

[6] P.J. Campo and M. Morari. Robust control of processes subject to saturation nonlinearities. *Computers & Chemical Engineering*, 14(4-5):343–358, 1990.

[7] RR Da Costa, QP Chu, and JA Mulder. Reentry flight controller design using nonlinear dynamic inversion. *Journal of Spacecraft and Rockets*, 40(1):64–71, 2003.

[8] B. Dasgupta and T.S. Mruthyunjaya. Closed-form dynamic equations of the general stewart platform through the newton–euler approach. *Mechanism and machine theory*, 33(7):993–1012, 1998.

[9] J.C. Doyle, R.S. Smith, and D.F. Enns. Control of plants with input saturation nonlinearities. In *1987 American Control Conference*, pages 1034–1039. IEEE, 1987.

[10] L. Edalati, A.K. Sedigh, M.A. Shooredeli, and A. Moarefianpour. Adaptive fuzzy dynamic surface control of nonlinear systems with input saturation and time-varying output constraints. *Mechanical Systems and Signal Processing*, 100:311–329, 2018.

[11] E. Frazzoli. Recitation 11: Time delays, 11 2010. URL `https://ocw.mit.edu/courses/aeronautics-and-astronautics/16-30-feedback-control-systems-fall-2010/recitations/MIT16_30F10_rec11.pdf`.

[12] V.E. Gough. Contribution to discussion of papers on research in automobile stability, control and tyre performance. *Proc. of Auto Div. Inst. Mech. Eng.*, 171:392–395, 1957.

[13] G. Grimm, J. Hatfield, I. Postlethwaite, A.R. Teel, M.C. Turner, and L. Zaccarian. Antiwindup for stable linear systems with input saturation: an lmi-based synthesis. *IEEE Transactions on Automatic Control*, 48(9):1509–1525, 2003.

[14] Fabian Grondman, Gertjan Looye, Richard O Kuchar, Q Ping Chu, and Erik-Jan Van Kampen. Design and flight testing of incremental nonlinear dynamic inversion-based control laws for a passenger aircraft. In *2018 AIAA Guidance, Navigation, and Control Conference*, page 0385, 2018.

[15] J. Heintze and A.J.J. Van Der Weiden. Inner-loop design and analysis for hydraulic actuators, with an application to impedance control. *Control Engineering Practice*, 3(9):1323–1330, 1995.

[16] Y. Huang. *Incremental nonlinear control of hydraulic parallel robots: An application to the SIMONA research simulator*. PhD thesis, Delft University of Technology, 2019.

[17] Y. Huang, D. M Pool, O. Stroosma, Q.P. Chu, and M. Mulder. Modeling and simulation of hydraulic hexapod flight simulator motion systems. In *AIAA modeling and simulation technologies conference*, page 1437, 2016.

[18] Y. Huang, D. Pool, O. Stroosma, and Q.P. Chu. Incremental nonlinear dynamic inversion control for hydraulic hexapod flight simulator motion systems. *IFAC-PapersOnLine*, 50(1):4294–4299, 2017.

[19] Yi. Huang, D. Pool, O. Stroosma, and Q.P. Chu. Robust incremental nonlinear dynamic inversion controller of hexapod flight simulator motion system. In *Advances in Aerospace Guidance, Navigation and Control*, pages 87–99. Springer, 2018.

[20] E. Johnson, A. Calise, H. El-Shirbiny, and R. Eysdyk. Feedback linearization with neural network augmentation applied to x-33 attitude control. In *AIAA Guidance, Navigation, and Control Conference and Exhibit*, page 4157, 2000.

[21] E.N. Johnson and A.J. Calise. Pseudo-control hedging: A new method for adaptive control. In *Advances in navigation guidance and control technology workshop*, pages 1–2. Alabama, USA Alabama, USA, 2000.

[22] S.H. Koekebakker. *Model based control of a flight simulator motion system*. PhD thesis, Delft University of Technology, 2001.

[23] M.E. Kontz. *Haptic control of hydraulic machinery using proportional valves*. PhD thesis, Georgia Institute of Technology, 2007.

[24] A. Korobeynikov and V. Turlapov. Modeling and evaluating of the stewart platform. 1 2005.

[25] S.J. Lin and A. Akers. A dynamic model of the flapper-nozzle component of an electrohydraulic servovalve. *Journal of Dynamic Systems, Measurement, and Control*, 111(1):105–109, 1989.

[26] T. Lombaerts, G. Looye, Q.P. Chu, and J.A. Mulder. Pseudo control hedging and its application for safe flight envelope protection. In *AIAA Guidance, Navigation, and Control Conference*, page 8280, 2010.

[27] N.D. Manring and R.C. Fales. *Hydraulic control systems*. John Wiley & Sons, 2 edition, 9 2019. ISBN 1119416477.

[28] H.E Merritt. *Hydraulic control systems*. John Wiley & Sons, 1 edition, 1 1991. ISBN 0471596175.

[29] Andrew Yeh Ching Nee. *Handbook of manufacturing engineering and technology*. Springer, 2015.

[30] NPTEL. Proportional control valves, 2 2013. URL `https://nptel.ac.in/courses/112106175/Module%203/Lecture%2022.pdf`. (Accessed May 29, 2019).

[31] N.O. Pérez-Arancibia, T. Tsao, and J.S. Gibson. Saturation-induced instability and its avoidance in adaptive control of hard disk drives. *IEEE Transactions on Control Systems Technology*, 18(2):368–382, 2009.

[32] F. Pierrot, C. Reynaud, and A. Fournier. Delta: a simple and efficient parallel robot. *Robotica*, 8(2):105–109, 1990.

[33] N. Sepehri, G.A.M. Dumont, P.D. Lawrence, and F. Sassani. Cascade control of hydraulically actuated manipulators. *Robotica*, 8(3):207–216, 1990.

[34] S. Sieberling, Q.P. Chu, and J.A. Mulder. Robust flight control using incremental nonlinear dynamic inversion and angular acceleration prediction. *Journal of guidance, control, and dynamics*, 33(6):1732–1742, 2010.

[35] P. Simplício, M.D. Pavel, E. van Kampen, and Q.P. Chu. An acceleration measurements-based approach for helicopter nonlinear flight control using incremental nonlinear dynamic inversion. *Control Engineering Practice*, 21(8):1065–1077, 2013.

[36] E.J.J. Smeur, G.C.H.E. de Croon, and Q.P. Chu. Cascaded incremental nonlinear dynamic inversion for mav disturbance rejection. *Control Engineering Practice*, 73:79–90, 2018.

[37] D. Stewart. A platform with six degrees of freedom. *Proceedings of the institution of mechanical engineers*, 180(1):371–386, 1965.

[38] B. Trinkel. *Fluid power basics*. Hydraulics & Pneumatics magazine, 3 edition, 6 2007.

[39] G. van Schothorst. *Modelling of long-stroke hydraulic servo-systems for flight simulator motion control and system design*. PhD thesis, Delft University of Technology, 8 1997.

[40] T.J. Viersma. *Analysis, synthesis and design of hydraulic servosystems and pipelines*, volume 980. Elsevier Amsterdam, 1980.

[41] voskhod. Servo valves. URL `https://www.voskhod.nnov.ru/products/produktsiya-obshchepromyshlennogo-naznacheniya/9-1-servoklapany/Servovalves.pdf`. (Accessed May 29, 2019).

[42] D. Wang, R. Dolid, M. Donath, and J. Albright. Development and verification of a two-stage flow control servovalve model. *American Society of Mechanical Engineers, The Fluid Power and Systems Technology Division (Publication) FPST*, 2:121–129, 1995.

[43] W.C. Yang and W.E. Tobler. Dissipative modal approximation of fluid transmission lines using linear friction model. 1991.

[44] F. Yeaple. *Fluid power design handbook*. Fluid Power and Control. CRC Press, 3 edition, 10 1995. ISBN 9780824795627.

[45] Q. Zhang. *Basics of hydraulic systems*. CRC Press, 2 edition, 3 2008. ISBN 1138484660.

III

Appendices

A

Reference trajectories

For the paper two types of references were used. The first is a sinusoidal heave reference, which increases in amplitude over time. This sinusoidal heave reference was used to evaluate the effects of saturation. The second type is a circular motion with pitch and roll, but no heave motion. This circular motion was used to evaluate the performance of the controllers.

A.1. Circular motion

The circular motion is shown in Fig. A.1, where the X and Y coordinates are in the base frame. The XY-plane as well as the time-series of the X and Y coordinates are shown in the figure. The corresponding leg extensions for the trajectory are shown in figure A.2 for each of the six legs. This motion was used primarily to evaluate the general behavior of the controllers and their performance.

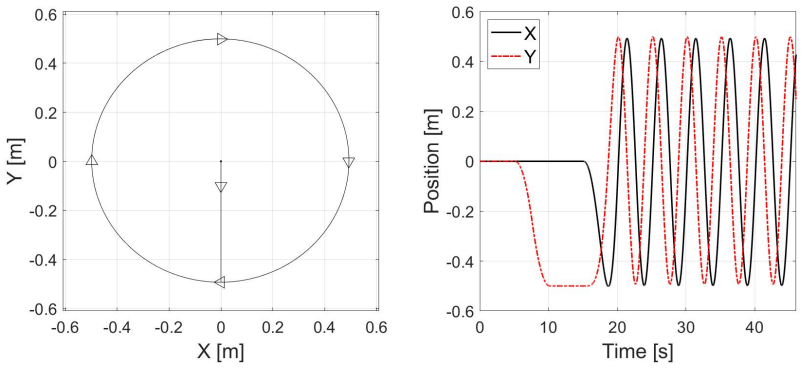

(a) XY - Plane

(b) Time-series

Figure A.1: The circular motion reference presented in the XY-plane and as time-series

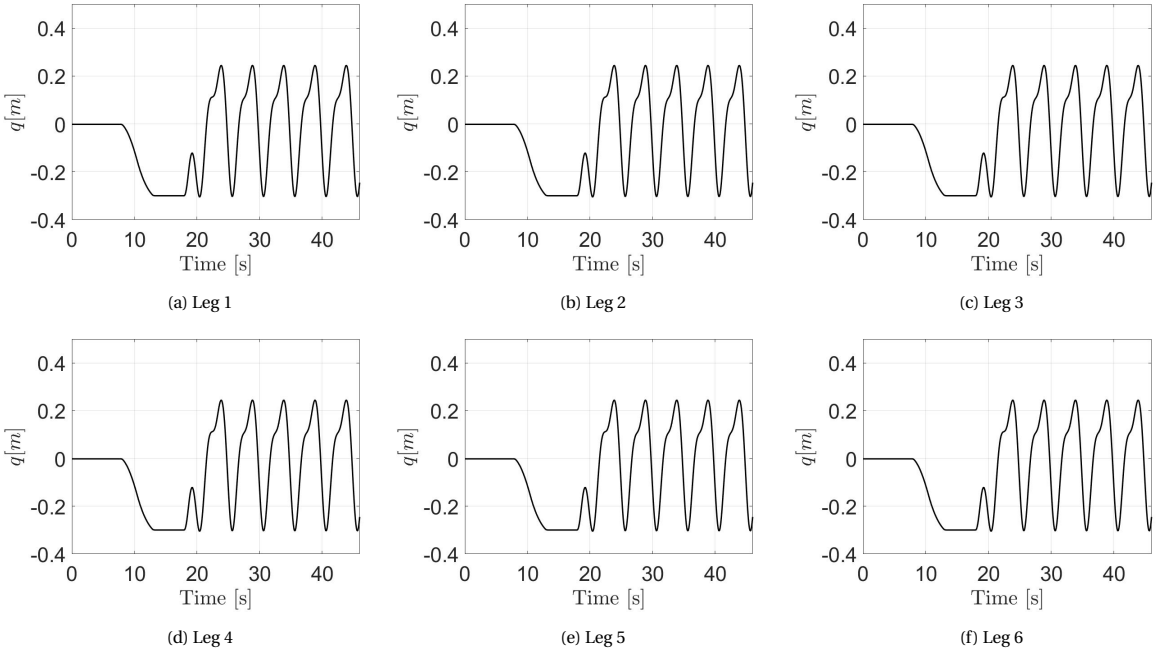

(a) Leg 1 (b) Leg 2 (c) Leg 3

(d) Leg 4 (e) Leg 5 (f) Leg 6

Figure A.2: Leg extension references for the circular motion reference

A.2. Sinusoidal heave reference

The sinusoidal references were used to evaluate the saturation. Different controllers have been evaluated. There are differences in tracking performance and therefore different amplitudes were needed to achieve saturation. The heave reference used for saturation for the controllers with inner loop CdP, original INDI and adapted INDI are shown in figures A.3, A.4 and A.5 respectively. Only 1 leg extension reference is shown as they are equal for each of the six legs due to the symmetric nature of the movement.

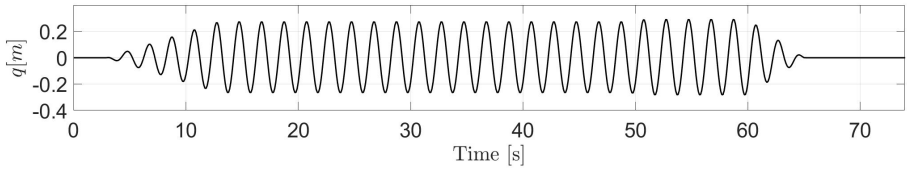

Figure A.3: The leg extensions for the sinusoidal heave motion for the controller with the inner loop CdP controller

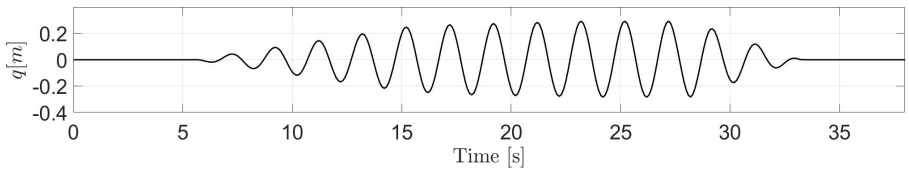

Figure A.4: The leg extensions for the sinusoidal heave motion for the controller with the original inner loop INDI controller

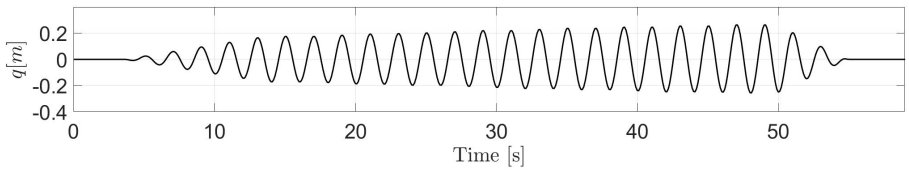

Figure A.5: The leg extensions for the sinusoidal heave motion for the controller with the adapted inner loop INDI controller

B

Experiment settings

During the experiments several controller parameters have been varied and some remained constant. The sampling frequency and most outer loop controller parameters remained constant and are shown in Tab. B.1. Some constants are used by the controllers as well and are shown in Tab. B.2. Several parameters were altered during the experiments. The files containing the log data for the experiments have been numbered and their number with corresponding file name are shown in Tab. B.3. The parameters for each experiment are shown in Tabs. B.4, B.5, B.6 and B.7. Experiments have been conducted with varying controllers and inner loop control gains. It is found that an internal setting in the data acquisition of the pressure difference measurements in the SRS had an influence on the stability and this setting was therefore also varied. When a valve-model is used instead of measurements a delay is present of which the magnitude is shown in the table as well. The order of the model was changed as well and is also provided in the tables. Finally, offsets were tuned for the measurements of the pressure and the main spool position and these offsets are given in the tables as well.

Table B.1: Outer loop controller gain settings and overall sampling frequency

KP_outer	KD_outer	KI_outer	Sampling Frequency [Hz]
800000	40000	0	5000

Symbol	**Description**	**Value**
ϕ_n	maximum valve flow	2.6E-3 $[m^3/s]$
L_{lm}	main leakage parameter	3.8187E-12 $[m^5/Ns]$
A_p	piston area	2.5E-3 $[m^2]$
P_s	supply pressure	1.6E7 $[N/m^2]$
P_t	return pressure	0 $[N/m^2]$
E	oil stiffness	1E9 $[N/m^2]$
V_m	actuator volume at middle position	1.9725E-3 $[m^3]$

Table B.2: Hydraulic servo-system parameters used by the inner loop controller

For the inner loop the control gains and the filter gains for filters C_4^* and C_5^* were varied. Filters C_2, C_3 and C_6 are given in (B.1). The structures of the C_4^* and C_5^* filters are shown in (B.1) as well, but the specific cutoff frequency and damping for each experiment are shown in Tabs. B.4, B.5, B.6 and B.7. The specific control gains for each experiment are also shown in in these tables. The complete inner loop controller is shown in (B.1) for convenience.

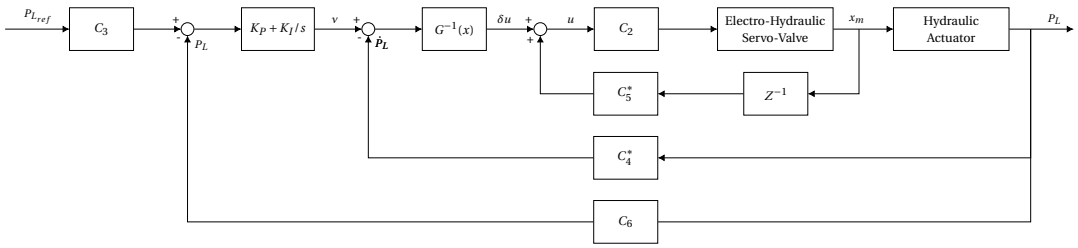

Figure B.1: Block diagram of the inner loop INDI controller including the filter design

$$C_1 = \frac{1}{\frac{1}{(2\pi 75)^2}s^2 + \frac{2\ 0.3}{2\pi 75}s + 1}, \qquad C_2 = \frac{1}{\frac{1}{2\pi 100}s + 1}, \qquad C_3 = \frac{\frac{1}{(2\pi 200)^2}s^2 + \frac{2\ 0.2}{2\pi 200}s + 1}{\frac{1}{(2\pi 400)^2}s^2 + \frac{2\ 0.2}{2\pi 400}s + 1}\frac{1}{\frac{1}{(2\pi 150)^2}s^2 + \frac{2\ 0.6}{2\pi 150}s + 1} \tag{B.1}$$

$$C_4^* = \frac{(2\pi\omega_f)^2\, s}{s^2 + 2\ \zeta_f(2\pi\omega_f) + (2\pi\omega_f)^2}, \quad C_5^* = \frac{(2\pi\omega_f)^2}{s^2 + 2\ \zeta_f(2\pi\omega_f) + (2\pi\omega_f)^2}, \quad C_6 = \frac{(2\pi 50)^2}{s^2 + 2\ 0.3(2\pi 50) + (2\pi 50)^2}$$

Table B.3: Names of the files containing the logged data of the experiments

Experiment Nr.	File name
1	2019-11-13_13-20 BaseLine Controller.mat
2	2019-11-13_13-28 BaseLine Controller - Ivan.mat
3	2019-11-13_13-45 BaseLine Controller - Ivan 02.mat
4	2019-11-13_14-46 INDI Kp 40.mat
5	2019-11-13_15-35 BaseLine Controller 2P.mat
6	2019-11-18_10-14 Simona Off.mat
7	2019-11-18_10-22 Simona Manual.mat
8	2019-11-18_10-25 Simona Neutral.mat
9	2019-11-18_10-31 Simona Sine Waves.mat
10	2019-11-18_10-35 Simona DownLock.mat
11	2019-12-03_16-37 Sampling Mode (Speed) dP.mat
12	2019-12-05_13-40 dP Sampling Mode and Filter.mat
13	2019-12-05_13-44 dP Sampling Mode and Filter dP_0 and dP_1.mat
14	2019-12-05_14-42 BaseLine Controller.mat
15	2019-12-05_14-59 INDI Controller f 15 d 1_5 Stable.mat
16	2019-12-05_15-29 INDI Controller f 15 d 0_707 Stable.mat
17	2019-12-05_15-42 INDI Controller f 35 d 0_707 Stable.mat
18	2019-12-05_15-52 INDI Controller f 35 d 0_3 Stable Little Noise.mat
19	2019-12-05_16-03 INDI Controller f 35 d 0_707 Kp 60.mat
20	2019-12-05_16-42 INDI Controller f 35 d 0_707 Kp 60 Ki 100.mat
21	2019-12-05_16-52 INDI Controller f 35 d 0_707 Kp 60 Ki 500.mat
22	2019-12-20_11-05 BaseLine Controller CdP - Sine.mat
23	2019-12-20_11-12 BaseLine Controller CdP - Ivan.mat
24	2019-12-20_11-22 Baseline Controller INDI Kp 60 Ki 0 - Sine.mat
25	2019-12-20_11-26 Baseline Controller INDI Kp 60 Ki 0 - Ivan.mat
26	2019-12-20_11-32 Controller INDI Kp 60 Ki 500 - Sine.mat
27	2019-12-20_11-35 Controller INDI Kp 60 Ki 1500 - Sine.mat
28	2019-12-20_11-37 Controller INDI Kp 60 Ki 1000 - Sine.mat
29	2019-12-20_11-42 Controller INDI Kp 60 Ki 100 - Ivan.mat
30	2019-12-20_11-46 Controller INDI Kp 60 Ki 500 - Ivan.mat
31	2019-12-20_13-10 Controller INDI Kp 60 Ki 50 - Ivan.mat
32	2019-12-20_13-14 Controller INDI Kp 60 Ki 100 - Ivan.mat
33	2019-12-20_13-18 Controller INDI Kp 60 Ki 25 - Ivan.mat
34	2019-12-20_13-22 Controller INDI Kp 60 Ki 60 - Ivan.mat
35	2019-12-20_13-25 Controller INDI Kp 60 Ki 0 - Ivan.mat
36	2019-12-20_14-15 Controller INDI Kp 60 Ki 60 ValveModel 5 - Sine.mat
37	2019-12-20_14-19 Controller INDI Kp 60 Ki 60 ValveModel 5 - Ivan.mat
38	2019-12-20_14-30 Controller INDI Kp 60 Ki 60 ValveModel 2 - Sine.mat
39	2019-12-20_14-34 Controller INDI Kp 60 Ki 60 ValveModel 2 - Ivan.mat
40	2019-12-20_14-44 Controller INDI Kp 60 Ki 60 ValveModel 1 - Sine.mat
41	2019-12-20_14-48 Controller INDI Kp 60 Ki 60 ValveModel 1 - Ivan.mat
42	2019-12-20_15-00 BaseLine Controller CdP - Sine Saturation.mat
43	2019-12-23_09-52 BaseLine Controller CdP - Sine Saturation.mat
44	2019-12-23_09-56 BaseLine Controller CdP - Sine Saturation.mat
45	2019-12-23_10-05 Controller INDI Kp 60 Ki 0 - Sine Saturation Ampl 0_29.mat
46	2019-12-23_10-11 Controller INDI Kp 60 Ki 0 - Sine Saturation Ampl 0_33.mat
47	2019-12-23_11-39 Controller INDI Kp 60 Ki 0 Kpch 0 - Sine.mat
48	2019-12-23_11-45 Controller INDI Kp 60 Ki 0 Kpch 20 - Sine.mat
49	2019-12-23_12-00 Controller INDI Kp 60 Ki 60 Kpch 20 - Sine Saturation Ampl 0_30.mat
50	2019-12-23_11-56 Controller INDI Kp 60 Ki 60 Kpch 20 - Sine.mat
51	2019-12-23_12-00 Controller INDI Kp 60 Ki 60 Kpch 20 - Sine Saturation Ampl 0_30.mat

Table B.4: Parameter settings for experiments 1-11

Test Nr.	1	2	3	4	5	6	7	8	9	10	11
Controller	CdP	CdP	CdP	INDI	CdP	CdP	CdP	CdP	CdP	CdP	CdP
Reference	Sine	Ivan	Ivan	Neutral	Sine	Neutral	Up and down	Up	Sine	Down	Neutral
K_P	-	-	-	40	-	-	-	-	-	-	-
K_I	-	-	-	0	-	-	-	-	-	-	-
ω_f	-	-	-	35	-	-	-	-	-	-	-
ζ_f	-	-	-	0.3	-	-	-	-	-	-	-
K_{PCH}	-	-	-	-	-	-	-	-	-	-	-
K_{ref}	-	-	-	-	-	-	-	-	-	-	-
valve offset leg 1	0.00074	0.00074	0.00074	0.002	0.002	0.002	0.002	0.002	0.002	0.002	0.002
valve offset leg 2	-0.0087	-0.0087	-0.0087	-0.001	-0.001	-0.001	-0.001	-0.001	-0.001	-0.001	-0.001
valve offset leg 3	0.00966	0.00966	0.00966	0.0015	0.0015	0.0015	0.0015	0.0015	0.0015	0.0015	0.0015
valve offset leg 4	0.00466	0.00466	0.00466	-0.001	-0.001	-0.001	-0.001	-0.001	-0.001	-0.001	-0.001
valve offset leg 5	0.00179	0.00179	0.00179	-0.003	-0.003	-0.003	-0.003	-0.003	-0.003	-0.003	-0.003
valve offset leg 6	0.0047	0.0047	0.0047	0.0047	0.0047	0.0047	0.0047	0.0047	0.0047	0.0047	0.0047
pressure offset leg 1	0	0	0	0	0	0	0	0	0	0	0
pressure offset leg 2	0	0	0	0	0	0	0	0	0	0	0
pressure offset leg 3	0	0	0	0	0	0	0	0	0	0	0
pressure offset leg 4	0	0	0	0	0	0	0	0	0	0	0
pressure offset leg 5	0	0	0	0	0	0	0	0	0	0	0
pressure offset leg 6	0	0	0	0	0	0	0	0	0	0	0
measurements / model	-	-	-	meas	-	-	-	-	-	-	-
valve model order	-	-	-	-	-	-	-	-	-	-	-
valve model delay	-	-	-	-	-	-	-	-	-	-	-
Pressure mode	Accuracy	Accuracy	Accuracy	Accuracy	Accuracy	Accuracy	Accuracy	Accuracy	Accuracy	Accuracy	Both

Table B.5: Parameter settings for experiments 12-21

Test Nr.	12	13	14	15	16	17	18	19	20	21
Controller	CdP	CdP	CdP	INDI	INDI	INDI	INDI	INDI	INDI	INDI
Reference	Neutral	Neutral	Sine	Sine	Sine	Sine	Sine	Sine	Sine	Sine
K_P	-	-	-	40	40	40	40	60	60	60
K_I	-	-	-	0	0	0	0	0	100	500
ω_f	-	-	-	15	15	35	35	35	35	35
ζ_f	-	-	-	1.5	0.707	0.707	0.3	0.707	0.707	0.707
K_{PCH}	-	-	-	-	-	-	-	-	-	-
K_{ref}	-	-	-	-	-	-	-	-	-	-
valve offset leg 1	0.002	0.002	0.002	0.002	0.002	0.002	0.002	0.002	0.002	0.002
valve offset leg 2	-0.001	-0.001	-0.001	-0.001	-0.001	-0.001	-0.001	-0.001	-0.001	-0.001
valve offset leg 3	0.0015	0.0015	0.0015	0.0015	0.0015	0.0015	0.0015	0.0015	0.0015	0.0015
valve offset leg 4	-0.001	-0.001	-0.001	-0.001	-0.001	-0.001	-0.001	-0.001	-0.001	-0.001
valve offset leg 5	-0.003	-0.003	-0.003	-0.003	-0.003	-0.003	-0.003	-0.003	-0.003	-0.003
valve offset leg 6	0.0047	0.0047	0.0047	0.0047	0.0047	0.0047	0.0047	0.0047	0.0047	0.0047
pressure offset leg 1	0	0	0	0	0	0	0	0	0	0
pressure offset leg 2	0	0	0	0	0	0	0	0	0	0
pressure offset leg 3	0	0	0	0	0	0	0	0	0	0
pressure offset leg 4	0	0	0	0	0	0	0	0	0	0
pressure offset leg 5	0	0	0	0	0	0	0	0	0	0
pressure offset leg 6	0	0	0	0	0	0	0	0	0	0
measurements / model	-	-	-	meas	meas	meas	meas	meas	meas	meas
valve model order	-	-	-	-	-	-	-	-	-	-
valve model delay	-	-	-	-	-	-	-	-	-	-
Pressure mode	Both	Both	Speed	Speed	Speed	Speed	Speed	Speed	Speed	Speed

Table B.6: Parameter settings for experiments 22-35

Test Nr.	22	23	24	25	26	27	28	29	30	31	32	33	34	**35**
Controller	CdP	CdP	INDI	INDI	INDI	INDI	INDI	INDI	INDI	INDI	INDI	INDI	INDI	INDI
Reference	Sine	Ivan	Sine	Ivan	Sine	Sine	Sine	Ivan	Ivan	Ivan	Sine	Ivan	Ivan	Ivan
K_P	-	-	60	60	60	60	60	60	60	60	60	60	60	60
K_I	-	-	0	0	500	1500	1000	100	500	50	100	25	60	0
ω_f	-	-	35	35	35	35	35	35	35	35	35	35	35	35
ζ_f	-	-	0.707	0.707	0.707	0.707	0.707	0.707	0.707	0.707	0.707	0.707	0.707	0.707
K_{PCH}	-	-	-	-	-	-	-	-	-	-	-	-	-	-
K_{ref}	-	-	-	-	-	-	-	-	-	-	-	-	-	-
valve offset leg 1	0.002	0.002	0.002	0.002	0.002	0.002	0.002	0.002	0.002	0.002	0.002	0.002	0.002	0.002
valve offset leg 2	-0.001	-0.001	-0.001	-0.001	-0.001	-0.001	-0.001	-0.001	-0.001	-0.001	-0.001	-0.001	-0.001	-0.001
valve offset leg 3	0.0015	0.0015	0.0015	0.0015	0.0015	0.0015	0.0015	0.0015	0.0015	0.0015	0.0015	0.0015	0.0015	0.0015
valve offset leg 4	-0.001	-0.001	-0.001	-0.001	-0.001	-0.001	-0.001	-0.001	-0.001	-0.001	-0.001	-0.001	-0.001	-0.001
valve offset leg 5	-0.003	-0.003	-0.003	-0.003	-0.003	-0.003	-0.003	-0.003	-0.003	-0.003	-0.003	-0.003	-0.003	-0.003
valve offset leg 6	0.0047	0.0047	0.0047	0.0047	0.0047	0.0047	0.0047	0.0047	0.0047	0.0047	0.0047	0.0047	0.0047	0.0047
pressure offset leg 1	-0.9	-0.9	-0.9	-0.9	-0.9	-0.9	-0.9	-0.9	-0.9	-0.9	-0.9	-0.9	-0.9	-0.9
pressure offset leg 2	-1.95	-1.95	-1.95	-1.95	-1.95	-1.95	-1.95	-1.95	-1.95	-1.95	-1.95	-1.95	-1.95	-1.95
pressure offset leg 3	-3.6	-3.6	-3.6	-3.6	-3.6	-3.6	-3.6	-3.6	-3.6	-3.6	-3.6	-3.6	-3.6	-3.6
pressure offset leg 4	0.65	0.65	0.65	0.65	0.65	0.65	0.65	0.65	0.65	0.65	0.65	0.65	0.65	0.65
pressure offset leg 5	1.9	1.9	1.9	1.9	1.9	1.9	1.9	1.9	1.9	1.9	1.9	1.9	1.9	1.9
pressure offset leg 6	1.9	1.9	1.9	1.9	1.9	1.9	1.9	1.9	1.9	1.9	1.9	1.9	1.9	1.9
measurements / model	meas	meas	meas	meas	meas	meas	meas	meas	meas	meas	meas	meas	meas	meas
valve model order	-	-	-	-	-	-	-	-	-	-	-	-	-	-
valve model delay	-	-	-	-	-	-	-	-	-	-	-	-	-	-
Pressure mode	Speed	Speed	Speed	Speed	Speed	Speed	Speed	Speed	Speed	Speed	Speed	Speed	Speed	Speed

Table B.7: Parameter settings for experiments 36-51

Test Nr.	36	37	38	39	40	41	42	43	44	45	46	47	48	49	50	**51**
Controller	INDI	INDI	INDI	INDI	INDI	INDI	CdP	CdP	CdP	INDI	INDI	INDI	INDI	INDI	INDI	INDI
Reference	Sine	Ivan	Sine	Ivan	Sine	Ivan	Sat	Sat	Sat	Sat	Sat	Sine	Sine	Sat	Sine	Sat
K_P	60	60	60	60	60	60	-	-	-	60	60	60	60	60	60	60
K_I	60	60	60	60	60	60	-	-	-	0	0	0	0	60	60	60
ω_f	35	35	35	35	35	35	-	-	-	35	35	35	35	35	35	35
ζ_f	0.707	0.707	0.707	0.707	0.707	0.707	-	-	-	0.707	0.707	0.707	0.707	0.707	0.707	0.707
K_{PCH}	-	-	-	-	-	-	-	-	-	-	-	0	20	20	20	20
K_{ref}	-	-	-	-	-	-	-	-	-	-	-	500	500	500	500	500
valve offset leg 1	0.002	0.002	0.002	0.002	0.002	0.002	0.002	0.002	0.002	0.002	0.002	0.002	0.002	0.002	0.002	0.002
valve offset leg 2	-0.001	-0.001	-0.001	-0.001	-0.001	-0.001	-0.001	-0.001	-0.001	-0.001	-0.001	-0.001	-0.001	-0.001	-0.001	-0.001
valve offset leg 3	0.0015	0.0015	0.0015	0.0015	0.0015	0.0015	0.0015	0.0015	0.0015	0.0015	0.0015	0.0015	0.0015	0.0015	0.0015	0.0015
valve offset leg 4	-0.001	-0.001	-0.001	-0.001	-0.001	-0.001	-0.001	-0.001	-0.001	-0.001	-0.001	-0.001	-0.001	-0.001	-0.001	-0.001
valve offset leg 5	-0.003	-0.003	-0.003	-0.003	-0.003	-0.003	-0.003	-0.003	-0.003	-0.003	-0.003	-0.003	-0.003	-0.003	-0.003	-0.003
valve offset leg 6	0.0047	0.0047	0.0047	0.0047	0.0047	0.0047	0.0047	0.0047	0.0047	0.0047	0.0047	0.0047	0.0047	0.0047	0.0047	0.0047
pressure offset leg 1	-0.9	-0.9	-0.9	-0.9	-0.9	-0.9	-0.9	-0.9	-0.9	-0.9	-0.9	-0.9	-0.9	-0.9	-0.9	-0.9
pressure offset leg 2	-1.95	-1.95	-1.95	-1.95	-1.95	-1.95	-1.95	-2.05	-2.05	-2.05	-2.05	-2.05	-2.05	-2.05	-2.05	-2.05
pressure offset leg 3	-3.6	-3.6	-3.6	-3.6	-3.6	-3.6	-3.6	-3.3	-3.3	-3.3	-3.3	-3.3	-3.3	-3.3	-3.3	-3.3
pressure offset leg 4	0.65	0.65	0.65	0.65	0.65	0.65	0.65	0.5	0.5	0.5	0.5	0.5	0.5	0.5	0.5	0.5
pressure offset leg 5	1.9	1.9	1.9	1.9	1.9	1.9	1.9	1.9	1.9	1.9	1.9	1.9	1.9	1.9	1.9	1.9
pressure offset leg 6	1.9	1.9	1.9	1.9	1.9	1.9	1.9	1.9	1.9	1.9	1.9	1.9	1.9	1.9	1.9	1.9
measurements / model	model	model	model	model	model	model	-	-	-	meas	meas	meas	meas	meas	meas	meas
valve model order	5	5	2	2	1	1	-	-	-	-	-	-	-	-	-	-
valve model delay	2	2	2	2	2	2	-	-	-	-	-	-	-	-	-	-
Pressure mode	Speed	Speed	Speed	Speed	Speed	Speed	-	-	-	Speed	Speed	Speed	Speed	Speed	Speed	Speed

C

Responses of the adapted INDI controller

This appendix shows the responses of the adapted INDI controller including integral action ($K_I = 60$) and the PCH implementation to the circular motion reference for each of the six legs. The adaptation to use a servo-valve model instead of measurements is implemented, but not active. Therefore, the servo-valve measurements are still used for the inner linearization loop of the inner loop controller. The outer loop leg extension tracking and accompanying tracking errors are shown in Figs. C.1 and C.2 respectively. The inner loop normalized pressure difference tracking and accompanying tracking errors are shown in Figs. C.3 and C.4 respectively.

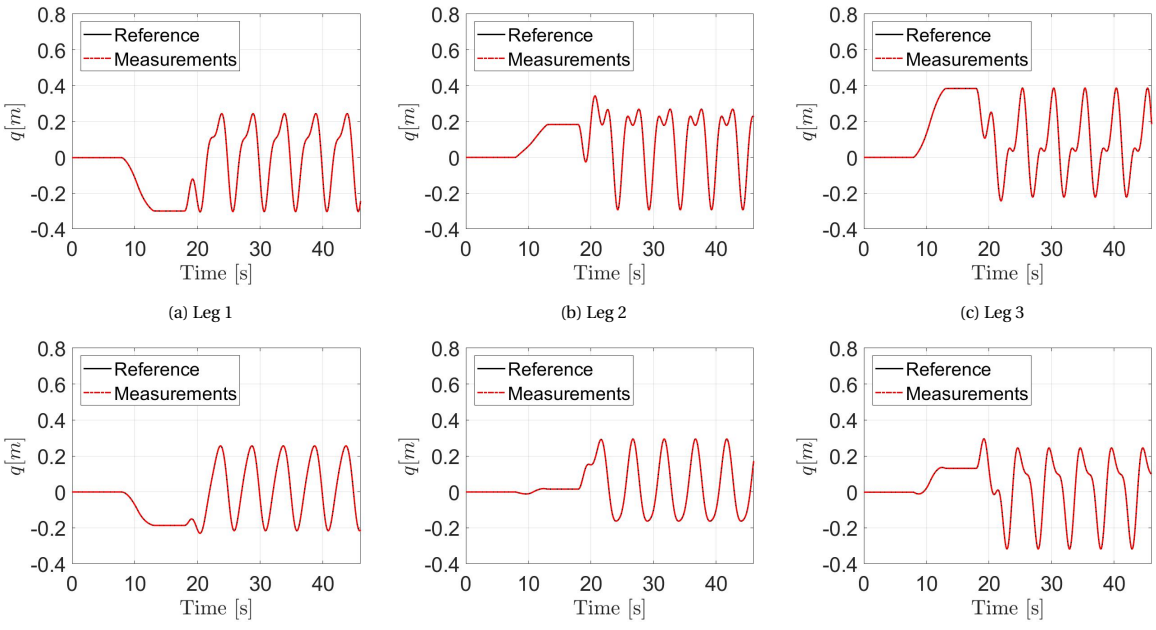

(a) Leg 1 (b) Leg 2 (c) Leg 3

(d) Leg 4 (e) Leg 5 (f) Leg 6

Figure C.1: Outer loop tracking of the leg extensions for each of the six legs for the controller with the adapted inner loop INDI controller

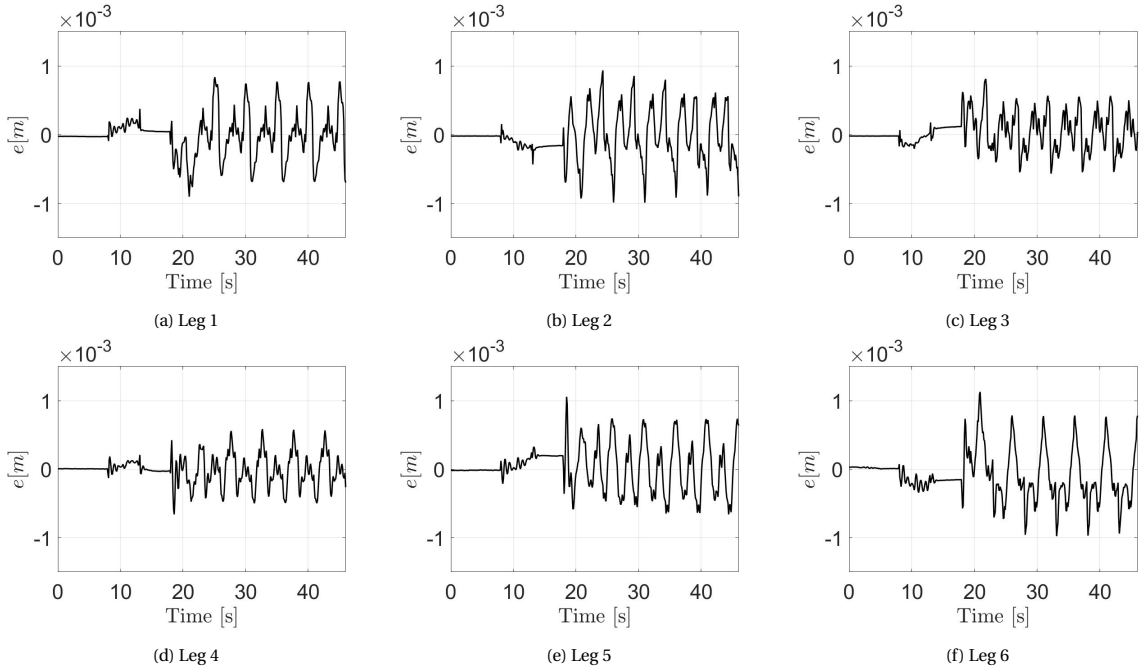

(a) Leg 1 (b) Leg 2 (c) Leg 3

(d) Leg 4 (e) Leg 5 (f) Leg 6

Figure C.2: Outer loop leg extension tracking errors for each of the six legs for the controller with the adapted inner loop INDI controller

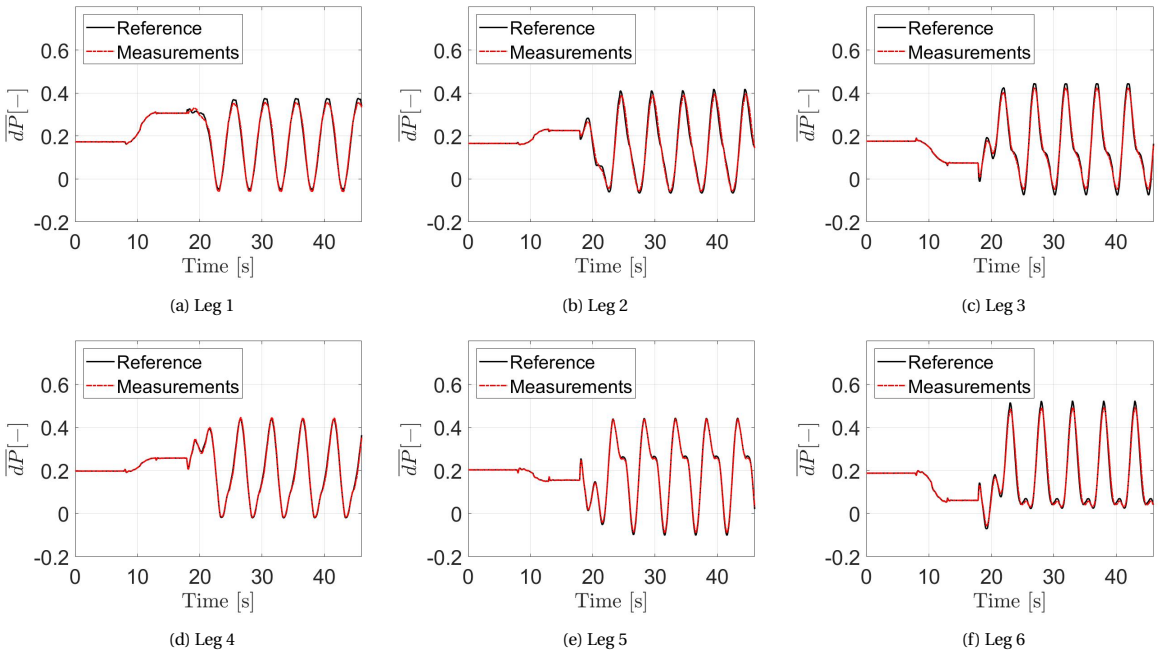

(a) Leg 1 (b) Leg 2 (c) Leg 3

(d) Leg 4 (e) Leg 5 (f) Leg 6

Figure C.3: Inner loop tracking of the leg pressures for each of the six legs for the controller with the adapted inner loop INDI controller

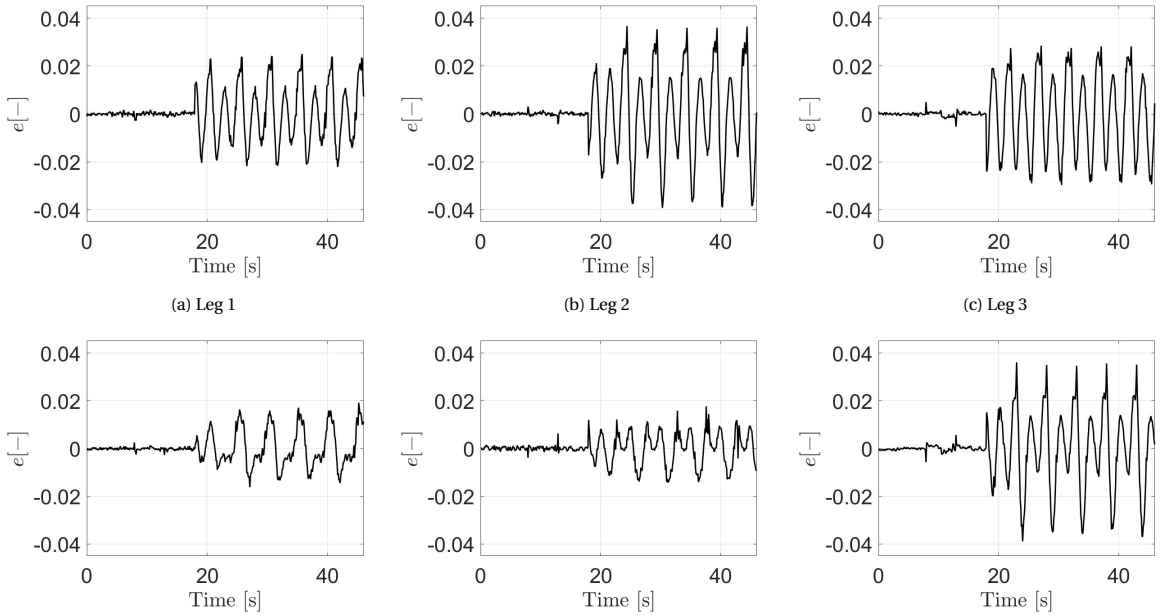

(a) Leg 1 (b) Leg 2 (c) Leg 3

(d) Leg 4 (e) Leg 5 (f) Leg 6

Figure C.4: Inner loop leg pressure tracking errors for each of the six legs for the controller with the adapted inner loop INDI controller

D

Comparison to baseline controllers

This appendix will treat the tracking errors of the original CdP, original INDI and adapted INDI controller for the circular motion reference to better understand the differences in performance between them. The maximum absolute error, Mean Absolute Error (MAE) and the Root Mean Square Error (RMSE) are considered. The tracking errors in these metric are shown for the inner loop and the outer loop controllers in figure D.1. The errors are considered for all six legs.

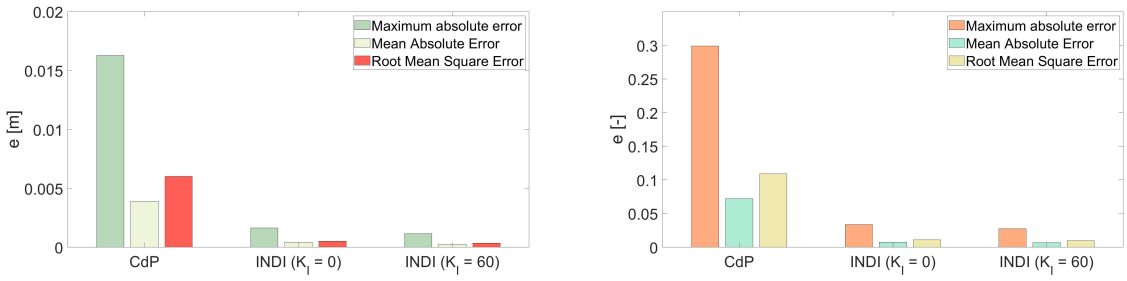

(a) Outer loop leg extension tracking errors

(b) Inner loop normalized pressure difference tracking errors

Figure D.1: Controller errors for the inner and outer loop in various metrics for all legs

The biggest difference for both the inner loop and outer loop controllers is to be found between the CdP and both INDI controllers. The inner loop CdP controller has the largest maximum absolute error of 16.28 mm and the inner loop INDI controllers lie closer together with 1.636 mm and 1.154 mm for the original and adapted inner loop INDI controller respectively. It should however be noted that $K_I = 60$ as this resulted in the best outer loop performance. Better inner loop tracking, which is obtained for larger K_I, might result in better outer loop tracking as well for other outer loop controllers such as an outer loop INDI controller.

The tracking performance for each leg for both the inner and outer loop controllers is shown in figures D.2 to D.19, which can be used to get a better understanding of the performance of each individual leg. The tracking errors for each of the six legs as well as the maximum absolute error, Mean Absolute Error (MAE) and the Root Mean Square Error (RMSE) are shown for each leg. It can be observed in these figures that there are significant differences in tracking performance between the legs. This can be due to factors such as deviations in the offset tunings and phenomena which were not modeled. Further investigation into this topic is required to increase the overall control performance of the whole system.

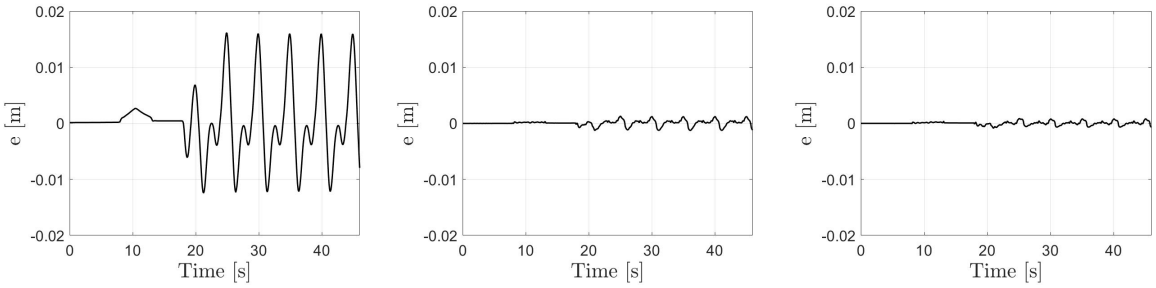

(a) CdP controller (b) Original INDI controller (c) New INDI controller

Figure D.2: Outer loop leg extension tracking errors for different controllers for leg 1

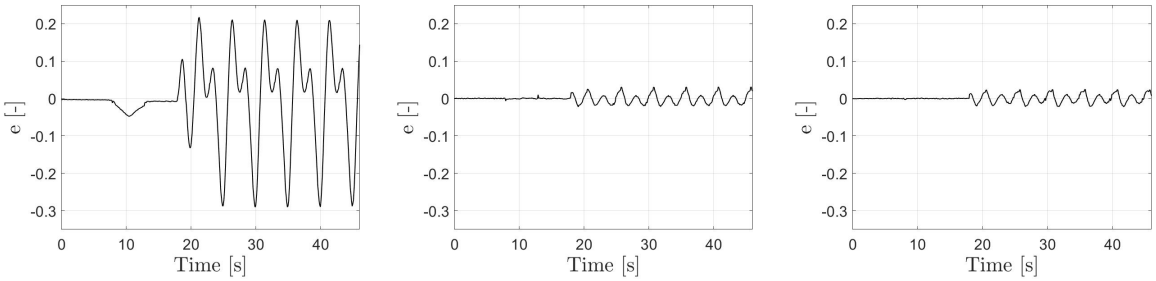

(a) CdP controller (b) Original INDI controller (c) New INDI controller

Figure D.3: Inner loop normalized pressure difference tracking errors for different controllers for leg 1

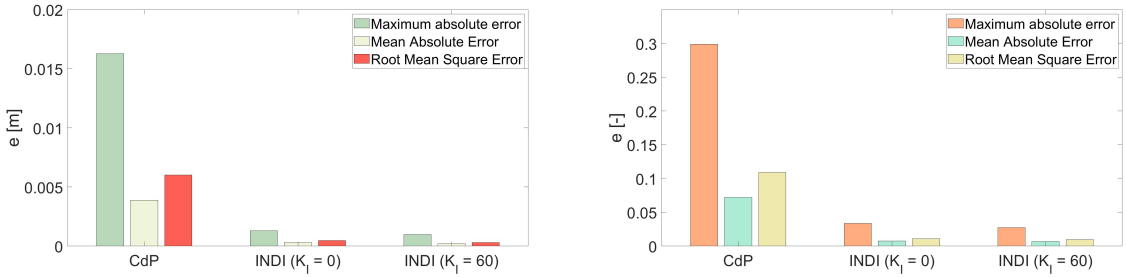

(a) Outer loop leg extension tracking errors (b) Inner loop normalized pressure difference tracking errors

Figure D.4: Controller errors for the inner and outer loop in various metrics for leg 1

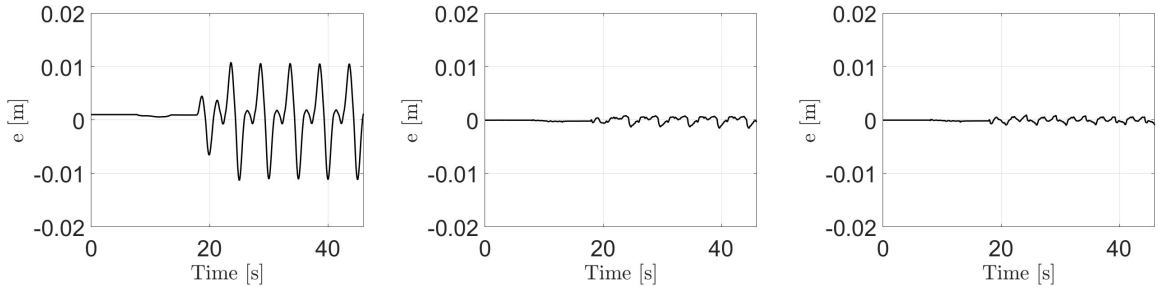

(a) CdP controller (b) Original INDI controller (c) New INDI controller

Figure D.5: Outer loop leg extension tracking errors for different controllers for leg 2

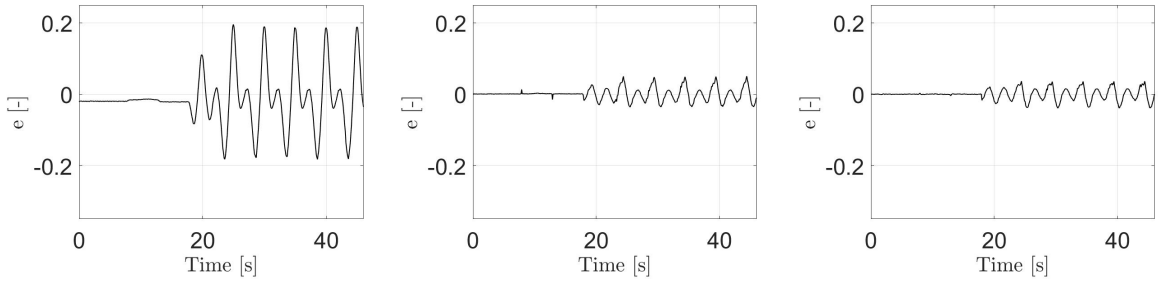

(a) CdP controller (b) Original INDI controller (c) New INDI controller

Figure D.6: Inner loop normalized pressure difference tracking errors for different controllers for leg 2

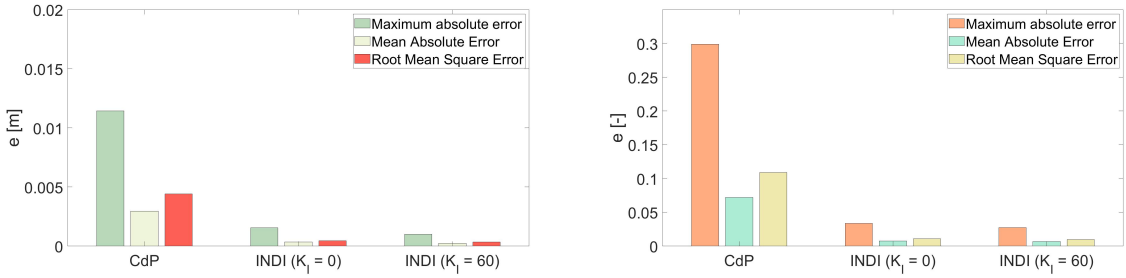

(a) Outer loop leg extension tracking errors (b) Inner loop normalized pressure difference tracking errors

Figure D.7: Controller errors for the inner and outer loop in various metrics for leg 2

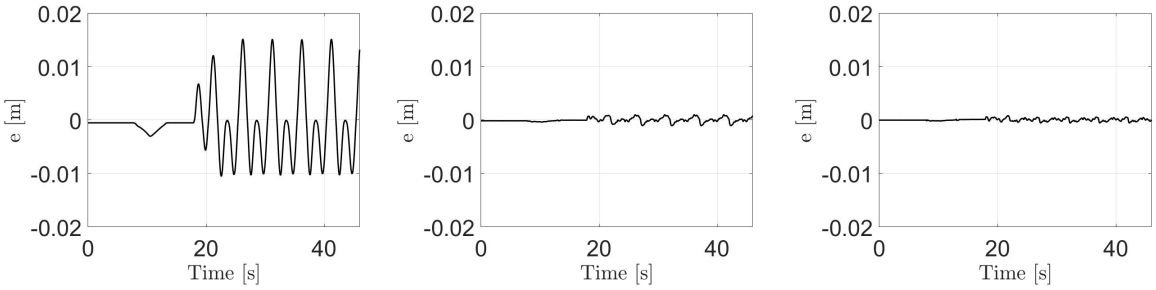

(a) CdP controller (b) Original INDI controller (c) New INDI controller

Figure D.8: Outer loop leg extension tracking errors for different controllers for leg 3

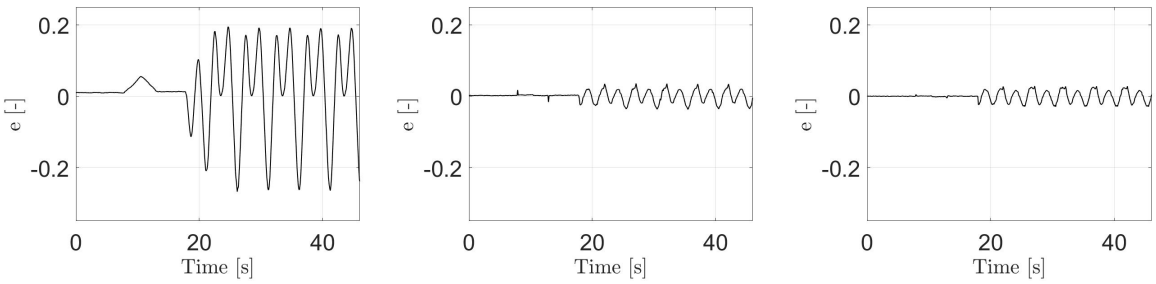

(a) CdP controller (b) Original INDI controller (c) New INDI controller

Figure D.9: Inner loop normalized pressure difference tracking errors for different controllers for leg 3

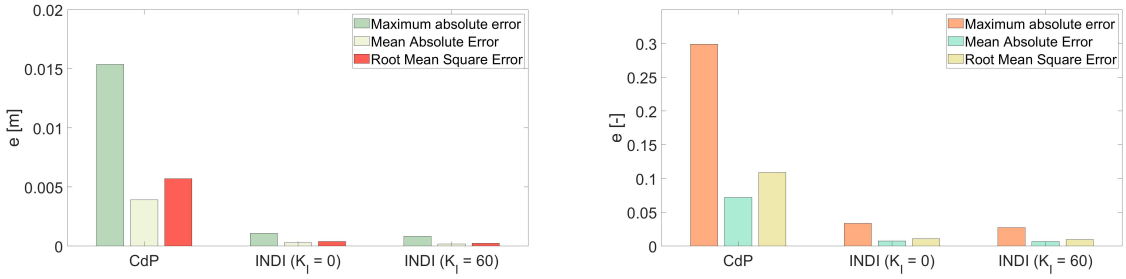

(a) Outer loop leg extension tracking errors (b) Inner loop normalized pressure difference tracking errors

Figure D.10: Controller errors for the inner and outer loop in various metrics for leg 3

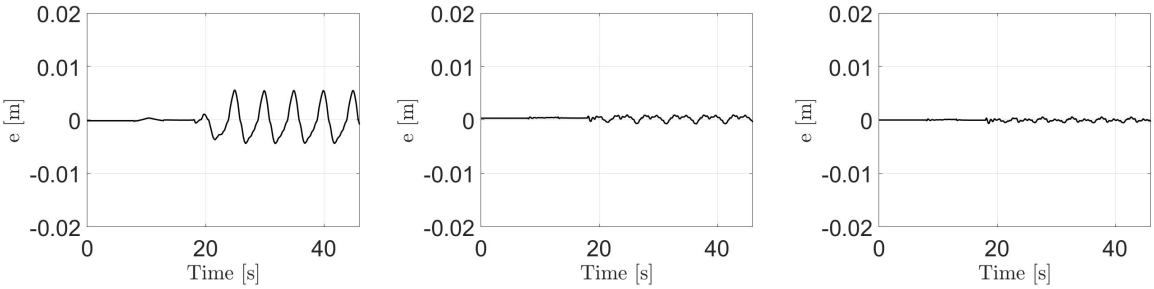

(a) CdP controller (b) Original INDI controller (c) New INDI controller

Figure D.11: Outer loop leg extension tracking errors for different controllers for leg 4

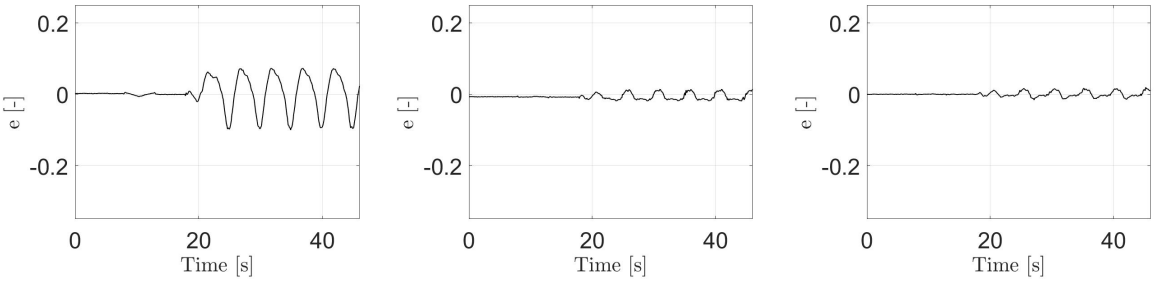

(a) CdP controller (b) Original INDI controller (c) New INDI controller

Figure D.12: Inner loop normalized pressure difference tracking errors for different controllers for leg 4

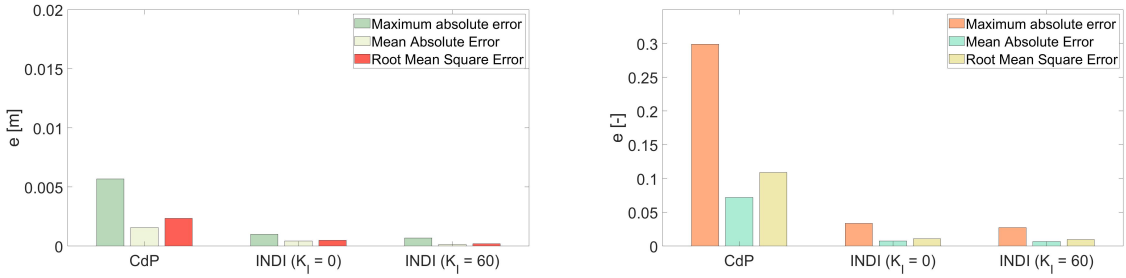

(a) Outer loop leg extension tracking errors (b) Inner loop normalized pressure difference tracking errors

Figure D.13: Controller errors for the inner and outer loop in various metrics for leg 4

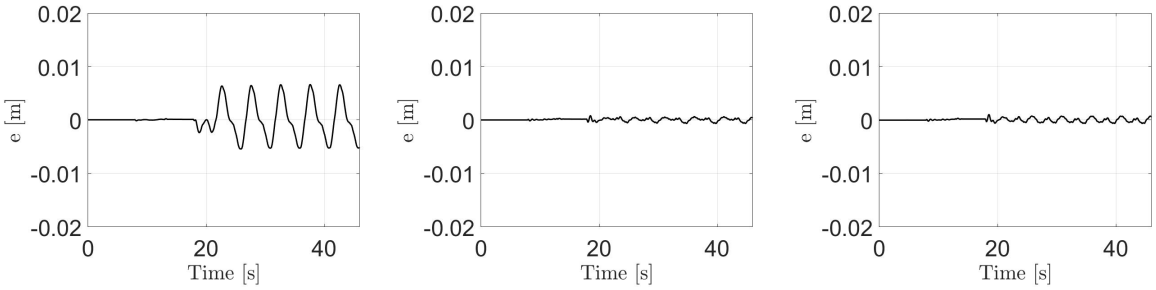

(a) CdP controller (b) Original INDI controller (c) New INDI controller

Figure D.14: Outer loop leg extension tracking errors for different controllers for leg 5

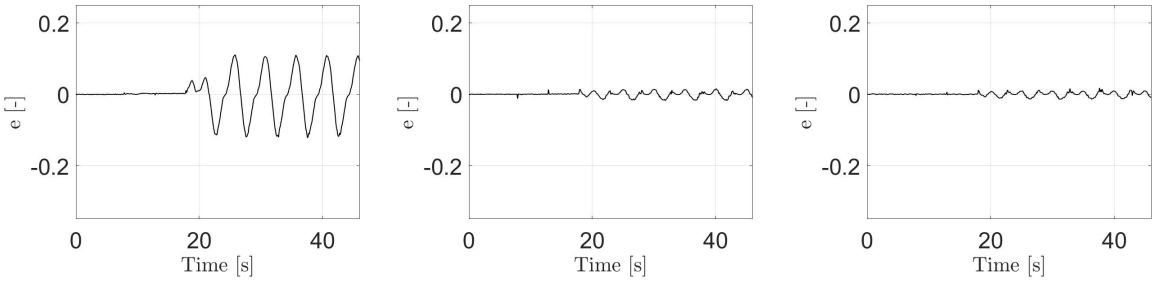

(a) CdP controller (b) Original INDI controller (c) New INDI controller

Figure D.15: Inner loop normalized pressure difference tracking errors for different controllers for leg 5

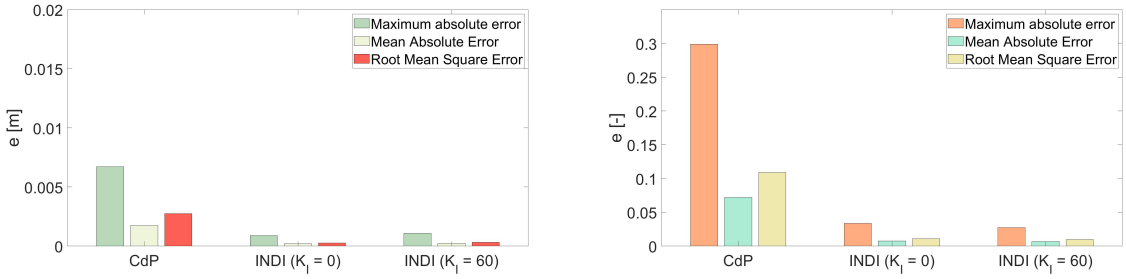

(a) Outer loop leg extension tracking errors (b) Inner loop normalized pressure difference tracking errors

Figure D.16: Controller errors for the inner and outer loop in various metrics for leg 5

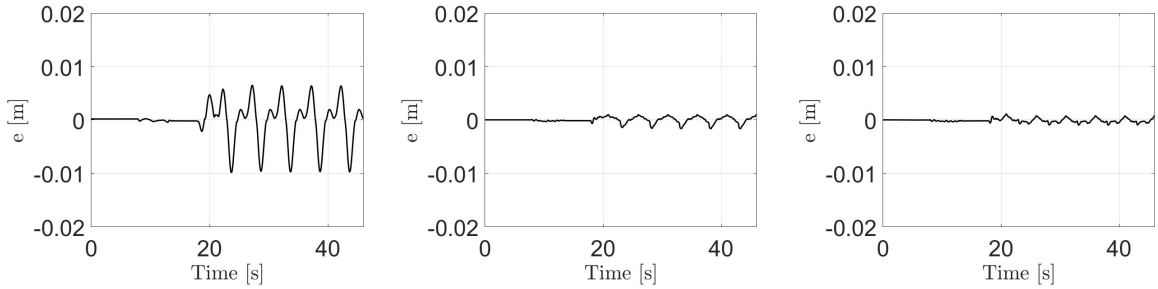

(a) CdP controller (b) Original INDI controller (c) New INDI controller

Figure D.17: Outer loop leg extension tracking errors for different controllers for leg 6

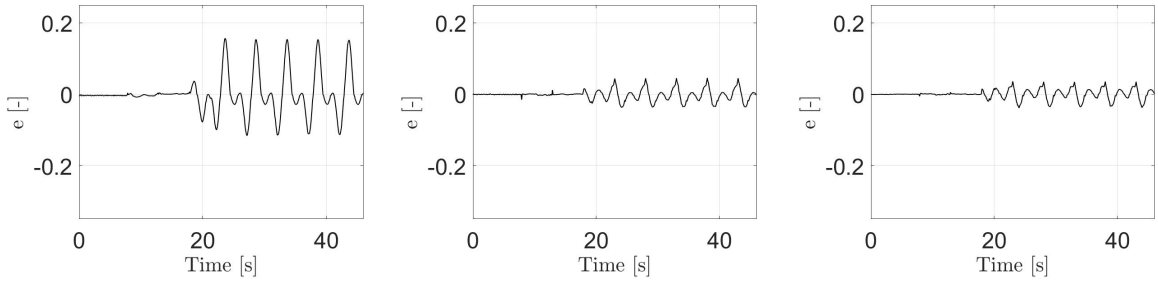

(a) CdP controller (b) Original INDI controller (c) New INDI controller

Figure D.18: Inner loop normalized pressure difference tracking errors for different controllers for leg 6

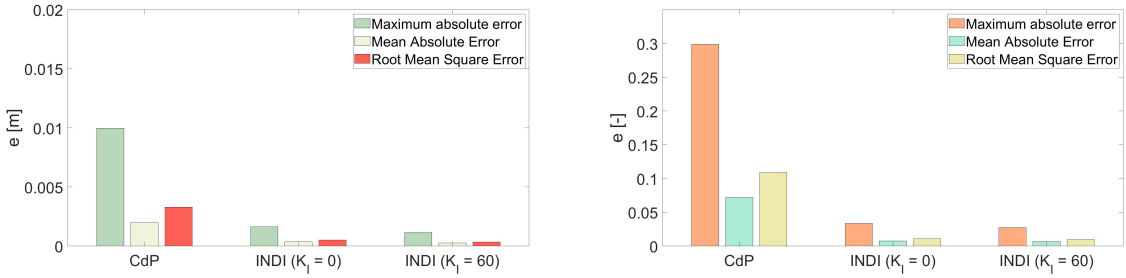

(a) Outer loop leg extension tracking errors (b) Inner loop normalized pressure difference tracking errors

Figure D.19: Controller errors for the inner and outer loop in various metrics for leg 6

E

Effect of integral gain

It is found in experiments on the SRS that the effect of an increased integral gain in the inner loop controller is different for the inner and outer loop control performance. Better inner loop performance does not necessarily lead to better outer loop performance. Increasing the K_I beyond 60 results in a smaller tracking error for the inner loop controller, but a larger tracking error for the outer loop controller. The maximum absolute error, the Mean Absolute Error (MAE) and the Root Mean Square Error (RMSE) for all of the six legs for the adapted INDI controller and varying K_I are shown in figure E.1.

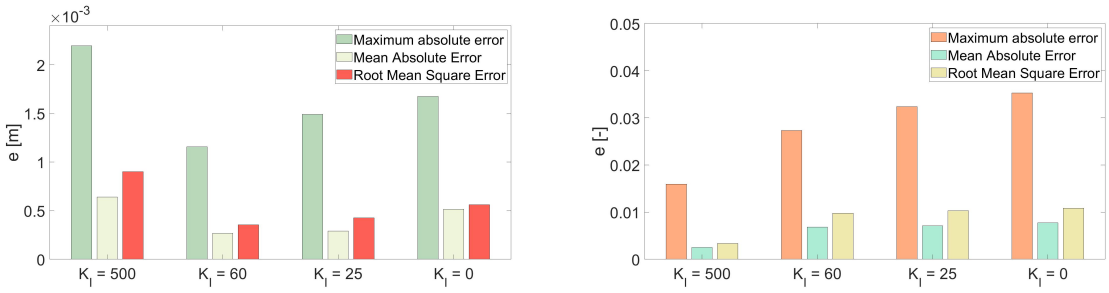

(a) Outer loop leg extension tracking errors

(b) Inner loop normalized pressure difference tracking errors

Figure E.1: Controller errors for the inner and outer loop for varying K_I and in various metrics for all legs

The inner loop tracking error is significantly reduced by changing the K_I from 60 to 500, but the outer loop tracking error becomes larger. In order to tune the controller properly it is therefore needed to simultaneously optimize the gains of the two loops in the cascaded controller using a strategy like Multi-Objective-Parameter-Optimization. Tools exist for Multi-Objective Parameter Optimization like MOPS [1]. It might be beneficial to make the K_I larger than 60, when a different outer loop controller is used. The gains of the inner loop controller will therefore have to be re-evaluated when this controller is used together with another outer loop controller such as an outer loop INDI motion controller.

The effect of integral gain for each individual leg is shown in figures E.2 to E.19. In the figures it can be observed that there are significant differences between the legs, especially for leg 4 as compared to the others. At this moment it is unknown why these differences occur and therefore further investigation is required into this phenomena. It might be beneficial to optimize the gains individually for the legs to further optimize the whole system.

[1] H.-D. Joos, "A multiobjective optimisation-based software environment for control systems design," in Proceedings. IEEE International Symposium on Computer Aided Control System Design. IEEE, 2002, pp. 7–14

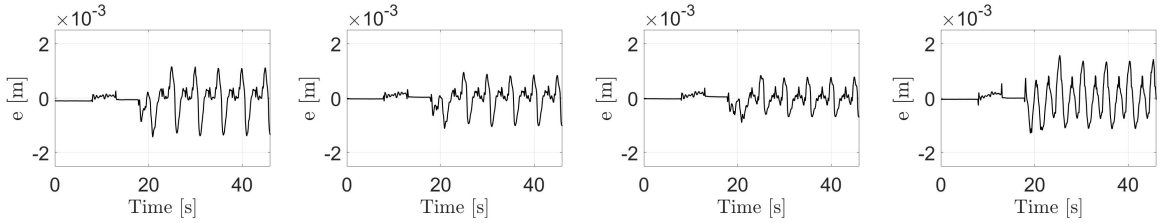

(a) $K_I = 0$ (b) $K_I = 25$ (c) $K_I = 60$ (d) $K_I = 500$

Figure E.2: Outer loop leg extension tracking errors for varying integral gain for leg 1

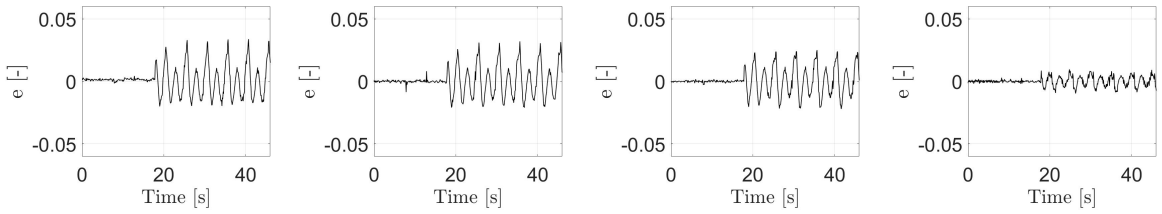

(a) $K_I = 0$ (b) $K_I = 25$ (c) $K_I = 60$ (d) $K_I = 500$

Figure E.3: Inner loop normalized pressure difference tracking errors for varying integral gain for leg 1

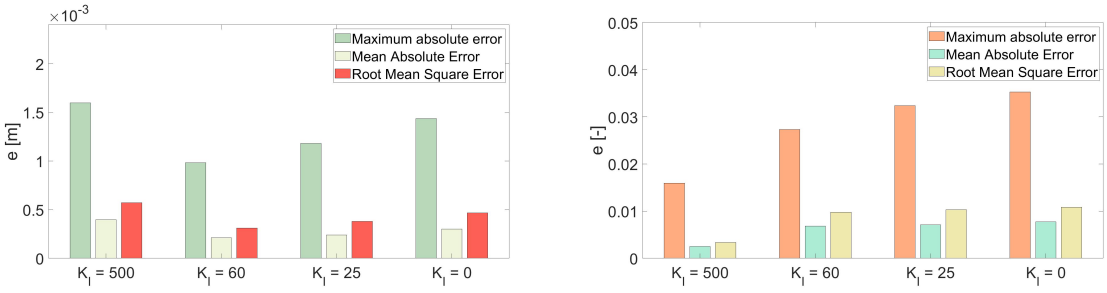

(a) Outer loop leg extension tracking errors (b) Inner loop normalized pressure difference tracking errors

Figure E.4: Controller errors for the inner and outer loop for varying K_I and in various metrics for leg 1

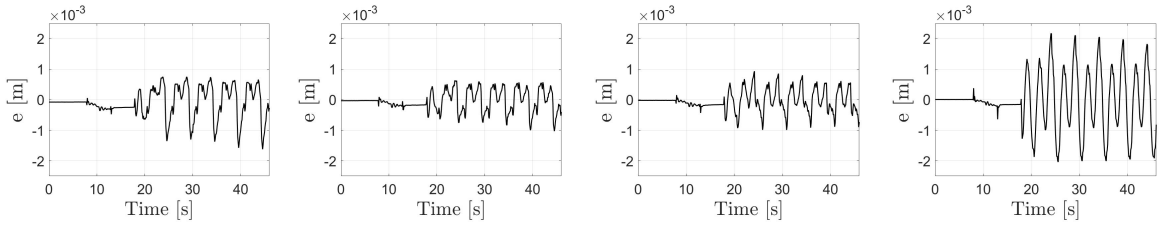

(a) $K_I = 0$ (b) $K_I = 25$ (c) $K_I = 60$ (d) $K_I = 500$

Figure E.5: Outer loop leg extension tracking errors for varying integral gain for leg 2

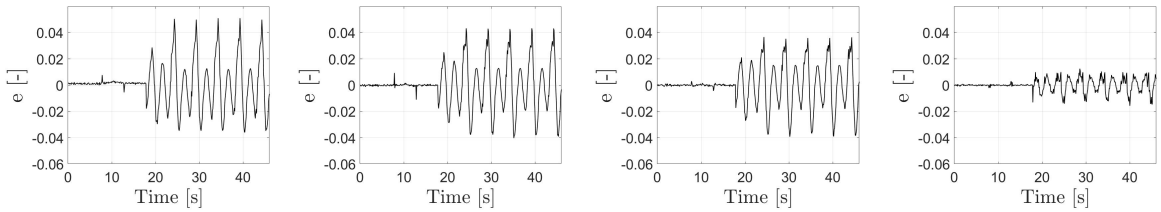

(a) $K_I = 0$ (b) $K_I = 25$ (c) $K_I = 60$ (d) $K_I = 500$

Figure E.6: Inner loop normalized pressure difference tracking errors for varying integral gain for leg 2

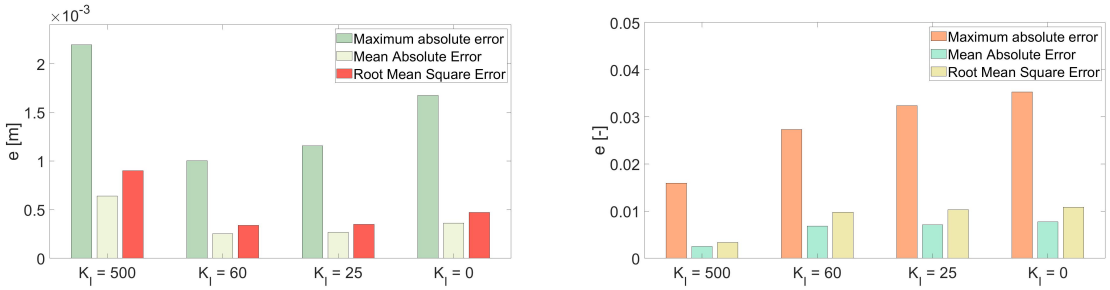

(a) Outer loop leg extension tracking errors (b) Inner loop normalized pressure difference tracking errors

Figure E.7: Controller errors for the inner and outer loop for varying K_I and in various metrics for leg 2

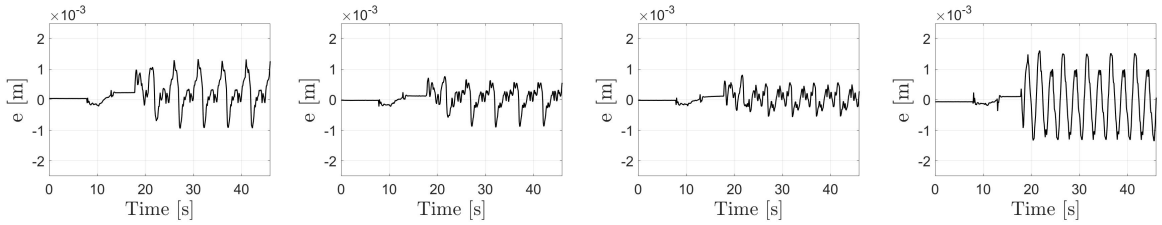

(a) $K_I = 0$ (b) $K_I = 25$ (c) $K_I = 60$ (d) $K_I = 500$

Figure E.8: Outer loop leg extension tracking errors for varying integral gain for leg 3

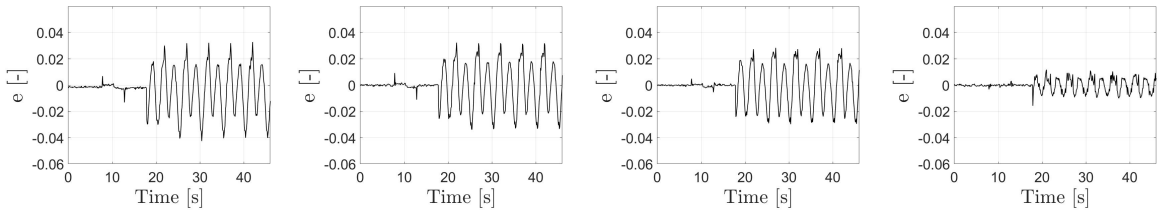

(a) $K_I = 0$ (b) $K_I = 25$ (c) $K_I = 60$ (d) $K_I = 500$

Figure E.9: Inner loop normalized pressure difference tracking errors for varying integral gain for leg 3

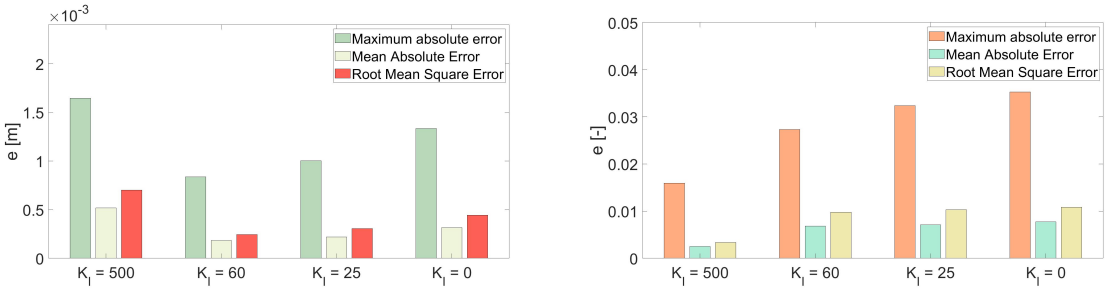

(a) Outer loop leg extension tracking errors (b) Inner loop normalized pressure difference tracking errors

Figure E.10: Controller errors for the inner and outer loop for varying K_I and in various metrics for leg 3

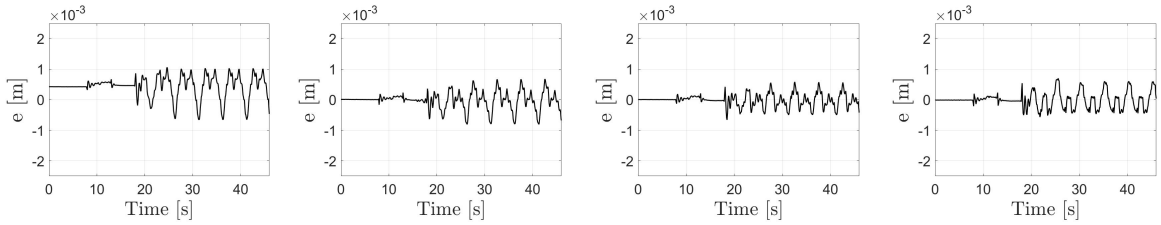

(a) $K_I = 0$ (b) $K_I = 25$ (c) $K_I = 60$ (d) $K_I = 500$

Figure E.11: Outer loop leg extension tracking errors for varying integral gain for leg 4

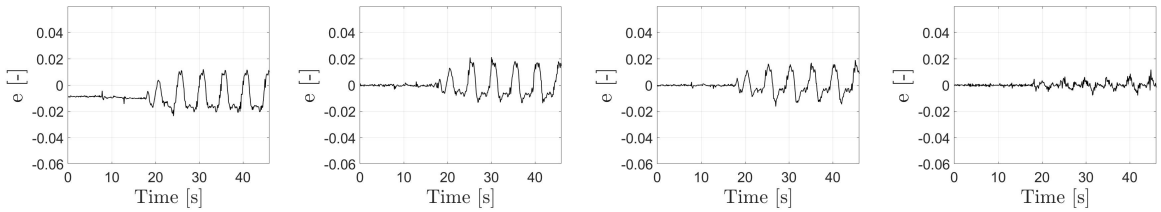

(a) $K_I = 0$ (b) $K_I = 25$ (c) $K_I = 60$ (d) $K_I = 500$

Figure E.12: Inner loop normalized pressure difference tracking errors for varying integral gain for leg 4

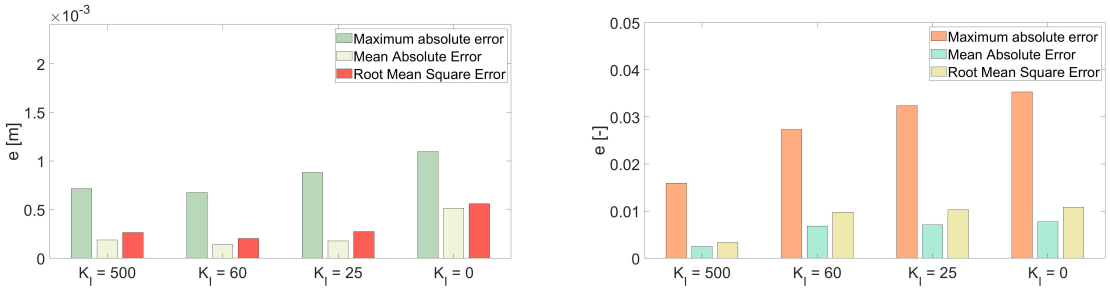

(a) Outer loop leg extension tracking errors (b) Inner loop normalized pressure difference tracking errors

Figure E.13: Controller errors for the inner and outer loop for varying K_I and in various metrics for leg 4

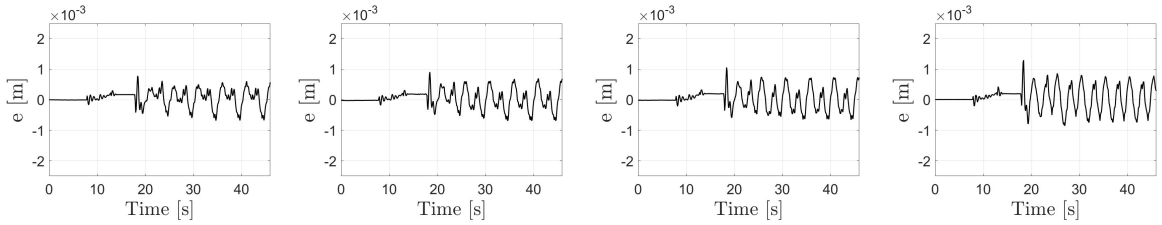

(a) $K_I = 0$ (b) $K_I = 25$ (c) $K_I = 60$ (d) $K_I = 500$

Figure E.14: Outer loop leg extension tracking errors for varying integral gain for leg 5

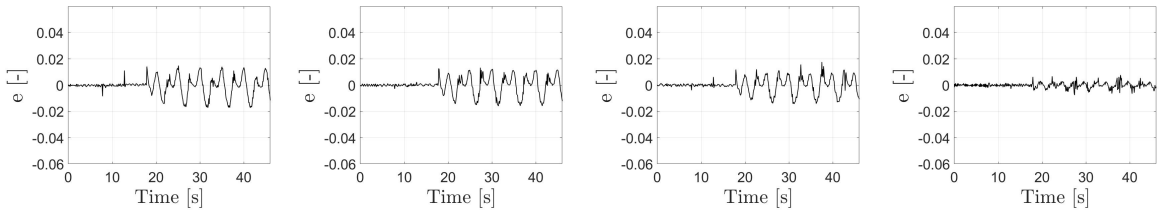

(a) $K_I = 0$ (b) $K_I = 25$ (c) $K_I = 60$ (d) $K_I = 500$

Figure E.15: Inner loop normalized pressure difference tracking errors for varying integral gain for leg 5

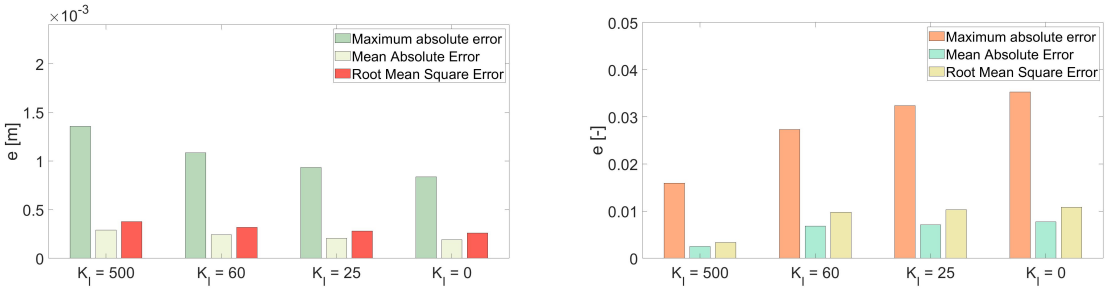

(a) Outer loop leg extension tracking errors (b) Inner loop normalized pressure difference tracking errors

Figure E.16: Controller errors for the inner and outer loop for varying K_I and in various metrics for leg 5

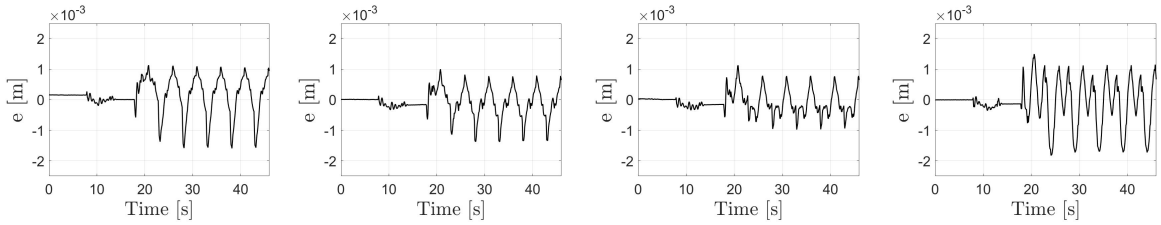

(a) $K_I = 0$ (b) $K_I = 25$ (c) $K_I = 60$ (d) $K_I = 500$

Figure E.17: Outer loop leg extension tracking errors for varying integral gain for leg 6

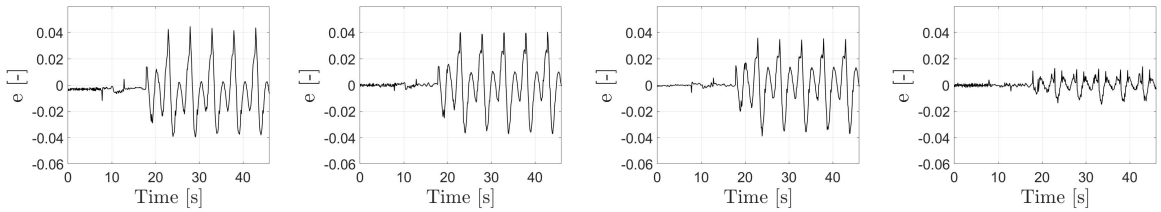

(a) $K_I = 0$ (b) $K_I = 25$ (c) $K_I = 60$ (d) $K_I = 500$

Figure E.18: Inner loop normalized pressure difference tracking errors for varying integral gain for leg 6

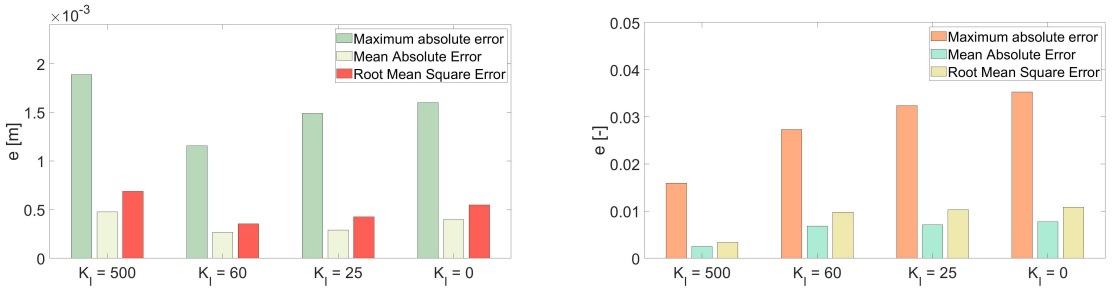

(a) Outer loop leg extension tracking errors (b) Inner loop normalized pressure difference tracking errors

Figure E.19: Controller errors for the inner and outer loop for varying K_I and in various metrics for leg 6

F

Saturation

The effects of saturation have been evaluated through experiments on the SRS for three different inner loop controllers. The original CdP, original INDI and adjusted INDI inner loop controllers have been evaluated using the sinusoidal references mentioned in appendix A. The adapted INDI controller contains the PCH adaptation as well as integral action ($K_I = 60$).

F.1. Inner loop CdP

The responses of the controller with an inner loop CdP controller during saturation can be observed in Figs. F.1 and F.2, which show the leg extensions tracking and normalized pressure difference tracking for each of the six legs.The figures shows that the controller remain stable during saturation. A pressure difference drop can be observed during saturation, which is to be expected. The hydraulic actuator is a velocity generator. During input saturation the velocity will therefore stagnate. The stagnation of the velocity causes the acceleration and pressure to drop. The inner loop CdP controller is behaving as expected and is able to handle the servo-valve saturation.

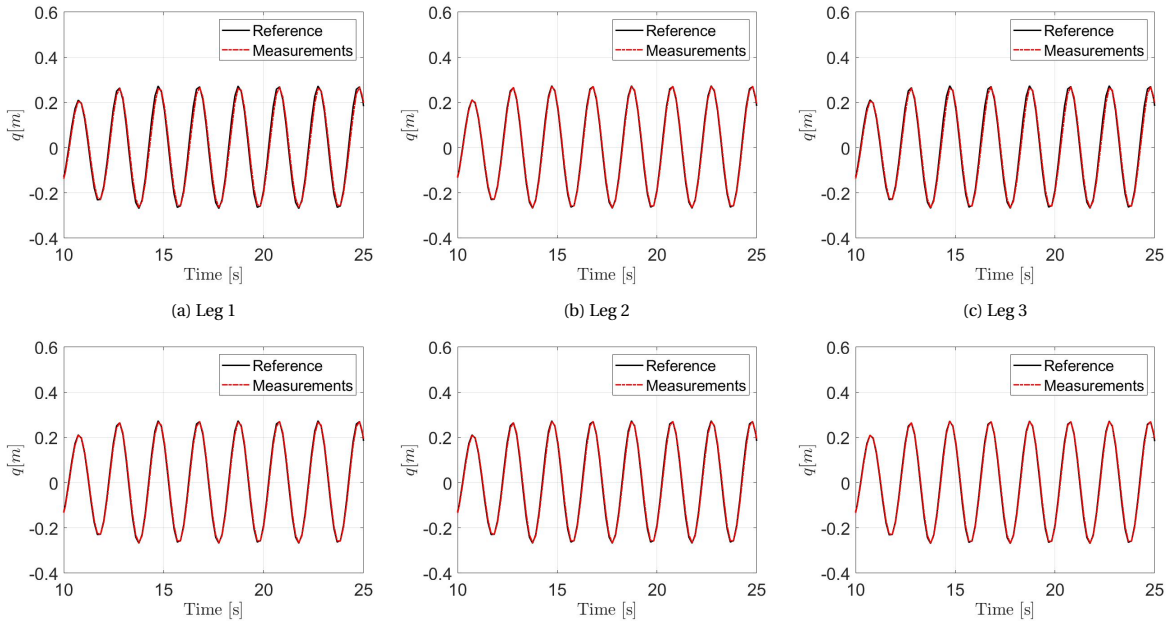

(a) Leg 1 (b) Leg 2 (c) Leg 3

(d) Leg 4 (e) Leg 5 (f) Leg 6

Figure F.1: Outer loop tracking of the leg extensions for each of the six legs for the controller with the original CdP controller without integral gain during saturation

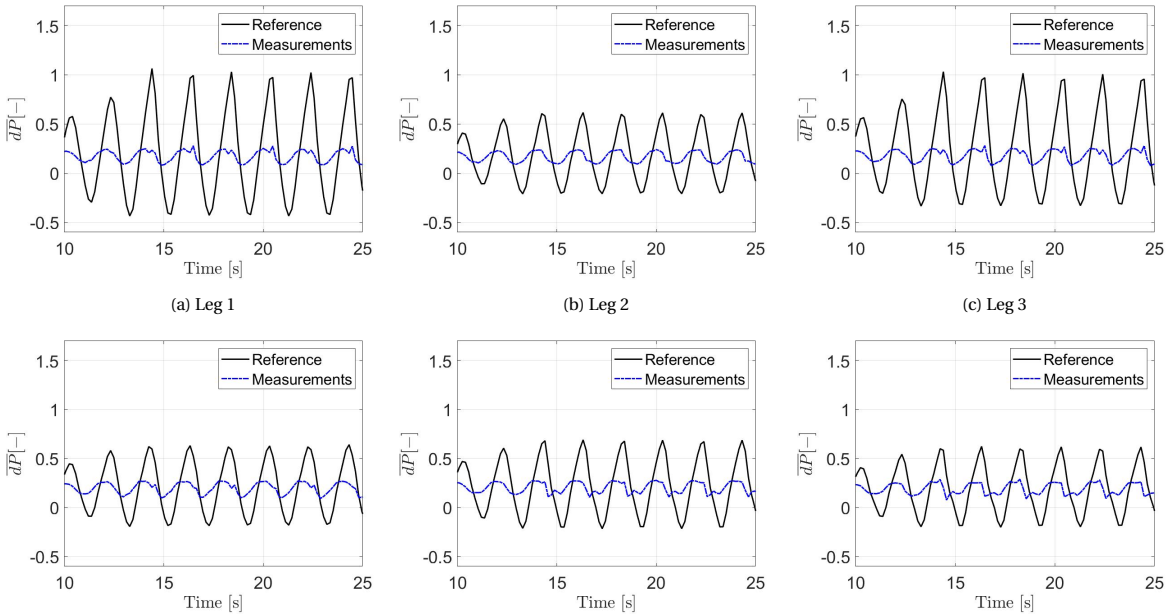

(a) Leg 1 (b) Leg 2 (c) Leg 3

(d) Leg 4 (e) Leg 5 (f) Leg 6

Figure F.2: Inner loop tracking of the normalized pressure for each of the six legs for the controller with the original CdP controller without integral gain during saturation

F.2. Inner loop INDI without integral action

From simulation it was found that the controller without integral action did not need any correction as it remained stable during saturation and showed no other undesirable effects. Therefore, the controller was evaluated during saturation on the SRS without any PCH correction. The results can be found in Figs. F.3 to F.5. Both the inner loop and outer loop tracking remain stable as shown by Figs. F.3 and F.4. During saturation the outer loop tracking performance will reduce, which leads to increased commands by the outer loop to the inner loop. This can also be observed in Fig. F.4. The increase in control action does however not build-up and after saturation the inner loop and outer loop follow the reference again without any delayed effects. Figure F.5 shows that the inner loop control to the servo-valve remains bounded as the only amount of input above the point of saturation ($\overline{x}_m = 1$) is due to the increment at that time step. The saturation is taken into account due to the fact that measurements of the main spool position are used in the incremental loop. The saturation is included in the measurements and therefore no wind-up will occur during saturation in the incremental loop.

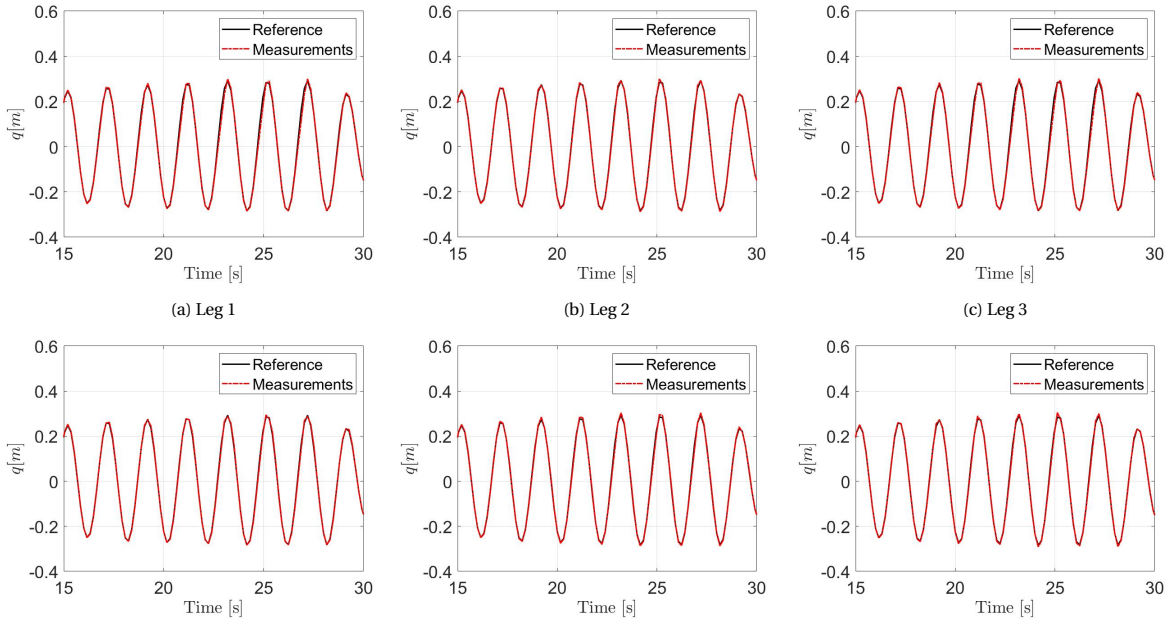

(a) Leg 1 (b) Leg 2 (c) Leg 3

(d) Leg 4 (e) Leg 5 (f) Leg 6

Figure F.3: Outer loop tracking of the leg extensions for each of the six legs for the controller with the original INDI controller without integral gain during saturation

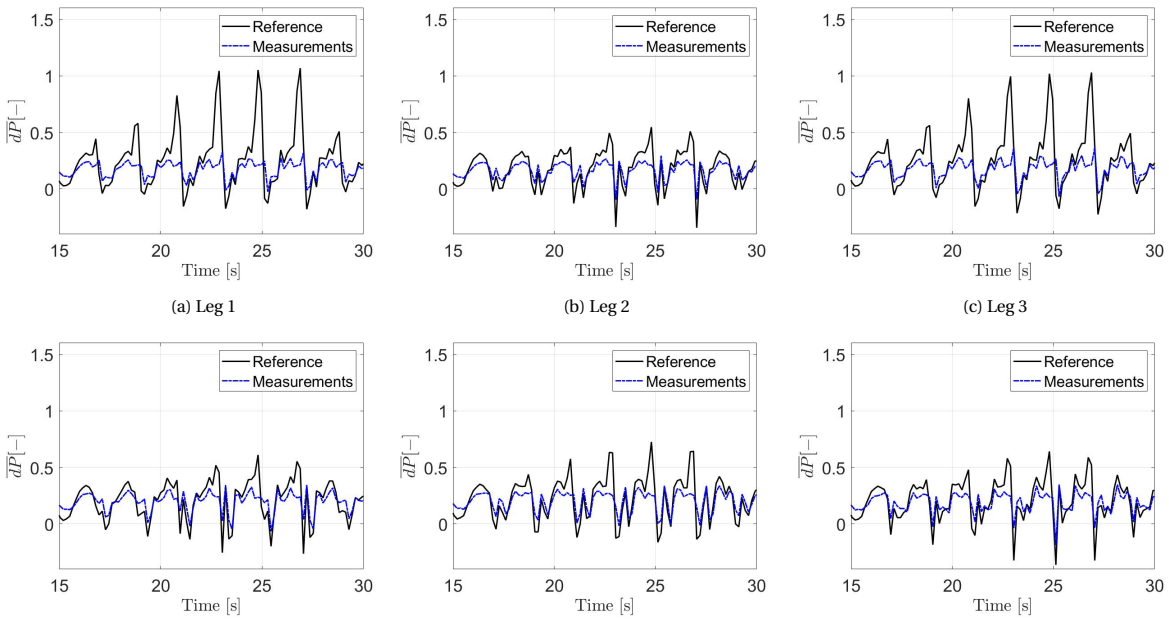

(a) Leg 1 (b) Leg 2 (c) Leg 3

(d) Leg 4 (e) Leg 5 (f) Leg 6

Figure F.4: Inner loop tracking of the normalized pressure for each of the six legs for the controller with the original INDI controller without integral gain during saturation

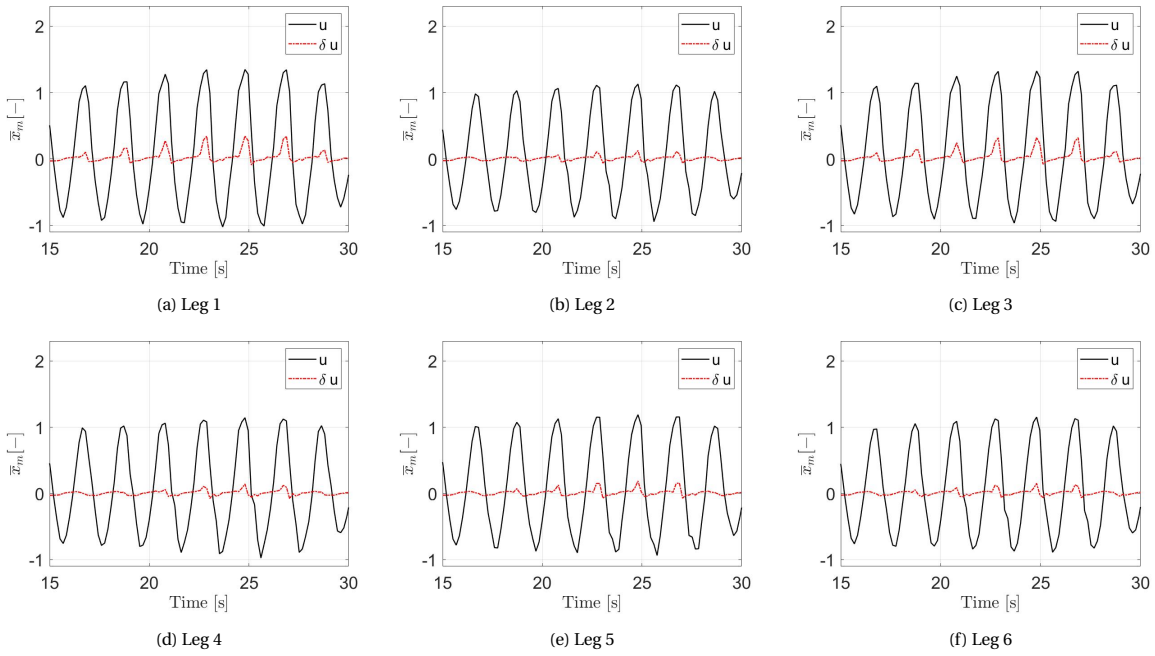

(a) Leg 1 (b) Leg 2 (c) Leg 3

(d) Leg 4 (e) Leg 5 (f) Leg 6

Figure F.5: Inner loop input command and increment for each of the six legs for the controller with the original inner loop INDI controller without integral gain during saturation

F.3. Inner loop INDI with integral action

Not all scenarios could be tested on the simulator, because the integral action will cause wind-up. An experiment without the corrective action by the PCH could damage the simulator when integral action is present in the inner loop INDI controller. Therefore some phenomena will be discussed through simulation results in the first section. The second section will show the results from experiments for the implementation with PCH. During the simulations a K_I of 175 is used.

F.3.1. Simulation

In order to demonstrate the effect of the wind-up on the system a heave reference is simulated with increasing amplitude over time. The outer loop tracking for this reference is shown in Fig. F.6.

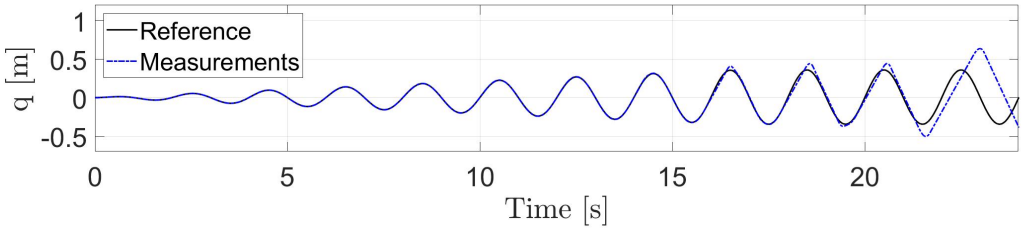

Figure F.6: Outer loop leg extension tracking for the sinusoidal reference that leads to saturation by the INDI controller with integral action, but without PCH for a single leg

The above figure shows that the measured extension in the simulation reaches above the reference, which illustrates that the integrator wind-up introduces undesirable effects. Next the inner loop tracking is considered, which is shown in Fig. F.7, to get a better understanding for the reason of this behavior.

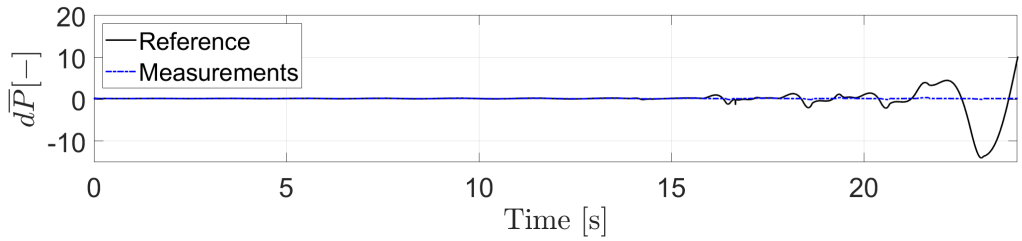

Figure F.7: Inner loop normalized pressure difference tracking for the sinusoidal reference that leads to saturation by the INDI controller with integral action, but without PCH for a single leg

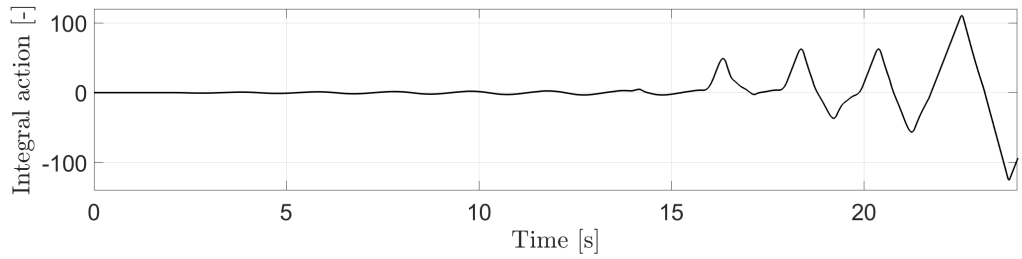

Figure F.8: Integral action in the inner loop controller for the sinusoidal reference that leads to saturation by the INDI controller with integral action, but without PCH for a single leg

Figure F.8 shows that the integral action is indeed winding-up during saturation. The integral action grows too large. The controller will therefore have to counter the wind-up, which explains that the pressure reaches above the reference in Fig. F.6. The PCH implementation should be able to prevent the integral action from growing too large. The simulation results of the PCH implementation with $K_{PCH} = 20$ are shown in Figs. F.9 to F.12.

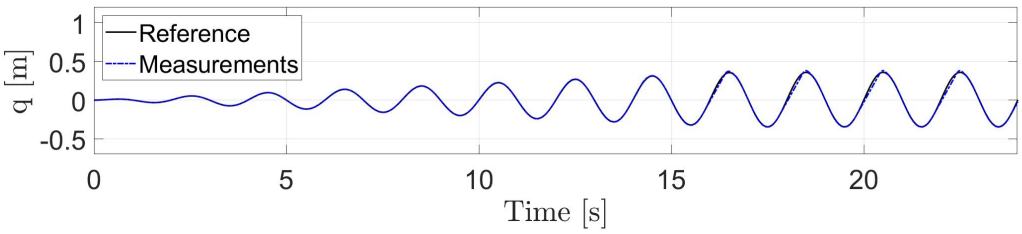

Figure F.9: Outer loop leg extension tracking for the sinusoidal reference that leads to saturation by the INDI controller with integral action and PCH ($K_{PCH} = 20$) for a single leg

The PCH prevents the leg extension from reaching far above the reference and greatly reduces the effects due to integrator wind-up. The extension does however reach slightly above the reference and therefore the inner loop tracking is considered, which is shown in Fig. F.10.

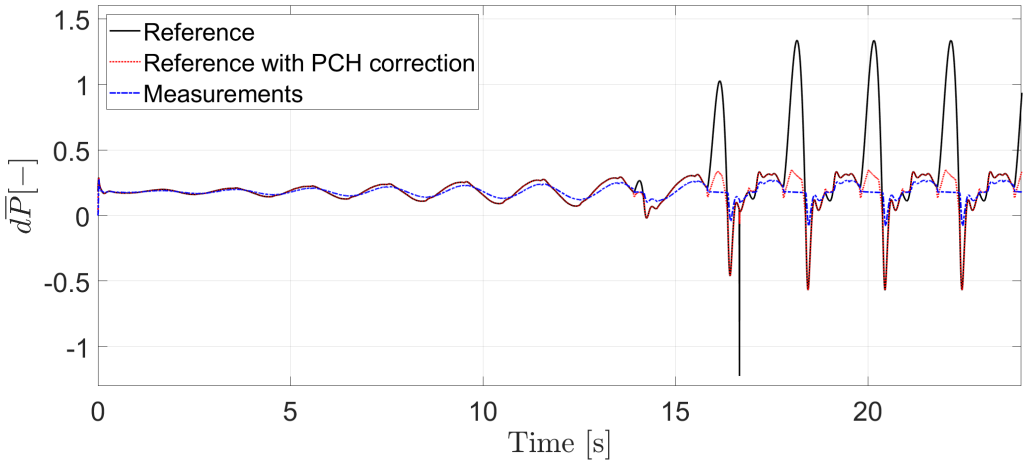

Figure F.10: Inner loop normalized pressure difference tracking for the sinusoidal reference that leads to saturation by the INDI controller with integral action and PCH ($K_{PCH} = 20$) for a single leg

Figure F.10 shows both the original reference and the reference adjusted by the PCH. During saturation the original reference and the adjusted reference differ. There is still a slight error between the adjusted reference and the pressure during saturation as well, which causes the integral action to grow slightly. This in turn causes the small amount of additional extension above the reference in Fig F.9. The effects are however so small that they can be neglected for this use case. Figure F.11 shows the integrator action for the implementation with PCH, so that it can be compared to the integrator action in Fig. F.8.

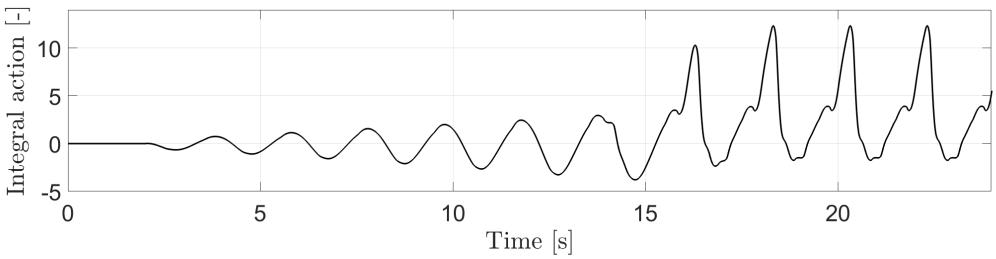

Figure F.11: Integral action in the inner loop controller for the sinusoidal reference that leads to saturation by the INDI controller with integral action and PCH ($K_{PCH} = 20$) for a single leg

As mentioned earlier there is still a small amount of integrator wind-up, which has a minor effect on the outer loop controller. During the experiments on the SRS a K_{PCH} of 20 was used as well. In order to reduce the integrator wind-up even further it is advised to change the value from 20 to 40 for the final implementation of the controller, which reduces the integrator wind-up even further in simulation as shown in Fig. F.12.

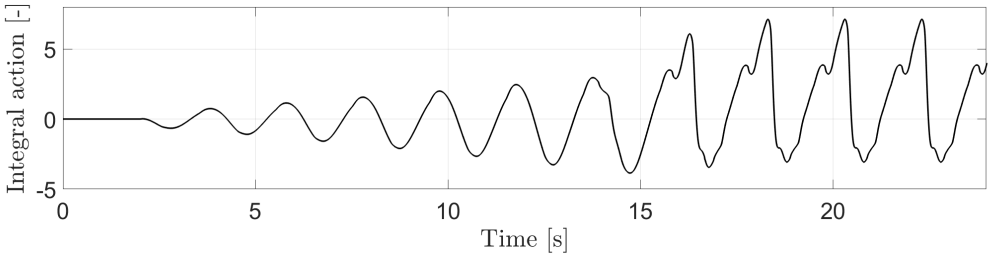

Figure F.12: Integral action in the inner loop controller for the sinusoidal reference that leads to saturation by the INDI controller with integral action and PCH ($K_{PCH} = 40$) for a single leg

F.3.2. Experiments

The PCH implementation is evaluated through experiments on the SRS and the results are shown in Figs. F.13 to F.17. The outer loop tracking shown in Fig. F.13 is behaving as expected and only shows some decreased tracking performance during saturation. Figure F.17 shows that the reference is adjusted by the PCH and Fig. F.14 shows that the commanded control input to the servo-valve remains bounded and does not keep growing due to wind-up effects. The hedging action can be found in Fig. F.15. The integrator actions are shown in Fig. F.16, where it can be observed that still a slight integrator wind-up occurs, which was also shown in simulation. This wind-up does not lead to instability or other undesirable effects in the outer loop due to its small magnitude. The effects would only be noticeable after an unrealistically long saturation, but it is still recommended to change the K_{PCH} from 20 to 40 for the final implementation of the controller for the SRS to further reduce this effect.

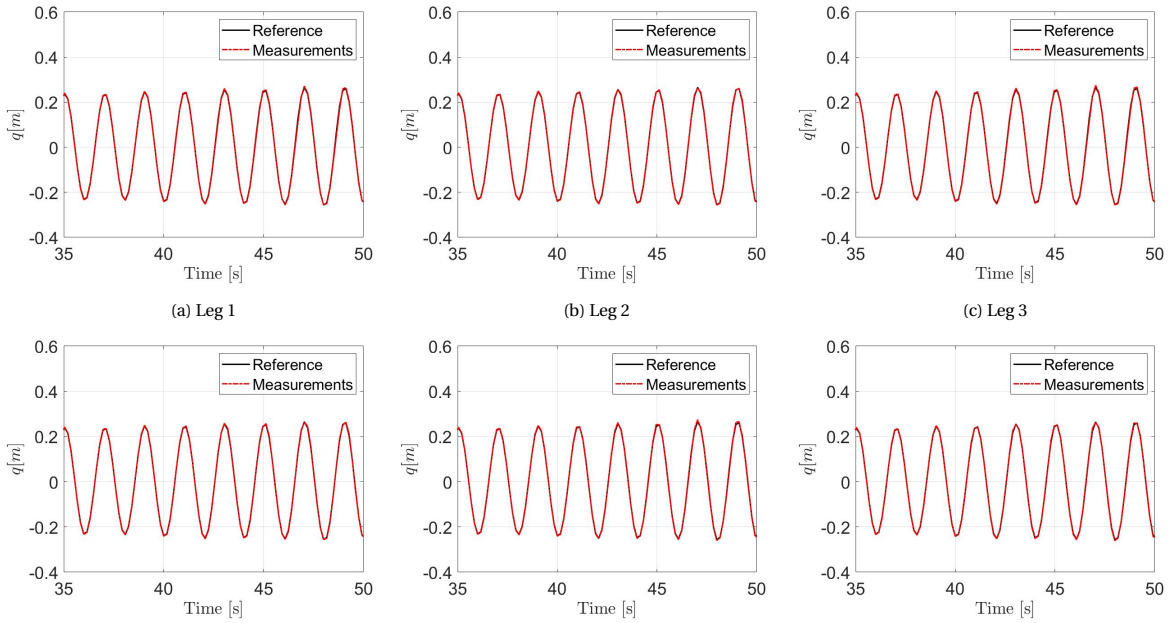

(a) Leg 1 (b) Leg 2 (c) Leg 3

(d) Leg 4 (e) Leg 5 (f) Leg 6

Figure F.13: Outer loop tracking of the leg extensions for each of the six legs for the controller with the new INDI controller during saturation

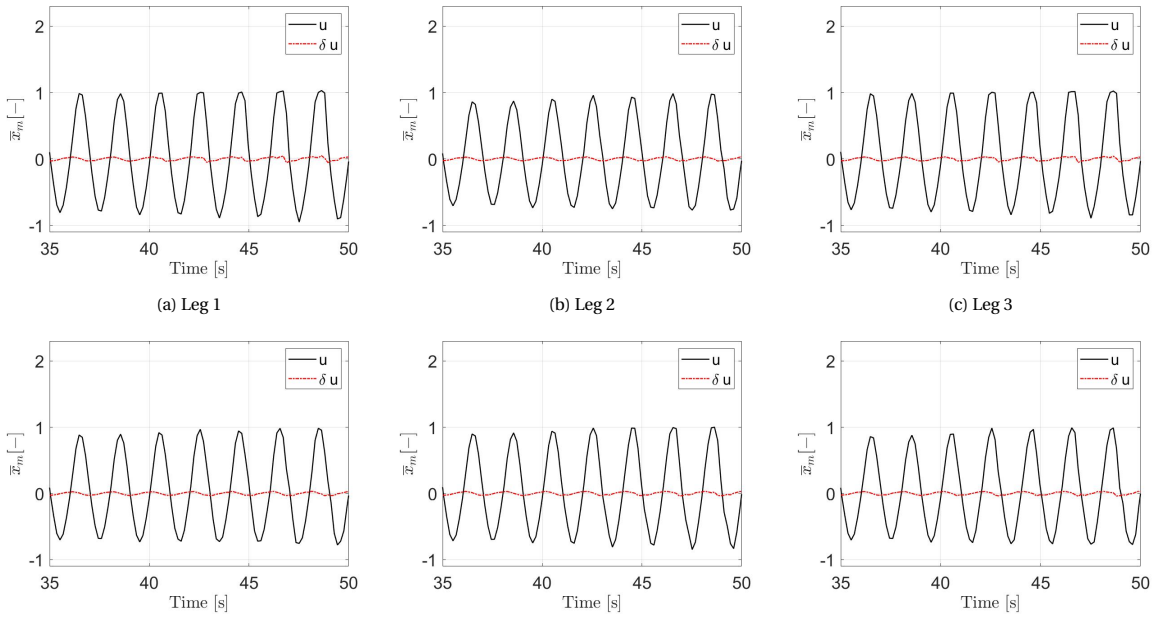

(a) Leg 1 (b) Leg 2 (c) Leg 3

(d) Leg 4 (e) Leg 5 (f) Leg 6

Figure F.14: Inner loop input command and increment for each of the six legs for the controller with the adjusted inner loop INDI controller with integral gain during saturation

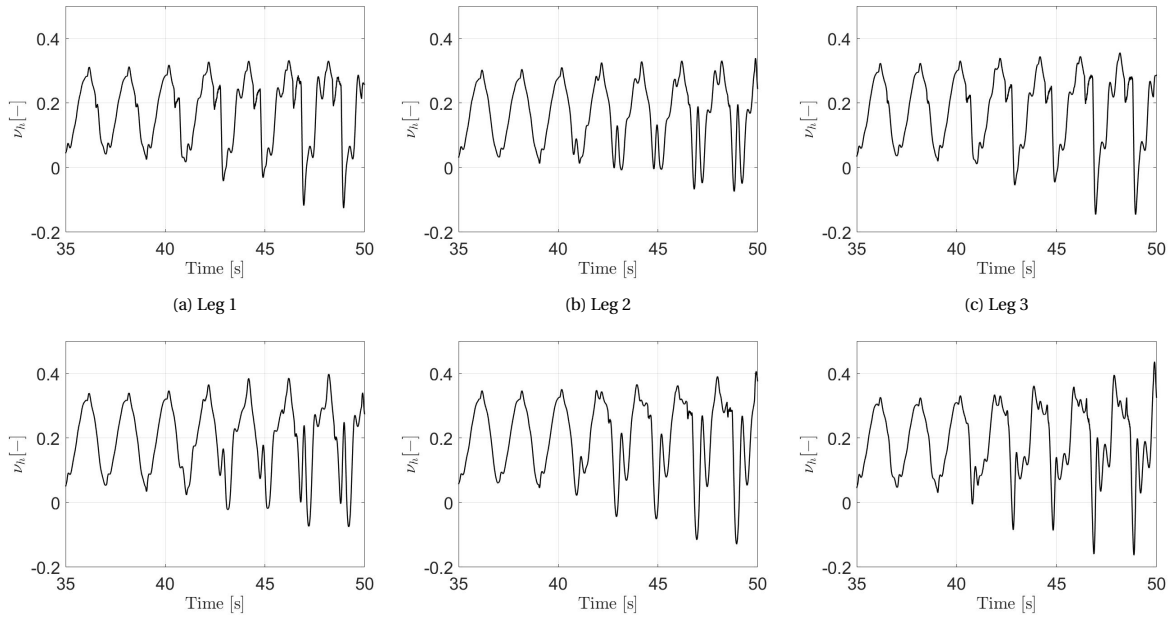

(a) Leg 1 (b) Leg 2 (c) Leg 3

(d) Leg 4 (e) Leg 5 (f) Leg 6

Figure F.15: Virtual control hedge for each of the six legs for the controller with the adjusted inner loop INDI controller with integral gain during saturation

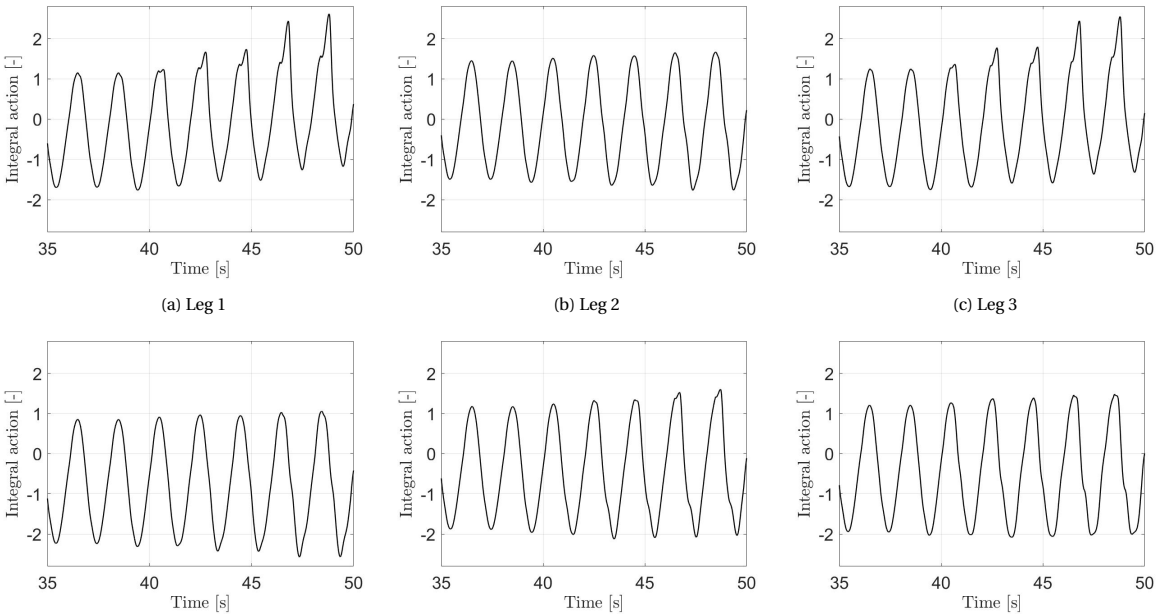

(a) Leg 1 (b) Leg 2 (c) Leg 3

(d) Leg 4 (e) Leg 5 (f) Leg 6

Figure F.16: Inner loop tracking of the normalized pressure for each of the six legs for the controller with the new INDI controller during saturation

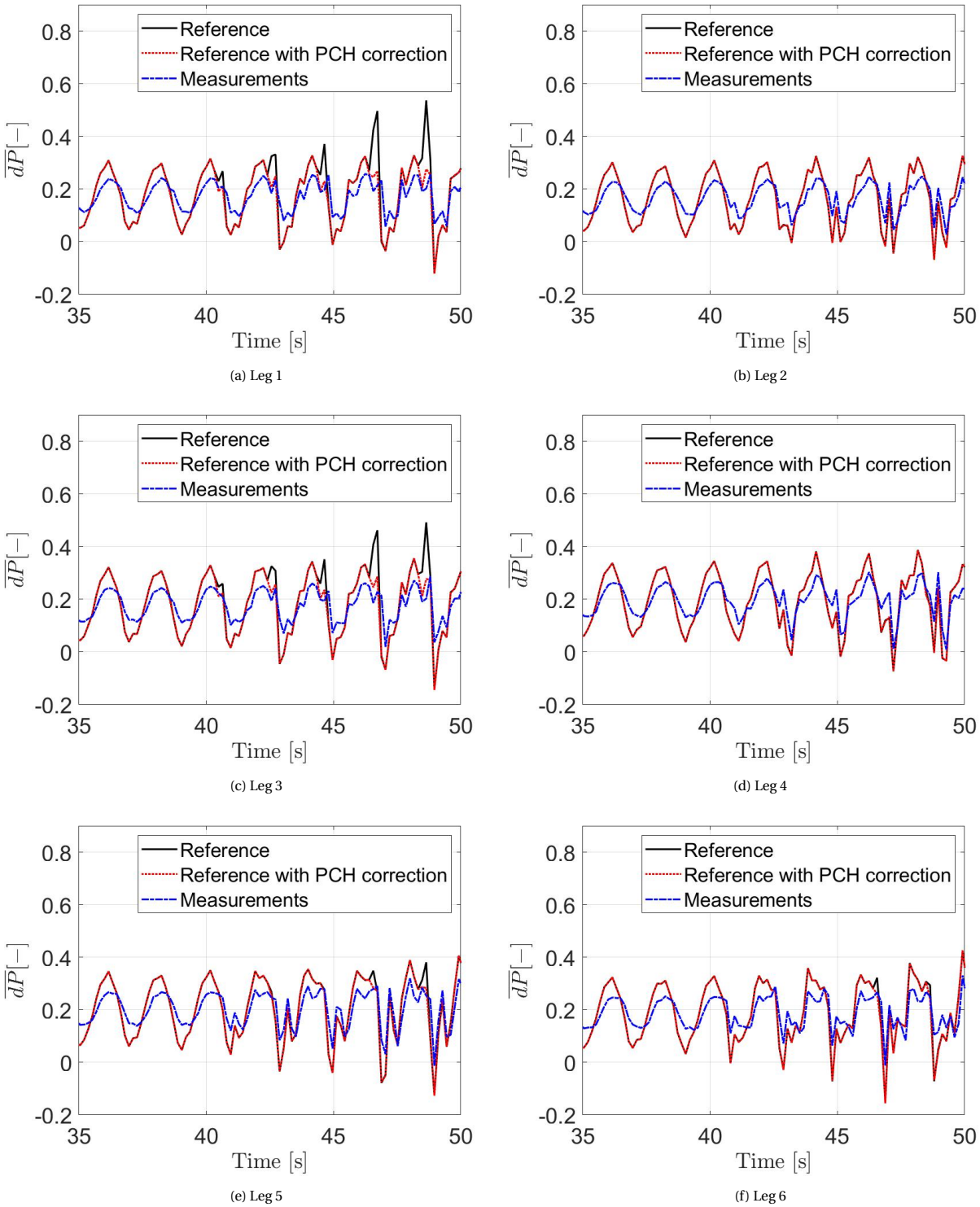

(a) Leg 1

(b) Leg 2

(c) Leg 3

(d) Leg 4

(e) Leg 5

(f) Leg 6

Figure F.17: Inner loop tracking of the normalized pressure for each of the six legs for the controller with the new INDI controller during saturation

G

Instability

The data acquisition of the SRS has been changed. After the changes the INDI controller was not stable anymore. The reason for the instability was unknown. The inner loop tracking during instability with an accompanying spectral analysis of the normalized pressure difference measurement signal is shown in Fig. G.1. This data is obtained through experiments on the SRS.

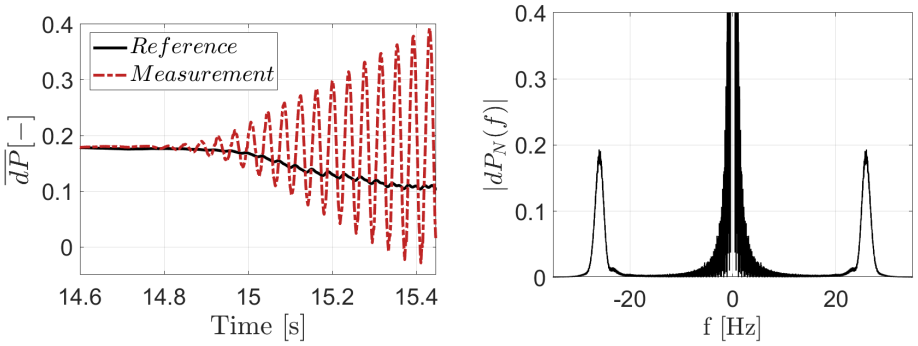

(a) Time domain

(b) Frequency domain

Figure G.1: Inner loop pressure tracking and spectral analysis of the pressure measurement during an experiment where the SRS controller with inner loop INDI became unstable

The unstable oscillation has a frequency of 26 Hz. Through simulation it was found that a delay of 6 ms in the outer linearization loop of the inner loop INDI controller led to a similar instability with a frequency close to 26 Hz. The simulation results are shown in Fig. G.2.

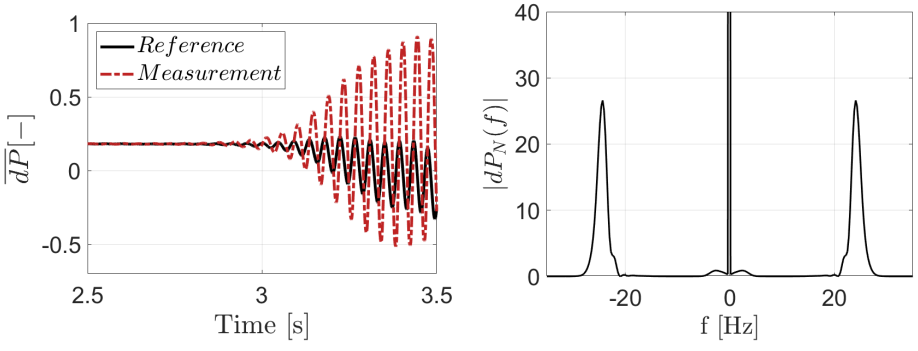

(a) Time domain

(b) Frequency domain

Figure G.2: Simulation of the inner loop pressure tracking with a 6 ms delay in the pressure derivative feedback and spectral analysis of the pressure difference derivative signal

This finding led to the hypothesis that the instability was caused by a delay in the measurements of the pressure difference. Through a analysis of the system it was found that an high accuracy option was enabled in the data acquisition of the pressure signal. Because of this option the signals was averaged over multiple consecutive samples leading to an equivalent delay of 7.2 ms. The option was switched from the high accuracy to the high speed mode so that the delay was lowered to about 1 ms. This change in data acquisition mode solved the problem and allowed for a stable inner loop INDI controller again for the SRS.

H

Modeling of the SRS

In the preliminary report it has been discussed in detail how the servo-system is modeled and simulated. Y. Huang has modeled the Stewart platform, which is treated in his work [1]. The user is therefore referred to these works for a detailed explanation on the topic of simulation of the SRS.

[1] Y. Huang, D. M. Pool, O. Stroosma, Q. P. Chu, and M. Mulder, "Modeling and Simulation of Hydraulic Hexapod Flight Simulator Motion Systems," in AIAA Modeling and Simulation Technologies Conference, January 2016.

Potential of outer loop INDI

In this work a model-based outer loop controller is used as motion controller. Huang has designed and tested an outer loop INDI controller for the SRS [1]. For future work it would therefore be interesting to combine the adapted inner loop INDI controller with this outer loop INDI controller. The outer loop INDI controller is shown in Fig. I.1.

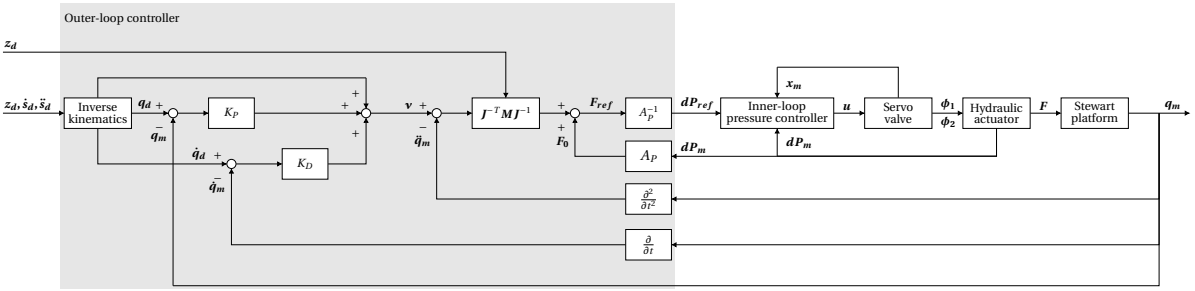

Figure I.1: Cascaded hydraulic control structure with the outer loop INDI controller

Through simulation a preliminary evaluation is performed to get an understanding of the potential of such a controller. The circular motion reference is used for the evaluation. The adapted inner loop controller is used together with the outer loop INDI controller. For the outer loop controller $K_P = 3000$, $K_I = 110$ and $K_D = 160$. The outer loop tracking errors for each leg are shown in Fig I.2 and the resulting total error metrics in Tab. I.1. The simulation indicates that the maximum tracking error can reduced by a factor 2 from around 1.1 mm to 0.55 mm. It should be mentioned that the gains used for this simulation are not optimized at all and therefore it is likely that better performance can be achieved by applying strategies like Multi-Objective Parameter Optimization using tools like MOPS [2]. The results do however shows that the performance can be increased by applying outer loop INDI, which is also found by Huang[1]. In his work he also found the outer loop controller to be more robust to model mismatches and uncertainties.

Table I.1: Error metrics for the cascaded controller with an inner and an outer INDI controller

Maximum Absolute Error	**RMSE**	**MAE**
$5.5E^{-4}\,[m]$	$2.1E^{-4}\,[m]$	$1.8E^{-4}\,[m]$

[1] Y. Huang, D. M. Pool, O. Stroosma, Q. P. Chu, and M. Mulder, "Modeling and Simulation of Hydraulic Hexapod Flight Simulator Motion Systems," in AIAA Modeling and Simulation Technologies Conference, January 2016.

[2] H.-D. Joos, "A multiobjective optimisation-based software environment for control systems design," in Proceedings. IEEE International Symposium on Computer Aided Control System Design. IEEE, 2002, pp. 7–14

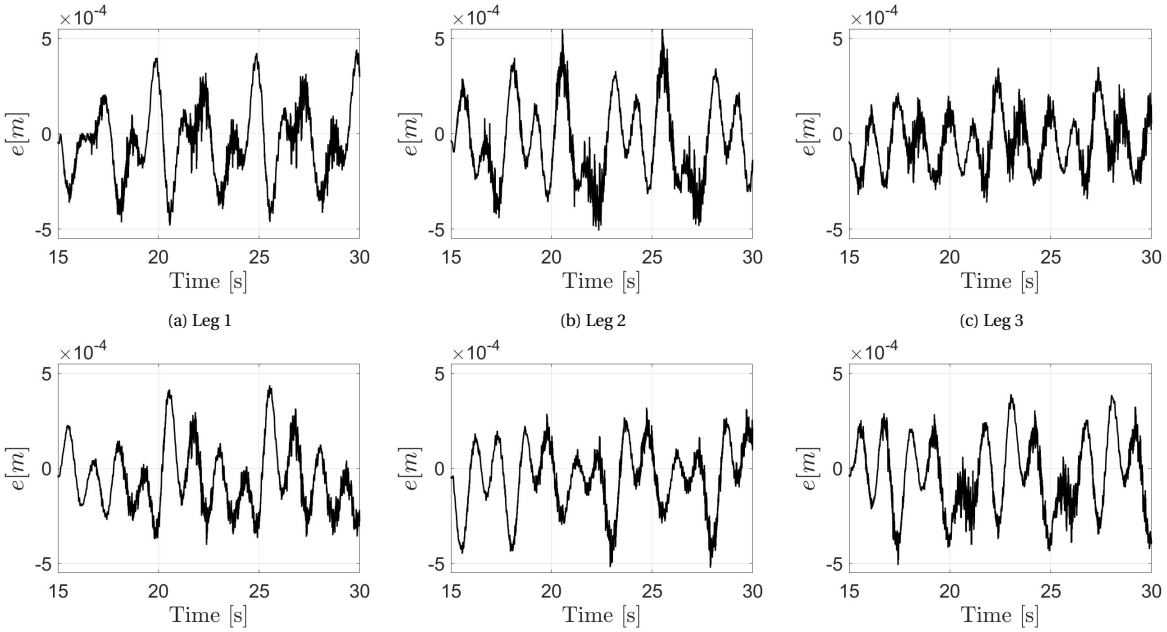

(a) Leg 1 (b) Leg 2 (c) Leg 3

(d) Leg 4 (e) Leg 5 (f) Leg 6

Figure I.2: Outer loop tracking of the leg extensions for each of the six legs for the controller with the new INDI controller during saturation